ADVANCED TECHNIQUES FOR ENHANCING PERFORMANCE IN VISIBLE LIGHT COMMUNICATION SYSTEMS

Ph.D. Thesis

by

ANUPMA SHARMA

DEPARTMENT OF ELECTRICAL ENGINEERING
INDIAN INSTITUTE OF TECHNOLOGY
INDORE

OCTOBER, 2024

ADVANCED TECHNIQUES FOR ENHANCING PERFORMANCE IN VISIBLE LIGHT COMMUNICATION SYSTEMS

A THESIS

Submitted in partial fulfillment of the

requirements for the award of the degree

of

DOCTOR OF PHILOSOPHY

by

ANUPMA SHARMA

DEPARTMENT OF ELECTRICAL ENGINEERING

INDIAN INSTITUTE OF TECHNOLOGY INDORE

OCTOBER, 2024

INDIAN INSTITUTE OF TECHNOLOGY INDORE

CANDIDATE'S DECLARATION

I hereby certify that the work which is being presented in the thesis entitled "**ADVANCED TECHNIQUES FOR ENHANCING PERFORMANCE IN VISIBLE LIGHT COMMUNICATION SYSTEMS**" in the partial fulfillment of the requirements for the award of the degree of DOCTOR OF PHILOSOPHY and submitted in the DEPARTMENT OF ELECTRICAL ENGINEERING, Indian Institute of Technology Indore, is an authentic record of my own work carried out during the time period from November 2019 to October 2024 under the supervision of Prof. Vimal Bhatia, Professor, Indian Institute of Technology Indore, India.

The matter presented in this thesis has not been submitted for the award of any other degree of this or any other institute.

25-10-2024

Signature of the student with date

(ANUPMA SHARMA)

This is to certify that the above statement made by the candidate is correct to the best of my knowledge.

25.10.2024

Signature of Thesis Supervisor with date

(Prof. VIMAL BHATIA)

Anupma Sharma has successfully given her Ph.D. Oral Examination held on April 30, 2025.

30.04.2025

Signature of Thesis Supervisor with date

(Prof. VIMAL BHATIA)

ACKNOWLEDGEMENTS

With profound reverence and heartfelt gratitude, I begin this acknowledgment by thanking the Almighty for bestowing upon me the strength, wisdom, and perseverance throughout this extraordinary academic journey.

I extend my sincere gratitude to my Ph.D. supervisor, Prof. Vimal Bhatia, for his continuous guidance and support throughout my thesis work. I extend my sincere appreciation to my PSPC committee members, Prof. Anand Parey and Prof. Shanmugam Dhinakaran, whose insights, constructive criticism, and enlightening discussions have immensely enriched my research perspective.

I am particularly grateful to Prof. C.P. Li and Dr. Keshav Singh, for inviting me as an intern at NSYSU, Kaohsiung Taiwan. This international exposure has been instrumental in expanding my research network and bringing fresh perspectives to my work. Their expertise and innovative insights have significantly elevated the quality of my research work and broadened my academic horizons. This academic pursuit would not have been possible without the generous financial support by the Ministry of Electronics & Information Technology, Government of India.

The conducive academic environment at IIT Indore has been crucial to my research journey, and I am grateful to all faculty members and staff for their consistent support. The Signal and Software group (SaSg) has been more than just a research group – it has been a sanctuary of intellectual growth and camaraderie. I am particularly indebted to my seniors and labmates: Dr. Rangeet Mitra, Dr. Sandesh Jain, Dr. Justin Jose, Dr. Deepak Kumar, Dr. Abhinav Singh Parihar, Dr. Vidya Bhaskar Shukla, Dr. Vaishali Sharma, Dr. Purva Sharma, Amit Baghel, Prakhar Keshari and last but not the least Dr. Shubham Bisen who have been steadfast companions and beacons of guidance throughout this journey.

Finally, and most profoundly, I dedicate this thesis to my pillars of strength – my parents and my brother. Whatever modest achievements I have garnered in life are the fruits of their sacrifices, unconditional love, and steadfast belief in my abilities. Their unwavering support and endless encouragement have been the driving force behind every step of my academic journey. To them, I owe not just this thesis, but the very essence of my academic aspirations. In the tapestry of academic life, friends play an invaluable role in maintaining balance and perspective. I owe special gratitude to Ritu Daryani and Aayush Singh, whose extraordinary support, endless encouragement, and unwavering friendship have been instrumental in helping me navigate the complexities of this academic pursuit. Their presence has made this journey not just bearable, but truly memorable.

This acknowledgment, though extensive, barely scratches the surface of the gratitude I feel towards everyone who has contributed to this significant chapter of my life. The completion of this thesis stands as a testament to the collective support, guidance, and encouragement of all these remarkable individuals.

ANUPMA SHARMA

Dedicated to my family

ABSTRACT

With the increase in high-speed-data demand for the upcoming fifth generation (5G) and beyond communication systems visible light communications (VLC) has emerged as a low-cost, green, and secure technology complementary to the currently congested traditional radio frequency (RF) communications owing to its wide license-free spectrum. In VLC, data transmission is achieved by modulating the intensity of light emitted from light-emitting diodes (LEDs). Using LEDs as transmitters, VLC enables simultaneous data communication and illumination.

Despite VLC's promise as a viable supplement to RF-based communication systems, the performance of a VLC system is significantly limited by several factors, such as: (a) multiplicative fading distortion due to user mobility and multipath between receiver and transmitter, (b) nonlinear characteristics of an LED, (c) presence of thermal and ambient noise, (d) absence of a direct link, and (e) limited coverage as visible light can not penetrate obstacles and is reflected back due to the high penetration loss. Moreover, the illumination requirements of LEDs pose a challenge to the practical deployment of VLC. The aforementioned VLC channel impairments significantly degrade the achievable bit error rate (BER) performance, and cause a significant performance-gap between the promised and the achieved sum rate of VLC based systems.

In this context, conventional modulation schemes for VLC such as, optical orthogonal frequency division multiplexing (OOFDM) are capable of mitigating inter-symbol-interference (ISI) due to time-domain dispersion caused by multipath reflections. Further, user mobility leads to variations in VLC channel-gains, that in-turn, leads to lowering of instantaneous signal-to-noise ratio (SNR). To jointly mitigate impairments due to user mobility and multipath dispersion, recently, orthogonal time frequency space (OTFS) modulation technique has been proposed. There are primarily two ways to mitigate the effect of LED nonlinearity i.e. by using pre-distorters and post-distorters. Pre-distortion techniques are known to outperform static inversion, however, it requires perfect feedback of the channel state information (CSI) from the receiver to the transmitter in a closed loop. Further, the performance of a VLC system is significantly limited by the absence of direct links or blockage of the line-of-sight (LoS) channel, which creates blind spots. Optical reflecting intelligent surface (ORIS) is a recently developed promising technology that uses reflecting surfaces to facilitate the non-line-of-sight (NLoS) paths and improve the performance of wireless communication systems. The mirror array (MA)-based RIS and the metasurface array (MSA)-based RIS are the two most popular reflecting surface designs employed for ORIS in VLC systems, where MA-based RIS performs better. Additionally, poor channel estimation can be caused by nonlinear distortions, which can seriously impair signal reception and add an equivalent additive distortion at the receiver. Similarly, practical VLC systems also suffer from ambient and thermal noise. Ambient light noises may arise from sunlight, skylights, incandescent and fluorescent lamps, and other light sources present in the indoor environment. Furthermore, the trans-impedence receiver circuitry produces the thermal noise. Hence, the goal of this thesis is to develop new advanced techniques for enhancing of a VLC link under various distortions considered.

In the first work, a hyperparameter-free random Fourier feature (RFF)-based receiver was proposed for OTFS to mitigate transmit side device nonlinearity. Further, analytical bounds for the performance of the proposed receiver are presented, which

were validated via computer simulations over VLC channels with user-mobility. The close overlap of the analytical BER with the simulated BER verifies the analytical contributions. The results obtained establish robustness of the proposed RFF-based post-distortion for the mitigation of transmit side nonlinearity for OTFS VLC based system with user-mobility.

In the previous work, the inherent sparsity of the OTFS VLC system was not exploited. Next, zero attracting least mean square (ZALMS)-based channel estimator is proposed for a VLC-OTFS system with the dispersive mobile multipath channel. Furthermore, it was observed from the simulations that due to the sparse nature of the VLC channel represented in the delay-Doppler domain, ZALMS performed better than the traditional least mean square (LMS) and orthogonal matching pursuit (OMP) algorithm. The simulated findings show that ZALMS is a more suitable low-complexity solution for channel estimation in the OTFS-VLC system.

In the previous works, the distortion effects resulting from user mobility and LED nonlinearity were discussed, with a primary focus on improving BER performance. However, transmission in visible light suffers from severe performance degradation due to LoS blockage, as visible light can not pass through obstacles due to its high penetration loss. Moreover, the illumination requirements of LEDs pose a challenge to the practical deployment of VLC. In this context, ORIS is proposed to address this issue. In the simulation-based 3D grid world, a subarray of ORIS elements is learned to align according to the multi-user positions. The proposed approach has significantly less overhead and is independent of the sizes of state and action spaces.

To further provide 360^0 coverage, the performance of an optical simultaneously transmitting and reflecting-RIS (OSTAR-RIS) is analyzed next. Most studies relied on on-off-keying (OOK) modulation in VLC systems. Color shift keying (CSK)-based VLC systems offer several advantages over conventional modulation schemes like OOK and pulse-amplitude modulation (PAM). A deep neural network (DNN)-based symbol detector was proposed for direct symbol detection and compared with the traditional LMS-based channel estimator.

In the previous works, VLC systems scenarios with no eavesdropper were considered. An eavesdropper can intercept transmitted data, gaining unauthorized access to sensitive information. In scenarios like VLC, where the broadcast nature of light makes the signals easily detectable, this risk increases. To address the growing data demands of users in VLC systems for beyond 5G communication, a novel multiple access scheme known as non orthogonal multiple access (NOMA) is proposed. The secrecy sum rate (SSR) performance of NOMA is compared with traditional orthogonal multiple access (OMA).

Contents

List of Figures

List of Tables

List of Abbreviations/Acronyms

3D-SOMP three-dimensional structured orthogonal matching pursuit.

ADC analog-to-digital converter.

AM/AM amplitude-to-amplitude.

AWGN additive white Gaussian noise.

BER bit error rate.

BPSK binary phase shift keying.

CB ceiling bounce.

CIR channel impulse response.

CSK color shift keying.

DAC digital-to-analog converter.

DCO-OTFS DC-biased optical orthogonal time frequency space.

DNN deep neural network.

EMI electromagnetic interference.

FoV field-of-view.

FSO free space optics.

i.i.d. independent and identically distributed.

ICI inter-carrier interference.

IoT internet-of-things.

ISFFT inverse symplectic fast Fourier transform.

ISI inter-symbol interference.

KLMS kernel least mean square.

LC liquid crystal.

LED light emitting diode.

LiFi light fidelity.

LMS least mean square.

LoS line-of-sight.

LS-RFF least square random Fourier feature.

MA mirror array.

MAP maximum a posteriori probability.

ML machine learning.

MMSE minimum mean square error.

MP matching pursuit.

MSA metasurface array.

MSD mean square deviation.

MSE mean square error.

MSP modified subspace pursuit.

NLFA non-linear function approximation.

NLoS non-line-of-sight.

NOMA non orthogonal multiple access.

OMA orthogonal multiple access.

OMP orthogonal matching pursuit.

OOK on-off keying.

OSTAR-RIS optical simultaneously transmitting and reflecting RIS.

OTFS orthogonal time frequency space.

OWC optical wireless communication.

PAM pulse-amplitude modulation.

PD photodetector.

PDF probability density function.

PEP pairwise error probability.

PSO particle swarm optimization.

ReLU rectified linear activation function.

RF radio frequency.

RFF random Fourier feature.

RIS reconfigurable intelligent surface.

RKHS reproducing kernel Hilbert space.

RL reinforcement learning.

RMS root-mean-square.

RWP random-way-point.

SBL sparse Bayesian learning.

SCMA sparse code multiple access.

SFFT symplectic fast Fourier transform.

SIC successive interference cancellation.

SINR signal-to-interference-plus-noise ratio.

SNR signal-to-noise ratio.

SSR secrecy sum rate.

UV ultraviolet.

UVC ultraviolet communication.

V2I vehicle-to-infrastructure.

V2V vehicle-to-vehicle.

VLC visible light communication.

VLMS Volterra least mean square.

ZALMS zero attracting least mean square.

List of Symbols

- Basic arithmetic and calculus notations with their definitions.

Elementary & Special Functions

Notation	Definition
$\Gamma(x)$	$= \int_0^{\infty} t^{x-1}e^{-t}\,\mathrm{d}t$ is the Gamma function.
$\Gamma(x,y)$	$= \int_y^{\infty} t^{x-1}e^{-t}\mathrm{d}t$ is the upper incomplete Gamma function.
$\Upsilon(x,y)$	$= \int_0^{y} t^{x-1}e^{-t}\mathrm{d}t$ is the lower incomplete Gamma function.
${}_1F_1(a,b;x)$	$= \sum_{r=0}^{\infty} \frac{(a)_r}{(b)_r}\frac{x^r}{r!}$ is the confluent hypergeometric function of first kind.
${}_2F_1(a,b;c;x)$	$= \sum_{r=0}^{\infty} \frac{(a)_r(b)_r}{(c)_r}\frac{x^r}{r!}$ is the Gauss hypergeometric function.
$\mathcal{W}_{\lambda,\mu}(x)$	$= \frac{x^{\mu+\frac{1}{2}}e^{-\frac{x}{2}}}{\Gamma\left(\mu-\lambda+\frac{1}{2}\right)} \int_0^{\infty} e^{-xt}t^{\mu-\lambda-\frac{1}{2}}\left(1+t\right)^{\mu-\lambda+\frac{1}{2}}\mathrm{d}t$ denotes the Whittaker function.
$I_v(x)$	$= \sum_{r=0}^{\infty} \frac{(\frac{1}{2})^{v+2r}}{r!\Gamma(v+r+1)}x^{v+2r}$ denotes the v^{th} order modified Bessel function of the first kind.
$\mathcal{K}_{\upsilon}(x)$	$= \frac{1}{2}\left(\frac{x}{2}\right)^{\upsilon}\int_0^{\infty}\frac{\mathrm{e}^{-t-\frac{x^2}{4t}}}{t^{\upsilon+1}}\mathrm{d}t$ represents the modified Bessel function of the second kind of order υ.
$D_n(x)$	$= 2^{\frac{1}{4}+\frac{n}{2}}\mathcal{W}_{\frac{1}{4}+\frac{n}{2},-\frac{1}{4}}\left(\frac{x^2}{2}\right)x^{-\frac{1}{2}}$ represents the Parabolic cylinder function.
$(x)_k$	$= \frac{\Gamma(x+k)}{\Gamma(x)}$ denotes the Pochhammer symbol.
$Q(x)$	$= \frac{1}{\sqrt{2\pi}}\int_x^{\infty} e^{-\frac{t^2}{2}}\mathrm{d}t$ is the Gaussian Q-function.

Probability & Statistics

Let X be a random variable (RV).

Notation	Definition
$\mathbb{E}[\cdot]$	statistical expectation operator
$\mathcal{P}(\cdot)$	statistical probability operator
$f_X(\cdot)$	probability density function (PDF) of a RV X
$F_X(\cdot)$	cumulative distribution function (CDF) of a RV X
$\mathcal{CN}(\mu,\sigma^2)$	complex normal distribution with mean μ and variance σ^2

Chapter 1

Introduction

1.1 Overview

In the recent years, the exponential growth in communication technology has created a drastic surge in bandwidth and capacity requirements. The growing need for expanded data and multimedia services has led to congestion within the conventionally utilized radio frequency (RF) spectrum. In response to this challenge, optical wireless communication (OWC) systems have emerged as a pivotal solution, capitalizing on distinctive features such as large bandwidth, license-free spectrum, high data rate, easy and quick deployment, and lower power requirements that set them apart. The mechanism of OWC involves the utilization of an optical carrier to convey information from the transmitter to the receiver through an unguided channel, typically free space or the Earth's atmosphere. As illustrated in Figure 1.1, OWC can be broadly categorized into three main types: visible light communication (VLC), ultraviolet communication (UVC) and free space optics (FSO). UVC harnesses ultraviolet (UV) radiation for signal transmission, capable of being dispersed and bounced off particles and aerosols suspended in the air. FSO communication systems can be more specifically categorized into terrestrial and space optical links. The indoor optical systems which include visible light communication systems, are the main focus of this thesis.

The human eye is most responsive to visible light, with the sun being the predominant natural source of visible light in nature. From the view of the electromagnetic spectrum as shown in Figure 1.2, the visible spectrum extends from about 390 to

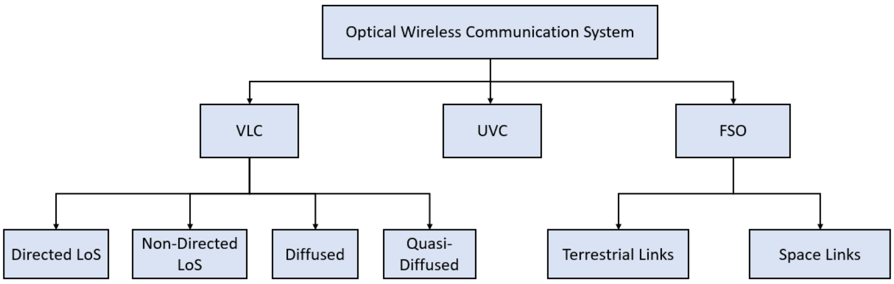

Figure 1.1: Classification of the optical wireless communication system.

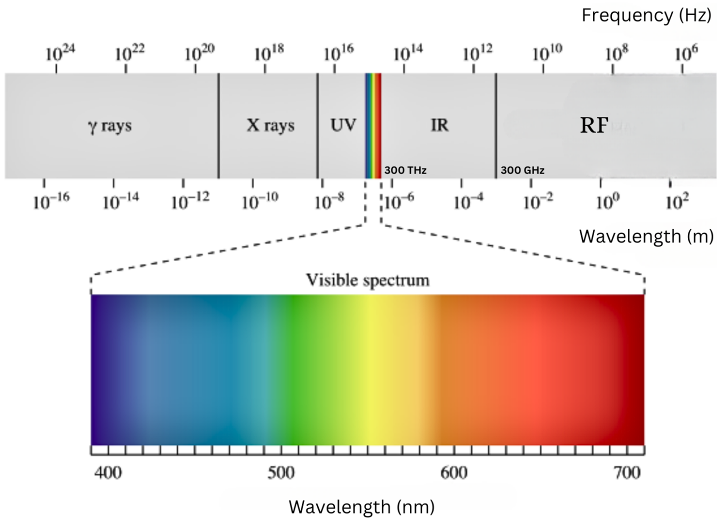

Figure 1.2: Electromagnetic spectrum

700 nm in terms of wavelength and 430 THz to 770 THz in terms of frequency, which is ten thousand times higher than radio waves, i.e. 770 THz as compared to a maximum of 300 GHz for radio waves. This suggests that light is capable of transmitting more pulses of data in much less time than radio waves.

VLC has become a good complementary technology to RF systems for facilitating high-speed data communication in next-generation wireless systems. It operates by modulating the intensity of light emitting diode (LED) lamps based on the input signal at an undetectable speed to the human eye. This enables the simultaneous accomplishment of both illumination and communication objectives. Photodiodes or photodetectors (PDs) are employed at the receiver end to convert the optical signal into electrical current. VLC has the following desired features over the conventional RF-based systems:

- **Wide spectrum**: Raising the carrier frequency enhances the information-carrying capacity of a communication system. In RF, the allowable bandwidth can be up to 20% of the carrier frequency. VLC has a license-free, huge bandwidth of 400 THz, which alleviates the spectrum crunch faced by RF communication systems. In VLC, even if the bandwidth is taken to be 1% of carrier frequency ($\sim 10^{16}$Hz), the allowable bandwidth would be 100 THz, which is 10^5 times that of RF carrier.

- **High directivity**: The gain of an antenna is dependent on its directivity. The superiority of an optical carrier compared to an RF carrier can be observed as

$$\frac{G_{optical}}{G_{RF}} \approx \frac{4\pi/\theta^2_{optical}}{4\pi/\theta^2_{RF}} \tag{1.1}$$

where θ_{RF} and $\theta_{optical}$ are RF and optical beam divergence, respectively. The beam divergence is proportional to λ/D where D is aperture diameter, and λ is carrier wavelength. As the optical wavelength is very small, high directivity and gain are obtained.

- **Cost-effective**: VLC-based systems offer a cost-effective and less complex implementation, leveraging the widespread presence of LEDs in existing infrastructures. The dual-purpose utilization of LEDs for both illumination and data transmission not only streamlines the deployment process but also enhances the overall cost-effectiveness of these systems. This inherent compatibility with prevalent infrastructure positions VLC as an accessible and economical solution for achieving efficient communication alongside illumination in various settings. The seamless integration of data transmission capabilities into the existing lighting framework further underscores the practicality and ease of adopting VLC technology.

- **Energy efficient**: VLC-based systems utilize LEDs as transmitters, which are recognized for their energy efficiency compared to incandescent light bulbs, placing them within the realm of environmentally friendly communication technology.

- **Security**: Unlike traditional wireless communication technologies such as RF that may extend beyond physical barriers, VLC restricts the transmission of information to the illuminated area. VLC has higher security compared to RF-based system as visible light can not pass through the opaque boundaries and hence prevents eavesdropping. Moreover, VLC systems can be implemented with additional security features, such as encryption and authentication protocols, further fortifying the communication link.

- **Electromagnetic interference (EMI)**: VLC-based communication systems exhibit a notable advantage in terms of resilience against electromagnetic interference, making them particularly suitable for deployment in environments sensitive to RF disturbances, such as hospitals and aircraft. As a result, VLC systems are less prone to the disruptive effects of competing signals and electromagnetic noise, ensuring a more reliable and undistorted communication environment.
- **Reusability**: VLC-based systems boast superior data density owing to the confined and highly directional nature of visible light beams. This characteristic allows for efficient data transmission along with spatial reusability within a closed environment. The focused nature of VLC beams enables multiple simultaneous communication links without interference, making it an ideal choice for applications requiring high data throughput in crowded spaces. This unique capability enhances the scalability and performance of VLC-based systems, making them well-suited for scenarios where maximizing data density is paramount.
- **High signal-to-noise ratio (SNR)**: As LEDs provides high illumination levels (typically of the order of 400-600 lux), high SNRs are practically achievable for VLC as compared to its RF counterparts. This advantage positions VLC as a favourable choice for scenarios where maintaining high SNRs is crucial for effective communication. The elevated illumination levels from LEDs contribute to the superior signal quality achievable in VLC setups.

Because of the aforementioned benefits, VLC finds applications in diverse fields, including light-fidelity (LiFi) systems, intelligent transportation systems (such as vehicle-to-infrastructure (V2I) communication and vehicle-to-vehicle (V2V) communication), smart lighting, underwater communication, internet of things (IoT) ecosystems, and wearable devices.

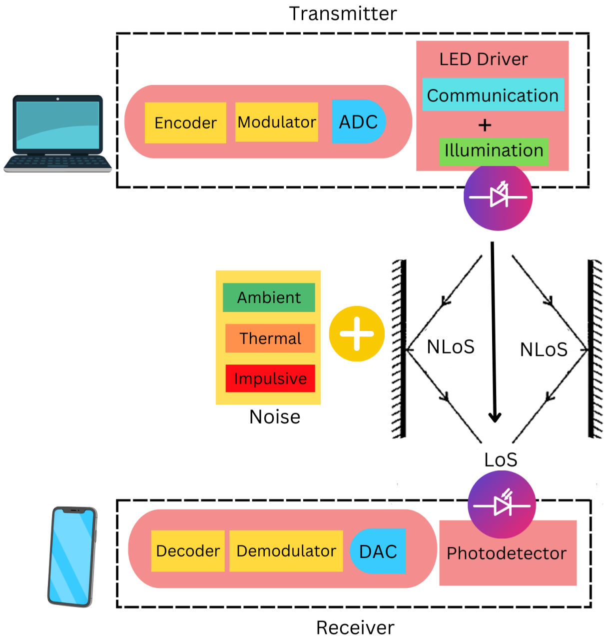

Figure 1.3: Architecture of visible light communication systems.

1.2 System Components and Architecture

A VLC system consists of several key components and follows a specific architecture to enable communication through visible light, as shown in Figure 1.3. In the VLC system, the optical signals emitted from the LEDs travel through complex communication channels consisting of line-of-sight (LoS) and non-line-of-sight paths (NLoS). The transmitter is composed of a modulator/encoder, digital-to-analog converter (DAC), and LED luminaires. First, the data bits are modulated using an appropriate modulation technique outlined in IEEE 802.15.7 standard for VLC systems. Further, reflection, diffusion, interference and noise in the channel cause the loss and distortion of the transmitted signal. The PD at the receiver, receives the modulated symbols transmitted through nonlinear LEDs. Similar to the transmitter block, the receiver block consists of a demodulator/decoder, analog-to-digital converter (ADC) and PD.

1.2.1 Light Sources

The advent of the LED has opened up new possibilities in the domain of VLC. The LED is a semiconductor that has the property that its frequency can be modulated rapidly at such a high speed that turning it on and off is undetectable by human eyes.

An LED luminaire consists of an LED driver and an LED lamp. The function of LED driver is to control the amount of current flowing through the LED depending on the type of modulation technique considered. For example, in the conventional on-off keying (OOK) scheme, the light is turned ON and OFF by using an LED driver circuit, where the 'ON' state is represented by the high-intensity level of light, and the 'OFF' state is represented by the low intensity of light. In most deployments, a white LED is generally used for transmission in VLC systems, which produce white light in either of the two ways:

- by using a blue LED coated with yellow phosphorous,
- by using three separate red, green and blue (RGB) LEDs, which generate white light by mixing red, green, and blue light.

Next, the signal is transmitted via a multipath VLC channel, which consists of both LoS and NLoS channel links creating multipath channel.

1.2.2 Photodetectors and Receivers

The signal transmitted by LED can be received by either of the two receivers:

- PD/non-imaging sensor,
- imaging/camera sensor.

PDs are used at the receiver for conversion of optical signal to electrical signal. visible light signals can also be received by camera sensors, which is a collection of several photodetectors arranged in an integrated circuit and are generally available in the smart mobile devices. However, data rates achieved by imaging sensors are very low due to its low sampling rate. PD is a crucial component in a VLC system, serving as the receiver to capture the modulated light signal. The key functions of the photodetector include:

- **Light Absorption**: When exposed to modulated light, the photodetector absorbs photons, generating electron-hole pairs within its semiconductor material.

- **Conversion to Electrical Current**: The absorbed photons release energy, causing the generation of free electrons and positively charged holes. This process results in the conversion of optical energy into an electrical current.

- **Signal Amplification**: The generated electrical current, representing the modulated information, is often weak. Therefore, amplifiers are employed to strengthen the signal for further processing.

- **Filtering and Demodulation**: The amplified signal may undergo filtering to isolate the desired frequency or information. Demodulation is then applied to extract the original data signal encoded in the light modulation.

- **Output to Receiver**: The final electrical signal, now containing the transmitted data, is sent to the receiver for further processing, decoding, and eventual utilization.

1.3 Channel Modelling

Channel modelling constitutes the initial and critical phase in the design of a VLC system, aiming for efficiency, reliability, and robustness. Numerous endeavours have been made to address VLC channel modelling, as indicated by various studies [2, 3].

Deterministic channel models

Deterministic channel models are usually based on the detailed description of a specific propagation environment, channel scenario, and the position and orientation of the LEDs and photodetectors or users. The ceiling bounce model is used to investigate the effect of multipaths due to reflection of light by various objects in an indoor environment. The channel impulse response (CIR) of the ceiling bounce (CB) model is given as

$$\mathbf{h}(\tau) = \frac{6\alpha^6}{(\tau + \alpha)^7} u(\tau)$$

where $\alpha = 12\sqrt{\frac{11}{13}} D_{RMS}$, D_{RMS} is the root-mean-square (RMS) delay spread of the multipath channel, and $u(\tau)$ is the unit step function. In the study by [4], Monte Carlo ray tracing is employed to assess the CIR within an empty room at visible light

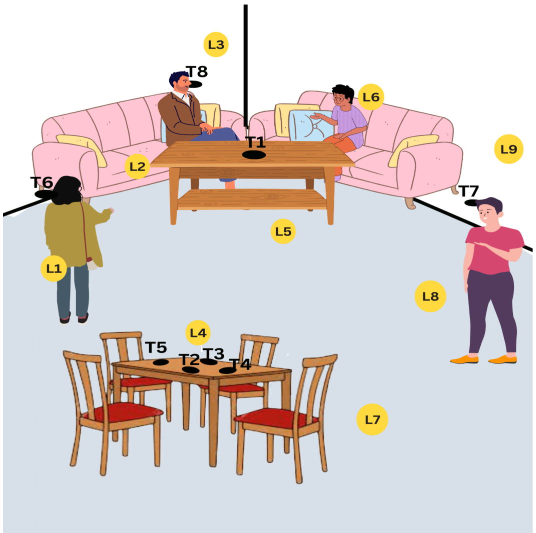

Figure 1.4: Home scenario for channel modelling using Zemax®

wavelengths. However, this approach overlooks wavelength dependency, assuming fixed reflectance values for surface materials. Similarly, in [2], the recursive method proposed in [5] is utilized to derive CIR in the visible light band, yet fixed reflectance is presumed. Addressing the impact of wavelength dependency in channel modelling, [6] computes reflectance values as the average of wavelength-dependent coefficients over the visible light band. Notably, [3] stands out as the sole work explicitly accounting for wavelength dependency. Here, a recursive method is employed to determine the CIR of an empty room. Nevertheless, akin to preceding studies, [3] is constrained by assumptions of solely diffuse reflections and ideal Lambertian sources, conditions that may not be universally applicable in practical scenarios.

In [7], the authors introduced an innovative approach to VLC channel modelling, addressing limitations present in previous models. They provide multiple CIRs tailored for diverse indoor environments, which are also incorporated into IEEE 802.15r1 PAN VLC channels. This methodology utilizes the ray tracing functionalities of the commercial optical and illumination design software Zemax®, allowing for a precise depiction of ray interactions emitted from lighting sources within specified confined spaces. Within the simulation environment created using Zemax®, users can define the geometry of the environment, objects present, and specifications of the light sources (LEDs) and receivers (PD). Leveraging the non-sequential ray tracing tool, the software computes detected power and path lengths from the light source to the detector for each ray, considering a specified number of rays and reflec-

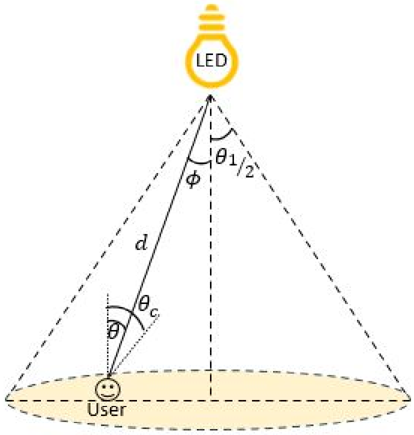

Figure 1.5: Line-of-sight channel gain model.

tions. Figure 1.4 shows the indoor home scenario considered for channel modelling using Zemax®by authors in [7]. The nine yellow circles (L1,$\cdots$,L9) are the nine luminaries, and there are eight test points (T1,$\cdots$,T8) represented by black circles. The Zemax®non-sequential ray tracing program generates an output file containing the detected power and path lengths for each ray from source to detector. This file is then imported into Matlab®, where the information is utilized to represent the CIR as:

$$h(t) = \sum_{i=1}^{N_r} P_i \; \delta(t - \tau_i) \tag{1.2}$$

where P_i is the power of the i^{th} signal, τ_i is the propagation time of the i^{th} ray, $\delta(t)$ is the dirac-delta function, and N_r is the number of receivers at the detector.

Several statistical channel models have been proposed for stationary and uniformly distributed users in prior works, such as [8]. The LoS channel gain, considering the direct path between the transmitter (LED) and the receiver photodetector as shown in Figure 1.5, is given as follows:

$$h_{LoS} = \frac{m+1}{2\pi d^2} A \cos^m(\phi) \cos(\theta) g(\theta) \tag{1.3}$$

where d is used to represent the distance between the LED transmitter and the PD, A is the area of the PD, ϕ is the light angle of incidence, θ is the angle of reception of the light at the photodiode, and $g(\theta)$ is the optical concentrator gain expressed as:

$$g(\theta) = \frac{n^2}{\sin(\theta_c)} \tag{1.4}$$

where n is the refractive index of the optical concentrator, θ_c is the field-of-view (FOV), and m is the order of Lambertian emission estimated as:

$$m = -\frac{1}{\log_2(\cos(\theta_{1/2})} \tag{1.5}$$

where $\theta_{1/2}$ is the semi-angle of the LED.

Stochastic channel models

In stochastic models, the impulse responses of OWC channels are characterized by the law of wave propagation applied to specific LEDs, photodetector, and scatterer geometries, which are predefined in a stochastic fashion according to certain probability distributions. In recent studies, like those in [9, 10], researchers used the random-way-point (RWP) mobility model to study the SNR in indoor LiFi systems. For the RWP model, the channel's probability distribution function (pdf) is specified as follows:

$$p(h) = \begin{cases} \sum_{l=1}^{4} K_l h^{-\beta_l}, & h_{min} \leq h \leq h_{max}; \\ 0, & \text{otherwise} \end{cases} \tag{1.6}$$

where $K_1 = K[27 + \frac{35D^2}{r_{max}^2} + \frac{8D^4}{r_{max}^4}]$, $K_2 = -K\frac{35}{r_{max}^2}\mathfrak{S}^{\frac{2}{a+3}}$, $K_3 = -K\frac{8}{r_{max}^4}\mathfrak{S}^{\frac{4}{a+3}}$, and $K_4 = -K\frac{16D^2}{r_{max}^4}\mathfrak{S}^{\frac{2}{a+3}}$, $K = \frac{12\mathfrak{S}^{\frac{2}{a+3}}}{73(a+3)r_{max}^2}$, $\beta_1 = \frac{2}{a+3} + 1$, $\beta_2 = \beta_4 = \frac{4}{a+3} + 1$, and $\beta_3 = \frac{6}{a+3} + 1$, where $\mathfrak{S} = b(a+1)D^{a+1}$, $b = \frac{R}{2\pi}$. The line of sight distance of the LED from the user is denoted as D, the effective geometric area of the detector is denoted by R, and r_{max} is the radius of the maximum coverage area. $h_{min} = \frac{\mathfrak{S}}{(r_{max}^2 + D^2)^{\frac{a+3}{2}}}$, $h_{max} = \frac{\mathfrak{S}}{D^{(a+3)}}$ and, $a = \frac{-1}{\log(\cos(\phi_{\frac{1}{2}}))}$ where $\phi_{\frac{1}{2}}$ is the half-angle of the fixature of the LED transmitting.

1.4 Challenges and Open Issues in VLC

The practical deployment of VLC faces several challenges, which can impact its widespread adoption. Various such challenges are discussed in detail in subsequent subsections:

1.4.1 Noise Sources

The dominant noise sources in a typical VLC system, as shown in Figure 1.3, are given in detail as follows:

Ambient noise

Ambient light noises may arise from sunlight, skylights, incandescent and fluorescent lamps, and other light sources present in the indoor environment. The presence of ambient light gives rise to DC photocurrent, inducing shot noise. The variance of this shot noise originating from ambient light (represented as $\sigma^2_{ambient}$) can be expressed as:

$$\sigma^2_{ambient} = 2qM^2F(I_b + I_x)B \tag{1.7}$$

where q symbolizes the charge of the electron, M corresponds to the average gain of the PD, B represents the bandwidth of the PD, I_b refers to the average photocurrent generated at the PD due to the average optical power received from sunlight, I_x signifies the average photocurrent generated at the PD due to the average optical power received from the LED, and F is characterized as the excess noise calculated as:

$$F = rM + \left(2 - \frac{1}{M}\right)(1 - r) \tag{1.8}$$

where r symbolizes the hole-to-electron ionization rate. The ambient light noise can be approximated by Gaussian distribution with mean 0 and variance $\sigma^2_{ambient}$. Ambient light noise has been considered in the literature.

Thermal noise

The variance of the thermal noise ($\sigma^2_{thermal}$) is given by

$$\sigma^2_{thermal} = 4\left(\frac{K_BT}{R_L}\right)F_nB \tag{1.9}$$

where K_B is the Boltzmann constant, T is the temperature (in Kelvin), F_n is the PD noise, and R_L is the load resistance (typically of the order of 50 Ω). Thermal noise can be modelled by Gaussian distribution with mean 0 and variance $\sigma^2_{thermal}$.

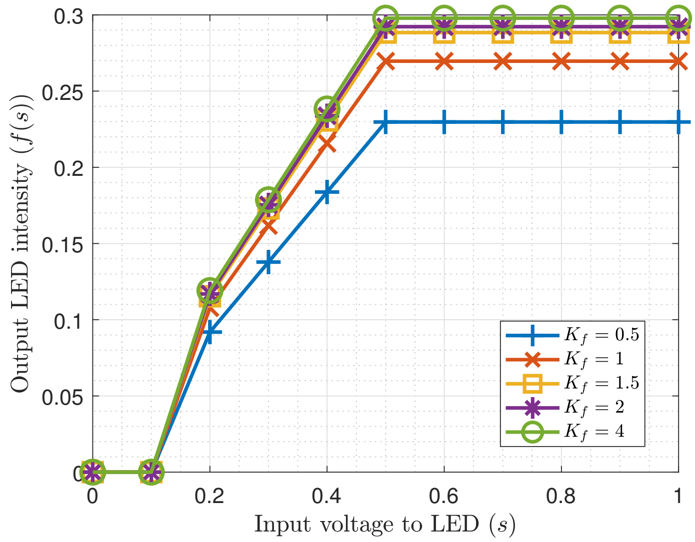

Figure 1.6: Transfer characteristics of the Rapp's nonlinear model for light emitting diode

Impulsive noise

The Middleton Class-A noise model is the most considered statistical noise model-based on Poisson-Gaussian to model impulsive noise induced due to imperfect optical components and other factors such as lightning, sunlight, etc. The Poisson process is employed to depict the likelihood of impulsive noise events occurring, while the Gaussian process is utilized to describe the amplitude distribution of said impulsive noise. The effective variance of the Class-A noise model is determined by:

$$\sigma^2_{impulse} = K\frac{\sigma_b^2}{A} \tag{1.10}$$

where $\sigma^2_{impulse}$ is the variance of the impulsive noise and σ_b^2 is the variance of the background noise, K represents the average power of the impulsive noise, and the parameter A represents the probability of impulsive noise on the time axis.

Hence, the overall noise in a VLC system is an independent and identically distributed (i.i.d) complex additive white Gaussian noise (AWGN) with zero mean and variance σ^2, where $\sigma^2 = \sigma^2_{ambient} + \sigma^2_{thermal} + \sigma^2_{impulse}$.

1.4.2 Nonlinear Characteristics of LEDs

LEDs are widely deployed in the existing infrastructure and have completely replaced conventional fluorescent and incandescent lamps due to its several desirable features, like lifetime, light density, reliability, and energy efficiency. The response of LEDs displays nonlinearity due to the nonlinear conversion of current to voltage and current to optical power. Specifically, the characteristics of LEDs become nonlinear in the presence of signals with a substantial dynamic range and at high switching frequencies. LED's nonlinear models are mainly divided into memoryless and memory nonlinear models. The memoryless nonlinear block is modelled by Rapp's model, which can be mathematically written as amplitude-to-amplitude (AM/AM) modelling as follows:

$$f(s) = \frac{s - v_{th}}{(1 + (\frac{s - v_{th}}{i_{sat}})^{2k_f})^{\frac{1}{2k_f}}} \tag{1.11}$$

where i_{sat} is the saturation current, $f(s)$ the output LED intensity, v_{th} is the cut-in voltage of the LED, and k_f controls the level of nonlinearity, also termed as knee factor. k_f controls the smoothness of transition from linear to the saturation region, as can be seen in Figure 1.6. Furthermore, the capacitance and conductance of an LED are frequency-dependent, which results in LED's nonlinearity with memory effects.

1.4.3 Impact of User Mobility and Multipath Effects

The performance of a VLC link degrades as a result of mobile receivers or transmitters causing relative motion between the transmitter and the receiver, and the presence of multipath between the transmitter and receiver. In addition to the LoS component, multiple reflections among the ceiling, floor, and walls of the room for an indoor VLC scenario result in NLoS components for a VLC link. Hence, the VLC channel is frequency selective in nature and results in severe inter-symbol-interfernce (ISI), particularly under the high data rate regime, i.e., when the delay spread is larger than the symbol period. In real-world scenarios, users may engage in activities such as reading, talking on a cell phone, or shopping in a mall while in motion. This dynamic behaviour introduces a probabilistic nature to the overall VLC sys-

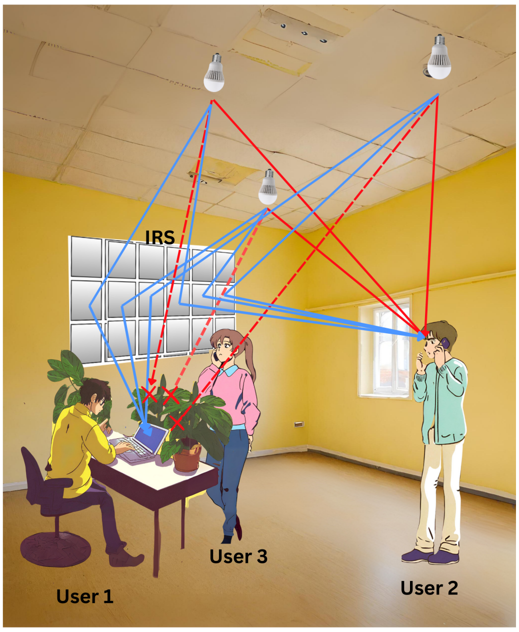

(a)

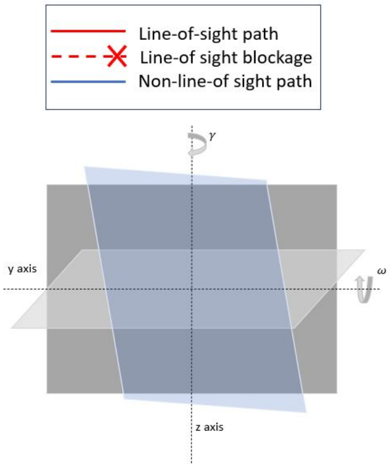

(b)

Figure 1.7: Reflecting intelligent surface-aided indoor visible light communication system model.

tem. The effect of user mobility leads to an effective multiplicative distortion that degrades the VLC link due to dispersion in the time domain, causing inter-carrier interference (ICI).

1.4.4 Blind Spots: Absence of Direct Link

Despite VLC's promise as a viable supplement to RF-based communication systems, the performance of a VLC system is significantly limited by the absence of direct links or blockage of the LoS channel, which creates blind spots as shown in Figure 1.7(a). As visible light cannot penetrate obstacles, it is reflected back due to the high penetration loss. In Figure 1.7(a), User 2 and User 3 have direct LoS and NLoS links available, while User 1 is in a blind spot with User 1 and plants blocking the LoS paths. In this context, to facilitate the data requirements of users like User 1, optical reflecting intelligent surface (RIS) has recently been introduced in the literature as a promising solution to overcome the drawbacks of LoS blockages and broaden the coverage area by reconfiguring the propagation environment [11]. Figure 1.7(b) shows the roll and yaw angle of the RIS which can be optimized as per user location.

1.5 Motivation

VLC systems are emerging as a viable alternative to traditional wireless communication technologies, especially in indoor environments where RF spectrum is limited. VLC offers numerous advantages, such as high bandwidth availability, enhanced security, and immunity to RF interference, making it ideal for applications in smart homes, offices, and industrial settings. However, there are significant technical challenges associated with optimizing VLC systems, including managing the effects of relative mobility between LEDs and user, nonlinearities in optical components, accurately estimating channel characteristics in multipath environments, and achieving high data rates while ensuring reliability in complex dynamic scenarios. To address Doppler effects due to user mobility orthogonal time frequency space (OTFS) modulation offers promising solution. Assessing the performance of OTFS in nonlinear VLC systems is essential to understand its feasibility and robustness in practical applications where LED nonlinearity can degrade system performance.

The OTFS channel mapped in delay-Doppler domain is inherently sparse. The zero attracting least mean square (ZALMS) algorithm can efficiently estimate sparse channels, but its performance needs to be evaluated in the context of multi-carrier VLC systems to ensure robustness and accuracy in real-world deployments. Further, the requirement of the next-generation wireless communication system can be fulfilled by employing smart technologies i.e., RIS.

The RIS-aided communication systems can achieve the stringent requirements of the 5G and beyond systems, such as ultra-high data rate, global coverage, and connectivity, extremely high reliability, and low latency. RIS have shown promise in enhancing signal quality and coverage in indoor VLC systems by dynamically adjusting the reflection and direction of light. By leveraging reinforcement learning for rate maximization, an RIS-assisted VLC system can adapt to environmental changes and user movement, optimizing data rates while maintaining energy efficiency. Integrating non orthogonal multiple access (NOMA) with optical simultaneously transmitting and reflecting-RIS (OSTAR-RIS) provides opportunities to enhance user multiplexing and improve spectral efficiency in VLC systems. Evaluating such configurations will provide insights into their potential to support multiple users efficiently within the limited spectral resources of VLC.

Color shift keying (CSK) modulation can further increase data transmission rates in VLC by utilizing different colors of LEDs i.e. red, green and blue. By combining this modulation with deep neural network (DNN)-based symbol detection, VLC systems with OSTAR-RIS support can achieve higher accuracy in symbol decoding, even in complex indoor environments with substantial interference and multipath effects.

1.6 Thesis Flowchart, Outline, and Contributions

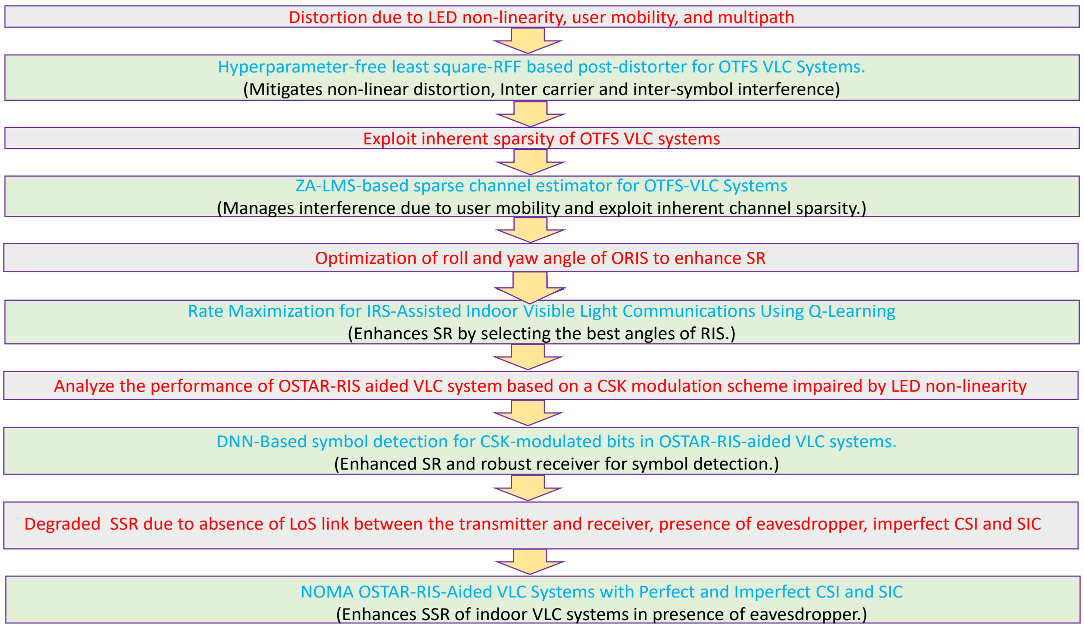

Figure 1.8: Flowchart of the thesis.

The flowchart of the thesis is shown in Figure 1.8 which shows the advancement of future wireless communication technology with their capability. The thesis is organized into 7 chapters, which are briefly described with their contributions as follows:

Chapter 1. Introduction : In chapter 1, a brief introduction to the VLC channel, user mobility, blind spots, channel characterization, various performance metrics, simultaneous information transfer, OTFS, an RIS, hardware imperfections like nonlinear LED impairments, ISI, ICI, and finally, the motivation and major contributions of the work presented in the thesis are provided.

Chapter 2. OTFS Modulation aided nonlinear VLC Systems: In this chapter, the performance of OTFS modulation in nonlinear VLC systems is investigated. VLC systems, suffers from degradation due to LED nonlinearity, multipath and relative mobility between the transmitter and the receiver. OTFS modulation is proposed addresses impairments due to multipath and user-mobility. To mitigate the distortions due to LED nonlinearity, hyperparameter-free RFF-based post-distorter is proposed. Analytical bounds for the bit-error-rate (BER) performance of the proposed post-distorter are presented, and validated via simulations over realistic VLC channels.

Chapter 3. ZALMS-based sparse channel estimator in multi-carrier VLC system: In the last chapter, the inherent channel sparsity of OTFS modulated VLC systems was not exploited. Effective representation of the channel in the delay-Doppler domain is inherently sparse when the number of channel paths is small compared to the number of symbols transmitted per frame. In this chapter, a formal analysis of the convergence and bit-error rate of the proposed ZA-LMS algorithm is presented, along with supporting simulations. The performance of the proposed algorithm with the traditional least mean square (LMS) and orthogonal matching pursuit (OMP) algorithm is compared.

Chapter 4. Rate Maximization for RIS-Assisted Indoor VLC Systems: In the previous chapter, the distortion effects resulting from user mobility and LED nonlinearity were addressed, with a primary focus on improving BER performance. Moreover, the illumination requirements of LEDs pose a challenge to the practical deployment of VLC. In this chapter, an optimization problem to find the optimum angles for RIS corresponding to different user positions to maximize the long-term discounted sum rates is formulated. The proposed function-approximation algorithm needs lower updates, irrespective of the state size and action space, which is a significant improvement in terms of computational needs.

Chapter 5. CSK Modulation Scheme and DNN-Based Symbol Detection in OSTAR-RIS-aided VLC Systems: In the previous chapter, the performance of a ORIS is analyzed for VLC systems. In this chapter to further provide 360^0 coverage, the performance of an OSTAR-RIS aided VLC system based on CSK modulation scheme is analyzed. For performance analysis, a closed-form expression of the achieved BER is derived. Further, the impact of impairments and other parameters on the system performance are highlighted.

Chapter 6. NOMA OSTAR-RIS-Aided VLC Systems: In the previous chapter, the achievable user rate and BER performance of nonlinear VLC system was enhanced by employing CSK modulation scheme and DNN-based detection scheme. In this chapter, in addition to low coverage area, and loss of the VLC signal due to the absence of a direct link between the transmitter and the receiver caused by blockages present in the environment the impact of eavesdropper on secrecy sum rate (SSR) of a VLC system is analyzed. The performance of NOMA OSTAR-RIS VLC is compared with the benchmark methods. Detailed simulation results demonstrate that the NOMA scheme outperforms the orthogonal multiple access (OMA) scheme for the proposed system, particularly in terms of the SSR.

Chapter 7. Conclusions and Future Works: All the contributions of the thesis have been summarized in this chapter, and important insights and conclusions have been presented. Further, the scope for future works is also discussed.

Chapter 2

OTFS Modulation in Nonlinear VLC Systems

VLC has emerged as a viable green supplement for traditional RF communication due to its unique features, such as wide licence free spectrum, low EMI, higher security, and low cost [12]. Although promising, the performance of a VLC system is known to degrade due to the following two limiting factors: (1) nonlinear characteristic of LED [13] that adds an equivalent additive distortion at the receiver, and (2) user-mobility and ISI which leads to time-domain and frequency-domain spreading respectively [14]. Conventional modulation schemes for VLC such as, optical-orthogonal frequency division multiplexing (O-OFDM) are capable of mitigating ISI due to time-domain dispersion caused by multipath reflections [15]. For O-OFDM-based VLC system, various pre-distorters [13] and post-distorters [16] are used to mitigate the effect of LED nonlinearity. Further, user mobility leads to variations in VLC channel-gains, that in-turn, leads to lowering of instantaneous SNR [14]. To jointly mitigate impairments due to user mobility and multipath dispersion, recently, OTFS modulation technique has been proposed [17].

There are primarily two ways to mitigate the effect of LED nonlinearity i.e. by using pre-distorters and post-distorters. Pre-distortion techniques are known to outperform static inversion, however, it requires perfect feedback of the channel state information (CSI) from the receiver to the transmitter in a closed loop. To alleviate the need for precise feedback, authors in [18–20] substituted pre-distorters with open loop post-distorters based on Volterra and Hammerstein polynomials. However, the Volterra (ex. Volterra least mean square (VLMS)) and Hammerstein-based approaches have high computational complexity and suffer from modelling impairments due to truncation of polynomial series. Thus, due to their universal representation, open loop reproducing kernel Hilbert space (RKHS) based post-distortion methods have been proposed recently. RKHS-based approaches are computationally simple and provide superior BER performance. Among the existing RKHS-based post-distortion techniques, the kernel least mean square (KLMS) and kernel minimum symbol error rate (KMSER) are the most popular. RKHS-based post-distorter based on KLMS/KMSER algorithm delivers better performance over polynomial series-based post-distorters. However, KLMS/KMSER-based approaches rely on growing dictionary of data sets, which is difficult to implement practically. Furthermore, the feature function of Gaussian kernel allows for approximation as random Fourier feature (RFF). However, the performance of RKHS-based techniques whether dictionary-based or RFF is highly sensitive to the choice of kernel-width parameter. Building on this observation, in this chapter hyperparameter-free RFF-based post-distorter for OTFS VLC System is proposed. Extensive research is required to exploit VLC-OTFS systems in the beyond 5G communication system. Authors in [21] have proposed direct current optical-OTFS (DCO-OTFS) based relay-assisted VLC system to enhance the spectral efficiency. To enhance VLC links and for generic impairment-mitigation, hyperparameter-free RFF-based post-distorters have emerged as promising solution for the OTFS VLC system. The main contributions of this chapter are:

- OTFS for VLC system impaired by both multipath and user mobility is proposed. For our studies, CIR measurements generated using Zemax software for realistic trajectories are considered [14].

- To mitigate distortions due to LED nonlinearity the hyperparameter-free least square-RFF (LS-RFF) based post-distorter is proposed for OTFS, and its BER performance is evaluated.

- A lower bound on the BER of the proposed RFF-based post-distorter is obtained analytically and validated via computer simulations over nonlinear VLC channels with varying severity levels.

2.1 System Model

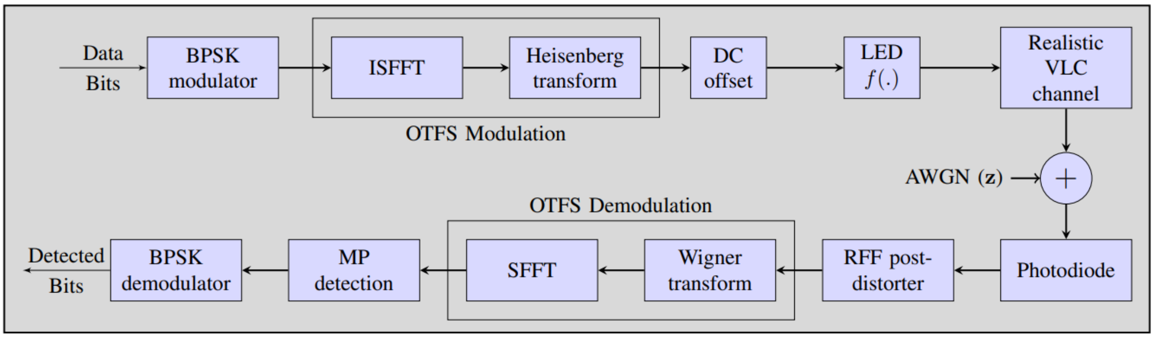

Figure 2.1: Block diagram of the considered system model.

In this section, the system model for the VLC-OTFS system impaired by LED nonlinearity and the multipath channel is described in Figure 2.1. The number of symbols transmitted per frame is $N_s = UV$, where U and V are the number of symbols and the number of sub-carriers, respectively. The transmitted binary phase shift keying (BPSK) symbols mapped in delay-Doppler domain are represented as $\mathbf{x} \in \mathbb{C}^{N_s \times 1}$. Two dimensional (2D) inverse symplectic fast Fourier transform (ISFFT) is applied on input BPSK modulated vector $\mathbf{x}$ to transform it into time-frequency domain such that:

$$\mathbf{X}_{v,u} = \sum_{l=0}^{U-1} \sum_{k=0}^{V-1} \mathbf{x}_{l,k} e^{-j2\pi(\frac{ul}{U} - \frac{vk}{V})}. \tag{2.1}$$

In the second step, Heisenberg transform on the output of the ISFFT $\mathbf{X}$ is applied to transform it into time-domain:

$$\tilde{\mathbf{x}}(t) = \sum_{u=0}^{U-1} \sum_{v=0}^{V-1} \mathbf{X}_{v,u} e^{j2\pi u \Delta f (t - vT)} g_x(t - vT), \tag{2.2}$$

where $g_x(t)$ is the transmitted pulse. In the time-frequency domain sampling is done at intervals T and Δf, respectively, to obtain a 2D lattice $\Lambda = (vT, u\Delta f)$, where $v = 0, \ldots, V-1$, and $u = 0, \ldots, U-1$. After OTFS modulation, a cyclic prefix of length $(C_p - 1)$ is affixed to the output before transmitting, where C_p is the number of channel paths. After adding cyclic prefix, the DC bias is added to the transmitted signal to bring the LEDs into the forward bias (operating) region. Next, symbols are transmitted through LED with nonlinear characteristics. As LEDs have amplitude-to-amplitude (AM/AM) modelling, nonlinear characteristics of LED is modelled by Rapp's model as follows:

$$f(\tilde{\mathbf{x}}) = \frac{\tilde{\mathbf{x}}}{(1 + (\frac{\tilde{\mathbf{x}}}{i_{sat}})^{2k_f})^{\frac{1}{2k_f}}}, \tag{2.3}$$

where i_{sat} is the saturation current of the LED and k_f is the knee factor which controls smoothness of the transition from the linear to the saturation region. The output is transmitted over mobile-multipath VLC channel $\mathbf{H}(\tau, \nu)$ [14], defined as:

$$\mathbf{H}(\tau, \nu) = \sum_{i=1}^{C_p} h_i \delta(\tau - \tau_i) \delta(\nu - \nu_i), \tag{2.4}$$

where ν_i, τ_i, h_i are Doppler shift, delay and channel gain, respectively, for the i^{th} cluster, and $\delta(\cdot)$ denotes the Dirac delta function.

Due to LED nonlinearity, the bit vector transmitted is denoted by $f(\tilde{\mathbf{x}})$. Therefore, the received signal at the photodiode after discarding the cyclic prefix can be written as [17]:

$$\begin{aligned} \mathbf{r}(t) &= \int_{\nu} \int_{\tau} \mathbf{H}(\tau, \nu) f(\tilde{\mathbf{x}}(t - \tau)) e^{j2\pi\nu(t-\tau)} d\tau d\nu + \mathbf{z}(t), \\ \mathbf{r} &= \mathbf{H} \otimes f(\tilde{\mathbf{x}}) + \mathbf{z}, \end{aligned} \tag{2.5}$$

where $\mathbf{z} \in \mathbb{C}^{N_s \times 1}$ is independent and identically distributed (i.i.d.) AWGN whose t^{th} entry is defined as $\mathbf{z}_t \sim \mathcal{CN}(0, \sigma_z^2)$. At the receiver, the symbols received by the photodiode are in the time-domain $\mathbf{r}(t)$ and are mapped back to the information domain after post distortion. First, the time-domain symbols are mapped back to time-frequency domain $\mathbf{Y}_{v,u}$ by applying Wigner transform:

$$: \mathbf{Y}_{v,u} = \int \mathbf{r}(\tau) r_x^*(\tau - t) e^{-j2\pi f(t-\tau)} d\tau, \tag{2.6}$$

where r_x^* is the conjugate of the received pulse r_x. Receiving and transmitting pulses g_x and r_x are ideal such that they satisfy the property of biorthogonality. Then symplectic fast Fourier transform (SFFT) is applied on output of Wigner transform $\mathbf{Y}_{v,u}$ [17] to transform signal mapped in the time-frequency domain to the information domain:

$$\mathbf{y}_{l,k} = \frac{1}{\sqrt{UV}} \sum_{v=0}^{V-1} \sum_{u=0}^{U-1} \mathbf{Y}_{v,u} e^{-j2\pi(\frac{ul}{U} - \frac{vk}{V})}. \tag{2.7}$$

Therefore, the input-output relation of the considered system model in the information domain, i.e. delay-Doppler domain, can be equated as:

$$\mathbf{y} = \mathbf{H_{eff}} \mathbf{x} + \tilde{\mathbf{z}}, \tag{2.8}$$

where $\mathbf{H_{eff}}$ is the effective channel matrix in information domain, and $\tilde{\mathbf{z}}$ is the noise which has the same statistical properties of $\mathbf{z}$. In the next section, a hyperparameter-free LS-RFF based post-distorter is proposed for the mitigation of transmit-side LED nonlinearity, and its performance bounds are derived.

2.1.1 Channel Model

The CIRs are obtained through ray-tracing by Zemax by authors in [14]. For the CIR modeling, a transmit LED-bandwidth of 20 MHz and a transmit baud-rate of 1 Gbps is considered. The channel-gain is dependent on the indoor spatial structure, user trajectory and user equipment orientation. To integrate these physical parameters into the VLC channel modelling, a framework which allows defining trajectories within an indoor environment and obtaining channel-gains along them is presented. In addition, the user orientation and the posture of the receiver terminal are defined, and the user is only allowed to move along coordinates without furniture/objects. Denoting the current location of the user as (x_p, y_p) and the next location is (x_n, y_n), the movement is modeled as:

$$x_n = x_p + \Delta r \cos\theta_d, \tag{2.9}$$

$$y_n = y_p + \Delta r \sin\theta_d, \tag{2.10}$$

where δr is the radial-change and θ_d is the movement direction. We assume that δr is equal to 40 cm, and θ_d is a uniformly distributed random variable between 0 and 2π . The user is initially assumed to face the wall for the considered trajectory shown in Fig. 2.2. The rotation of user is changed according to the direction of the trajectory while the rotation (i.e., 45^0) and location of cell phone in his/her hand are fixed with respect to the user's ear.

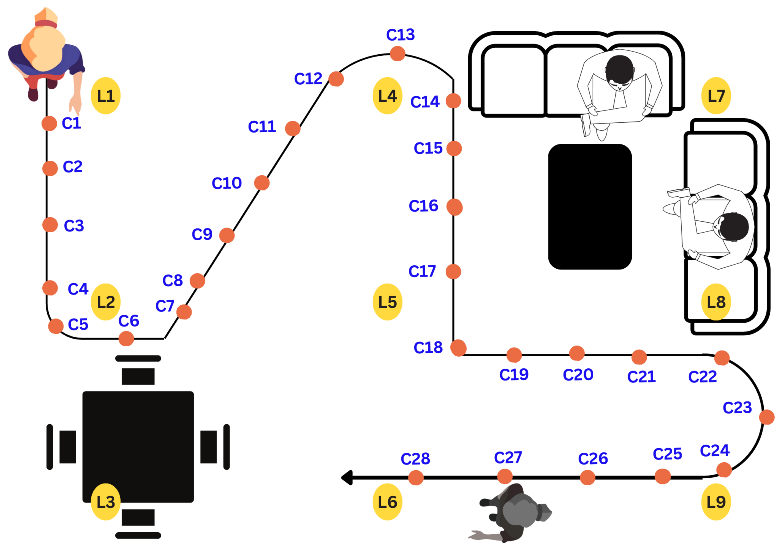

Figure 2.2: Trajectory under consideration [14].

2.2 Hyperparameter-free LS-RFF

In this section, a hyperparameter-free LS-RFF based post-distorter for mitigating transmit-side nonlinearity for the considered OTFS-VLC system is proposed. Owing to the superior performance of RFF-based technique in RKHS over the classical polynomial-based techniques such as VLMS and advantage of finite-memory budget over other RKHS-based methods,a hyperparameter-free-based approach is proposed to alleviate the need for estimating the hyperparameter i.e. kernel-width. Notably, the hyperparameter-free RFF are viable for mitigation of arbitrary transmit-side nonlinearity without the knowledge of hyperparameters like kernel-width or the explicit nature of the underlying nonlinearity.

Reference waveforms $\mathbf{r}_{ref}$ are considered at the receiver corresponding to the pre-determined pilots $\tilde{\mathbf{x}}_{ref}$. Further, without loss of generality, the first N_{tr} subcarriers of $\mathbf{r}_{ref}$ are used for training, the same is denoted as $\mathbf{r}_{ref} < 1 : N_{tr} >$, corresponding to pilots $\tilde{\mathbf{x}}_{ref} < 1 : N_{tr} >$. Further, the augmented regressors by concatenation of the real and imaginary parts are denoted as follows:

$$\mathbf{r}^c_{ref} < 1 : N_{tr} >= [\text{real}(\mathbf{r}_{ref} < 1 : N_{tr} >); \text{imag}(\mathbf{r}_{ref} < 1 : N_{tr} >)], \qquad (2.11)$$

and

$$\tilde{\mathbf{x}}_{ref}^{c} < 1 : N_{tr} >= [\mathrm{real}(\tilde{\mathbf{x}}_{ref} < 1 : N_{tr} >); \mathrm{imag}(\tilde{\mathbf{x}}_{ref} < 1 : N_{tr} >)]. \tag{2.12}$$

Further, the regressors are mapped to RKHS by the hyperparameter-free RFF, which, for n_G RFFs, is denoted as follows:

$$\mathbf{\Phi}(\mathbf{r}_{ref}^{c} < 1 : N_{tr} >) = \sqrt{\frac{2}{n_G}} \cos\left(\mathrm{diag}[\zeta]\mathbf{A}\mathbf{r}_{ref}^{c} < 1 : N_{tr} > +\mathbf{b}\right), \tag{2.13}$$

where the vectors ζ is drawn from a Gamma distribution, $\mathbf{\Gamma}[\alpha, \beta]$, and mapping coefficients $\mathbf{A}$ and $\mathbf{b}$ are drawn respectively from a zero mean normal distribution with unit variance, and uniformly distributed random variable in the interval $[0, 2\pi]$. Further, the parameters of the Gamma distribution can be initialized as follows:

$$\alpha = \frac{UV}{2},$$
$$\beta = \epsilon,$$

where ϵ is an arbitrarily small constant. Using these hyperparameter free RFFs, the estimate of the autocorrelation matrix, $\hat{\mathbf{R}}_{\mathbf{\Phi}}$, is expressed as follows:

$$\hat{\mathbf{R}}_{\mathbf{\Phi}} = \frac{1}{N_{tr}} \sum_{m=1}^{N_{tr}} \mathbf{\Phi}(\mathbf{r}_{ref}^{c} < 1 : N_{tr} >)\mathbf{\Phi}(\mathbf{r}_{ref}^{c} < 1 : N_{tr} >)^{T}. \tag{2.14}$$

and the cross covariance is expressed as:

$$\hat{\mathbf{r}}_{\mathbf{\Phi}} = \frac{1}{N_{tr}} \sum_{m=1}^{N_{tr}} (\tilde{\mathbf{x}}_{ref}^{c} < 1 : N_{tr} >)\mathbf{\Phi}(\mathbf{r}_{ref}^{c} < 1 : N_{tr} >). \tag{2.15}$$

which allows for the following estimate of the equalizer weights,

$$\mathbf{w} = \hat{\mathbf{R}}_{\mathbf{\Phi}}^{-1}\hat{\mathbf{r}}_{\mathbf{\Phi}}. \tag{2.16}$$

which, in-turn, allows for the following unwarped/equalized estimate, $\mathbf{r}_{unwarped}^{c}$, as follows:

$$\mathbf{r}_{unwarped}^{c} = \mathbf{w}^{T}\mathbf{\Phi}(\mathbf{r}_{ref}^{c}). \tag{2.17}$$

The MSE of the proposed receiver, σ_e^2, can be given as follows:

$$\sigma_e^2 = 1 - \hat{\mathbf{r}}_{\mathbf{\Phi}}^T \hat{\mathbf{R}}_{\mathbf{\Phi}}^{-1} \hat{\mathbf{r}}_{\mathbf{\Phi}}. \tag{2.18}$$

which allows for the following the SNR:

$$\gamma = \frac{1}{\sigma_e^2 + \sigma_z^2}. \tag{2.19}$$

which, in turn, results in the following lower bound for BER [22],

$$\text{BER} \geq \frac{UV - 1}{2^{UV}} Q(\sqrt{2\gamma}). \tag{2.20}$$

Putting the value of γ from (2.19), finally the lower bound of BER is:

$$\text{BER} \geq \frac{N_s - 1}{2^{N_s}} Q\left(\sqrt{\frac{2}{\sigma_e^2 + \sigma_z^2}}\right). \tag{2.21}$$

The accuracy of the proposed post-distorter can be validated in Figure 2.3. The accuracy of the model can be estimated as:

$$\text{Accuracy} = \frac{\text{Total number of correct estimations}}{\text{Total number of bits transmitted}} \times 100, \tag{2.22}$$

From Table 2.1, it is observed that for SNR=0 dB in both Case-1 where $k_f = 0.5$, and $i_{sat} = 1$, and Case-2 where $k_f = 0.5$, and $i_{sat} = 0.5$, the accuracy of the proposed model is $\sim$ 59%. However, as the SNR is increased to 10 dB the accuracy is enhanced to 87.32% for Case-1 and 87.3% for Case-2. On further increasing the SNR, the proposed model achieves an accuracy of more than 99%.

Table 2.1: Accuracy of proposed hyperparameter-free RFF-based post-distorter.

SNR	**Case 1:** $k_f = 0.5$, **and** $i_{sat} = 1$	**Case 2:** $k_f = 0.5$, **and** $i_{sat} = 0.5$
0 dB	59.89%	59.24%
10 dB	87.32%	87.3%
20 dB	99.78%	99.04%
30 dB	99.96%	99.92%
40 dB	99.99%	99.99%

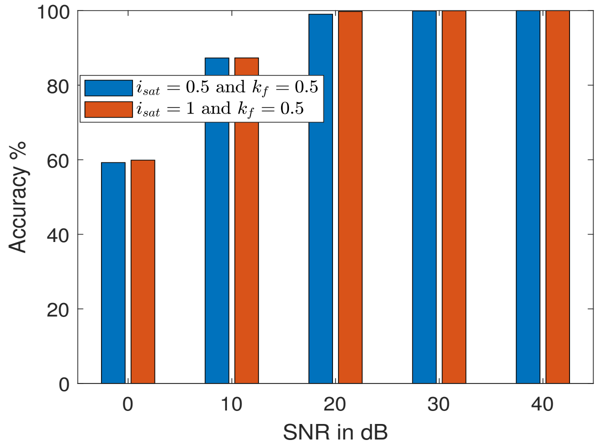

Figure 2.3: Accuracy of the proposed post-distorter for both the considered scenarios i.e. $k_f = 0.5$, and $i_{sat} = 1$, 2) $k_f = 0.5$, and $i_{sat} = 0.5$.

2.3 Message Passing detector

In this section, the message passing (MP) detection algorithm for VLC is described. The total number of non-zero elements out of N_s in each row and column of $\mathbf{H_{eff}}$ given in (2.8) are S, where $S < C_p$. Let $\mathcal{U}_b$ and $\mathcal{V}_d$ be the sets of position of non-zero values in the b^{th} row and d^{th} column of $\mathbf{H_{eff}}$, respectively such that $|\mathcal{U}_b| = |\mathcal{V}_d| = S$.

Based on (2.8), the system is modelled such that there are N_s variable nodes corresponding to $\mathbf{x}$. Similarly, corresponding to $\mathbf{y}$, there are N_s observation nodes [23–25]. In the factor graph shown in Figure 2.4, the observation node $\mathbf{x}_d$ is connected to the set of variable nodes $\{\mathbf{y}_b, b \in \mathcal{V}_d\}$. Similarly, the variable node $\mathbf{y}_b$ is connected to the set of observation nodes $\mathbf{x}_d, d \in \mathcal{U}_b\}$. The joint maximum aposteriori probability (MAP) detection rule for estimation of the transmitted information symbols from the received symbols is defined as:

$$\hat{\mathbf{x}} = \arg \max_{x \in \mathbb{A}^{N_s \times 1}} \Pr(\mathbf{x}|\mathbf{y}, \mathbf{H_{eff}}). \tag{2.23}$$

Symbol-by-symbol MAP detection rule is considered for $0 \leq d \leq N_s - 1$,

$$\begin{aligned} \hat{\mathbf{x}}_d &= \arg \max_{a_j \in \mathbb{A}} \Pr(\mathbf{x}_d = a_j|\mathbf{y}, \mathbf{H_{eff}}) \\ &= \arg \max_{a_j \in \mathbb{A}} \frac{1}{|\mathbb{A}|} \Pr(\mathbf{y}|\mathbf{x}_d = a_j, \mathbf{H_{eff}}). \end{aligned} \tag{2.24}$$

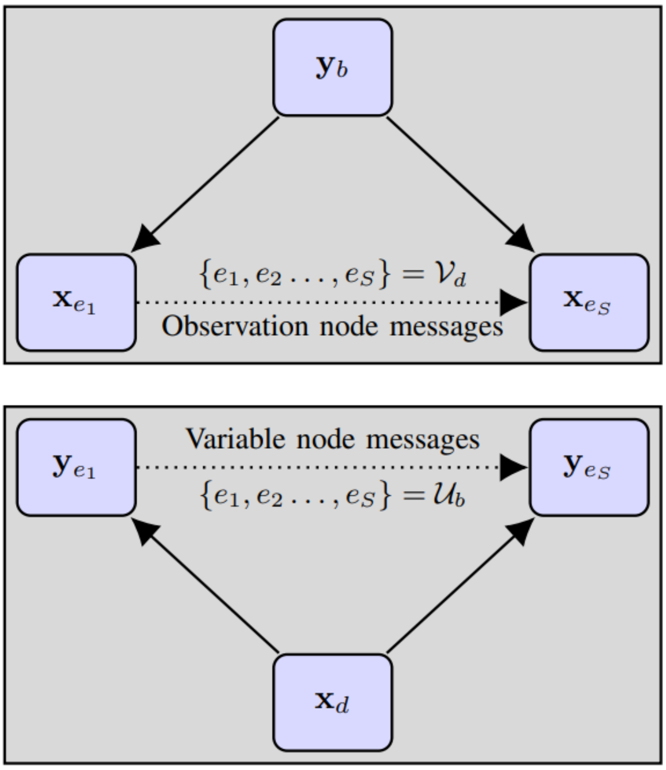

Figure 2.4: Messages in the factor graph.

Assume the probability of transmitting all the information symbols $a_j \in \mathbb{A}$ is the same. Also, $\mathbf{x}$ and $\mathbf{y}$ are independent of each other.

$$\hat{\mathbf{x}}_d \approx \arg\max_{a_j \in \mathbb{A}} \prod_{e \in \mathcal{U}_b} \Pr(\mathbf{y}_b | \mathbf{x}_d = a_j, \mathbf{H}_{\mathbf{eff}}). \tag{2.25}$$

In MP algorithm, mean and variance of the interference-plus-noise terms (ϱ_{bd}) are transmitted as messages from observation nodes $\mathbf{y}_b$ for $b \in \mathcal{V}_d$ to variable nodes $\mathbf{x}_d$ for each $d = 0, \ldots, N_s - 1$. The probability mass function of the alphabets in $\mathbb{A}$ is defined as:

$$\mathbf{p}_{db} = \{p_{db}(a_j) | a_j \in \mathbb{A}\}. \tag{2.26}$$

The steps in **Algorithm 1** are detailed below. First initialize the iteration index $i = 1$ and $\mathbf{p}^0_{db} = \frac{1}{|\mathbb{A}|}$ for $d = \{0, \ldots, N_s - 1\}$ and $d \in \mathcal{U}_b$. Then, messages are passed to the variable nodes $\mathbf{x}_d$ from the observation nodes $\mathbf{y}_b$. Thus, the message passed has a Gaussian pdf which is computed as:

Algorithm 1 MP algorithm for detection of OTFS symbols

% ***Input:***

$\mathbf{y}$ (estimated signal vector after post-distortion and OTFS demodulation) and $\mathbf{H_{eff}}$ (effective channel matrix)

% ***Initialization:***

Choose pmf $\mathbf{p}_{db}^{(0)} = \frac{1}{|\mathbb{A}|}$ for $d = \{0, \ldots, N_s - 1\}$ and $d \in \mathcal{U}_b$, i_{max}

% ***Computation:***

for $i = 1; i < i_{max}; i++$

- Compute means $(\mu_{b,d}^{(i)})$ and variances $(\sigma_{b,d}^{(i)2})$ of interference-plus-noise term $\varrho_{b,d}^{i}$ using $\mathbf{p}_{db}^{(i-1)}$ and pass them through observation nodes to variable nodes as messages.
- Variable node update $\mathbf{p}_{db}^{(i)}$ using the message received and passing it to the observation node.
- Update the decision on the information symbol transmitted.
- Increment i till maximum iteration i.e. i_{max} is reached.

end for

% ***Output:***

$\hat{\mathbf{x}}_d$ (signal vector detected).

$$\begin{aligned}
\mathbf{y}_b &= \sum_{e \in \mathcal{U}_b} \mathbf{x}_d \mathbf{H_{eff}}_{b,d} + \tilde{\mathbf{z}} \\
&= \mathbf{x}_d \mathbf{H_{eff}}_{b,d} + \sum_{e \in \mathcal{U}_b, e \neq d} \mathbf{x}_e \mathbf{H_{eff}}_{b,e} + \tilde{\mathbf{z}} \\
&= \mathbf{x}_d \mathbf{H_{eff}}_{b,d} + \varrho_{bd}
\end{aligned} \tag{2.27}$$

where ϱ_{bd} is the interference-plus-noise term and $\mathbf{H_{eff}}_{b,d}$ is the element in the b^{th} row and the d^{th} column of $\mathbf{H_{eff}}$. As the considered noise is Gaussian, ϱ_{bd} can also be approximated as a Gaussian random variable with mean and variance denoted by $\mu_{bd}^{(i)}$, and $\sigma_{bd}^{(i)2}$ respectively. The transmitted symbols are presumed to be i.i.d. and independent of noise. Variable nodes send messages to the observation nodes. The new message obtained from $\mathbf{x}_d$ to $\mathbf{y}_b$ carries the probability mass function (pmf) vector $\mathbf{p}_{db}^{(i)}$ defined as:

$$\mathbf{p}_{db}^{(i)}(a_j) = \Delta \cdot \hat{\mathbf{p}}_{db}^{(i)}(a_j) + (1 - \Delta) \cdot \mathbf{p}_{db}^{(i-1)}(a_j), \tag{2.28}$$

where $\Delta \in (0, 1]$ is defined as the damping factor.

$$\hat{p}_{db}^{(i)}(a_j) \propto \prod_{e \in \mathcal{U}_b, e \neq d} \Pr(\mathbf{y}_e | \mathbf{x}_d = a_j, \mathbf{H_{eff}}), \tag{2.29}$$

The final decision on the transmitted symbols is thus,

$$\hat{\mathbf{x}}_d = \arg\max_{a_j \in \mathbb{A}} p_d(a_j), \quad d \in \{0, \dots, N_s - 1\} \tag{2.30}$$

where,

$$p_d(a_j) = \prod_{e \in \mathcal{U}_b} (\mathbf{y}_e | \mathbf{x}_d = a_j, \mathbf{H_{eff}}). \tag{2.31}$$

Table 2.2: Simulation Parameters for OTFS-based VLC channel model.

Parameters	**Specifications**
Number of symbols transmitted per frame (N_s)	2048
Number of subcarriers (V)	1024
Knee factor (k_f) [26]	0.5
Saturation current of LED (i_{sat})[26]	0.5,1
α	1024
β	10^{-3}
Number of training pilots (N_{tr})	100

2.4 Numerical and Simulation Results

In this section, simulations are presented for validating the proposed hyperparameter-free RFF-based receiver. The simulation parameters are summarized in Table 2.2. A non-stationary channel for VLC is considered using a temporal evolution of CIRs, which is obtained by ray tracing using Zemax software [14]. To generalize the performance of the proposed post-distorter, two cases for nonlinearity are considered:

- Case-1: $i_{sat} = 1$ and $k_f = 0.5$,
- Case-2: $i_{sat} = 0.5$ and $k_f = 0.5$.

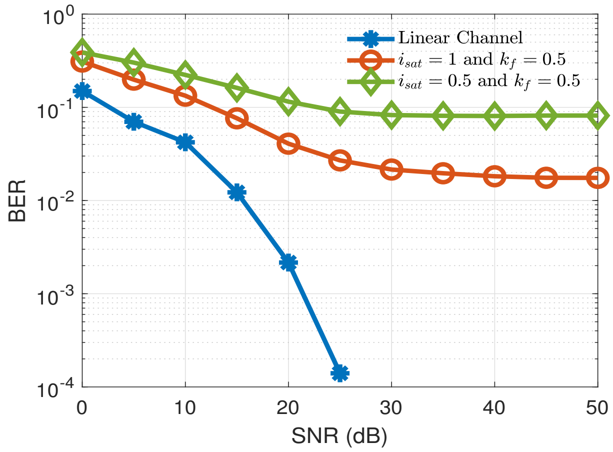

Figure 2.5: Bit error rate performance comparison for orthogonal time frequency space for linear channel and nonlinear channel for $k_f = 0.5$, and $i_{sat} = 1, 0.5$.

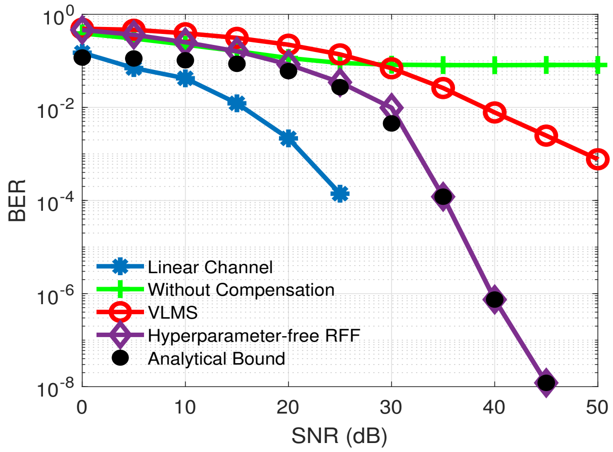

Figure 2.6: Bit error rate performance comparison for orthogonal time frequency space for the linear channel, nonlinear channel, and with hyperparameter free least square-random Fourier feature-based compensation for $k_f = 0.5$, and $i_{sat} = 1$.

The BER performance of both cases is compared with the linear channel as shown in Figure 2.5. The green curve is for the most severe case, i.e. Case-2, and the red curve is for the less severe case, i.e. Case-1. From Figure 2.5, the degradation in the BER performance of the proposed OTFS-VLC system after considering LED nonlinearity can be observed.

For the proposed detector, the results shown in Figure 2.6 indicate a considerable improvement in the BER performance compared to the compensation by VLMS and uncompensated scenario. Also, 2nd order truncated VLMS-based post-distorter gives better performance than the uncompensated scenario owing to the nonlinear approximation. Furthermore, it is observed that there is a gap between the per-

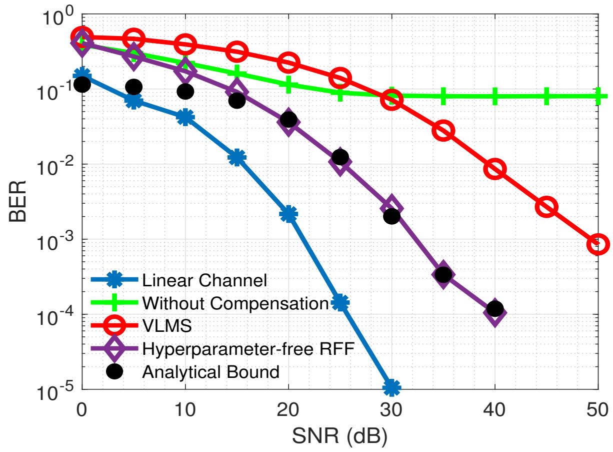

Figure 2.7: Bit error rate performance comparison for orthogonal time frequency space for the linear channel, nonlinear channel, and with hyperparameter free least square-random Fourier feature-based compensation for $k_f = 0.5$, and $i_{sat} = 0.5$.

formances of the proposed hyperparameter-free RFF-based detector and the BER performance corresponding to the linear channel. Notably, this gap is quantified in (2.20) in terms of SNR, which is further mapped via (2.22) to account for the degradation in the BER performance of the proposed receiver. These analytical results are validated in Figure 2.6 considering $k_f = 0.5$, $i_{sat} = 1$, which indicate a close overlap with the analytical results in (2.20-2.22).

In Figure 2.7, similar results are obtained for a more severe nonlinearity with $k_f = 0.5$, $i_{sat} = 0.5$, and compared to the case in Figure 2.6, interestingly, similar BER performance is achieved, which reconfirms that the proposed hyperparameter-free RFF-based receiver is best suitable for the considered VLC-OTFS system compared to VLMS-based receiver. For both cases, the performance of the proposed post-distorter is validated with the analytical results obtained. From Figure 2.6 and Figure 2.7, it is observed that the hyperparameter-free LS-RFF and analytical bound curves overlap in the high SNR regime. Also, the complexity of the proposed receiver is of the order $\mathcal{O}(n_G^2)$, which is similar to the existing low-complexity methods of post-distortion, which requires hyperparameter tuning such as RFF-KRLS [16].

2.5 Summary

In this chapter, a hyperparameter-free RFF-based receiver was proposed for OTFS to mitigate transmit side device nonlinearity. Further, analytical bounds for the performance of the proposed receiver are presented, which were validated via computer simulations over VLC channels with user-mobility. The close overlap of the analytical BER with the simulated BER verifies the analytical contributions. The results obtained establish robustness of the proposed RFF-based post-distortion for the mitigation of transmit side nonlinearity for OTFS VLC based system with user-mobility. However, the channel mapped in delay-Doppler domain is inherently sparse which is analyzed further in the next chapter.

Chapter 3

ZALMS-based sparse channel estimator in multi-carrier VLC system

In the last chapter, the inherent channel sparsity of OTFS modulated VLC systems was not exploited. In this chapter, a formal analysis of the convergence and bit-error rate of the proposed ZALMS algorithm is presented, along with supporting simulations. Effective representation of the channel in the delay-Doppler domain is inherently sparse when the number of channel paths is small compared to the number of symbols transmitted per frame [17]. Various channel estimation approaches for OTFS have been proposed in the literature. Authors in [27] have proposed time domain channel estimation and equalization method for OTFS with fractional Doppler shifts. For an RF-based communication system, authors in [28] have proposed a sparse coding-based channel estimation approach for OTFS-sparse code multiple access (SCMA) in the uplink. Taking advantage of inherent sparsity, authors in [29] have presented sparse signal recovery methods such as OMP and modified subspace pursuit (MSP) for channel estimation in uplink-OTFS. For massive-multiple input multiple output OTFS, authors in [30] have proposed a three-dimensional structured orthogonal matching pursuit (3D-SOMP) for channel estimation in the downlink with low pilot overhead. However, techniques based on greedy algorithms, like OMP and its derivatives, heavily rely on calculating the precise stopping criteria and might result in high convergence error, which reduces overall performance [31].

For static VLC systems, authors in [32] have proposed a ZALMS-based sparse channel estimation algorithm. For mobility-impaired OTFS-VLC systems, the channel estimation problem has not yet been investigated thoroughly. To estimate sparse dispersive OTFS-VLC channels and to overcome the shortcomings of the previous greedy-algorithm-based schemes, ZALMS based channel estimator is proposed with analysis in this chapter.

Recognizing the inherent sparse nature of effective channels in delay-Doppler domain, in this chapter, a ZALMS-based channel estimation method for the VLC-OTFS system is proposed. Simulations performed over a realistic mobile VLC channel modelled by RWP model indicate that OTFS with ZALMS mitigate distortions due to the user mobility and multipaths and gives better performance compared to the conventional LMS algorithm and OMP algorithm. Major contributions of this chapter are given as follows:

- OTFS for realistic indoor VLC systems to mitigate the distortion caused by multipath and user mobility is proposed.
- Recognizing the inherent sparse nature of effective VLC channel in the delay-Doppler domain, the ZALMS-based channel estimation method is proposed. The proposed algorithm gives superior performance compared to the conventional LMS and the OMP-based algorithms in terms of BER and computational complexity.
- The proposed system's BER is calculated analytically and validated using computer simulations over RWP VLC channel.
- Computational complexity of the ZALMS is compared with the conventional existing algorithms such as OMP and LMS.
- With simulations, the impact of impulsive noise on the VLC-OTFS system is shown by varying parameters.

3.1 System Model

In this section, a block diagram of the considered system model of the OTFS-VLC system affected by impairments due to user mobility, multipath between the receiver

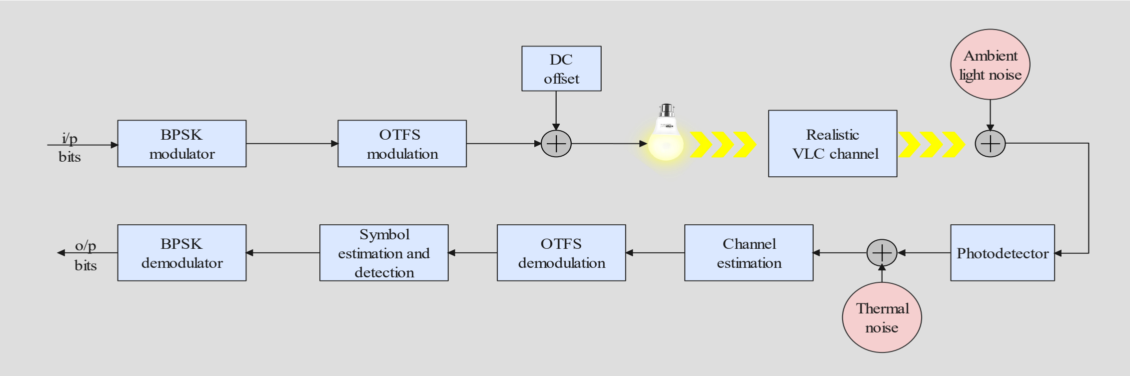

Figure 3.1: Block diagram of the considered system model.

and transmitter and ambient light noise and thermal noise is depicted in Figure 3.1. Let $N_s = KL$ represent the number of symbols transmitted in each frame, where K and L represent the number of symbols and sub-carriers, respectively. Let $\mathbf{x} \in \mathbb{C}^{N_s \times 1}$ be transmitted BPSK symbols. For OTFS modulation, Zac transformation is done on the input vector to transform delay-Doppler mapped symbols to the time domain for transmission. Zac transform is computationally complex and performed in two steps. First, the input BPSK modulated vector $\mathbf{x}$ is transformed into the time-frequency domain using the 2D ISFFT such that:

$$\mathbf{X_t}[v,u] = \sum_{l=0}^{K-1} \sum_{k=0}^{L-1} \mathbf{x}_{l,k} e^{-j2\pi(\frac{ul}{K} - \frac{vk}{L})}. \tag{3.1}$$

In the second step, Heisenberg transform on the output of ISFFT is applied to transform it into the time domain:

$$\tilde{\mathbf{x}}(t) = \sum_{u=0}^{K-1} \sum_{v=0}^{L-1} \mathbf{X_t}[v,u] e^{j2\pi u \Delta f(t-vT)} g(t - vT), \tag{3.2}$$

where $g(t)$ denotes the pulse transmitted. To create a 2D lattice in the time-frequency domain, sampling is done at intervals T and Δf, respectively, where $\Lambda = (vT, u\Delta f)$, and $v = 0, \ldots, L-1$, and $u = 0, \ldots, K-1$.

Before transmitting the time domain data, the output of Heisenberg transform $\tilde{\mathbf{x}}$ in (3.2) is prefixed with cyclic prefix of length $(C_p - 1)$, where C_p is the total number of channel paths. The symbols are broadcasted through LED in the time domain after OTFS modulation and adding cyclic prefix. The output is transmitted over a mobile VLC channel, $\mathbf{h}$, modelled by the RWP channel model. The channel is denoted by the expression $\mathbf{h} = [h_0, h_1, \ldots, h_{C_p-1}]^T$. After removing the cyclic prefix, the received information signal in the temporal domain can be expressed as:

$$\mathbf{r} = \mathbf{H}\tilde{\mathbf{x}} + \tilde{\mathbf{w}}, \tag{3.3}$$

where $\mathbf{H}$ is estimated as:

$$\mathbf{H}\left(\tau, \nu\right) = \sum_{i=1}^{C_p} h_i \delta\left(\tau - \tau_i\right) \delta\left(\nu - \nu_i\right), \tag{3.4}$$

where ν_i, τ_i are Doppler shift and delay, respectively, for the i^{th} cluster, and $\delta(\cdot)$ denotes the Dirac delta function. In this work, both ambient light noise and thermal noise are approximated by a zero mean Gaussian distribution denoted by $\tilde{\mathbf{w}} \in \mathbb{C}^{N_s \times 1}$ and is additive i.i.d. whose i^{th} entry is defined as $w_i \sim \mathcal{CN}(0, \sigma^2)$. Where $\sigma^2 = \sigma_a^2 + \sigma_t^2$ and σ_a^2 and σ_t^2 is the variance of ambient light noise and thermal noise, respectively.

Similar to the transmitter side, at the receiver side, the symbols received by photodetector $\mathbf{r}(t)$ are in the time domain and are transformed back to the information domain using the inverse Zac transformation. Similar to Zac transformation, inverse Zac transformation can be done in two following simple steps. First, the received time domain symbols are transformed to time-frequency domain $\mathbf{Y}[v, u]$ by applying the Wigner transform:

$$\mathbf{Y}[v, u] = \int \mathbf{r}(\tau) p^*(\tau - t) e^{-j2\pi f(t-\tau)} d\tau, \tag{3.5}$$

where p is the received pulse. Pulses g and p are ideal such that they satisfy bi-orthogonality and robustness. Then SFFT is applied on the output of the Wigner transform $\mathbf{Y}_{v,u}$ [17] to transform signal mapped in time-frequency to delay-Doppler, i.e. information domain.

$$\mathbf{y}_{l,k} = \frac{1}{\sqrt{KL}} \sum_{v=0}^{L-1} \sum_{u=0}^{K-1} \mathbf{Y}[v, u] e^{-j2\pi(\frac{ul}{K} - \frac{vk}{L})} + \mathbf{w}. \tag{3.6}$$

$$\mathbf{y} = \mathbf{H}^{\text{eff}} \mathbf{x} + \mathbf{w}, \tag{3.7}$$

where $\mathbf{y} \in \mathbb{C}^{N_s \times 1}$ is the symbol received at the receiver in the information domain i.e. delay-Doppler domain, $\mathbf{H}^{\text{eff}} \in \mathbb{C}^{N_s \times N_s}$ is the effective channel matrix which is sparse in nature, $\mathbf{x} \in \mathbb{C}^{N_s \times 1}$ is the transmitted BPSK symbols mapped in delay-Doppler domain and, $\mathbf{w}$ is the noise having the same statistical properties of $\tilde{\mathbf{w}}$. Alternatively, the relation in (3.7) can be written as:

$$\mathbf{y} = \mathbf{X}\mathbf{h_b} + \mathbf{w}, \tag{3.8}$$

where $\mathbf{h_b} \in \mathbb{C}^{N_L \times 1}$ is a $N_L \times 1$ vector with C_p non-zero elements and $\mathbf{X} \in \mathbb{C}^{N_s \times N_L}$. Based on the received observations ZALMS-based receiver is trained, and symbols are estimated by zero-forcing (ZF) using the channel estimated after training. The estimated symbols are then detected by maximum likelihood (ML) detector [33]. The detected symbols are then passed through a BPSK demodulator to receive the transmitted bits.

3.2 ZALMS for OTFS-VLC System

In this section, the ZALMS-based channel estimation algorithm for the OTFS-VLC system impaired by dispersive VLC channel is described as shown in **Algorithm 2**. As $C_p << KL$, effective channel matrix $\mathbf{H}^{\text{eff}}$ in (3.7) is sparse in nature. Hence, in this chapter, the ZALMS algorithm is implemented for channel estimation as it takes advantage of inherent channel sparsity [23]. The channel estimation problem can be described as a non-convex combinatorial problem that is formulated as:

$$\begin{aligned} &\min_{\mathbf{h}_b} \|\mathbf{h}_b\|_0, \\ &\text{s.t. } \|\mathbf{y}_p - \mathbf{X}_p\mathbf{h}_b\|_2^2 \leq \beta, \end{aligned} \tag{3.9}$$

where $\mathbf{y}_p$ and $\mathbf{X}_p$ are the received, and the transmitted pilots, and β is the error tolerance parameter which always has a positive value. Various offline training methods for sparse channel estimation are proposed in the literature to solve the aforementioned problem, such as OMP [34] and sparse Bayesian learning (SBL) [35] etc.. However, because these methods are offline, they have a significant propagation latency and high computational cost since they must calculate the matrix inversions for each iteration. The ZALMS algorithm is proposed to address the problem statement without having the drawbacks of offline techniques. The mean square deviation (MSD) based cost function $J_{ZA}(n)$ for ZALMS [36] is therefore defined as:

$$J_{ZA}(j) = \mathbb{E}\{\|\mathbf{y}_p(j) - \mathbf{X}_p(j)\hat{\mathbf{h}}_b(j)\|^2\} + \gamma f(\hat{\mathbf{h}}_b(j)), \tag{3.10}$$

where $\hat{\mathbf{h}}_b$ is the estimated channel, γ is the regularization parameter, and $f(\cdot)$ is the penalty term inducing sparsity. Following the use of the traditional steepest descent algorithm [37] the estimated channel $\hat{\mathbf{h}}_b(j+1)$ can be iteratively updated as:

$$\hat{\mathbf{h}}_b(j+1) = \hat{\mathbf{h}}_b(j) - \frac{\mu}{2}\nabla_{\hat{\mathbf{h}}_b(j)}(J_{ZA}(j)), \tag{3.11}$$

where the step-size parameter is denoted as μ. The gradient $\nabla_{\hat{\mathbf{h}}_b(j)}$ of the cost function considered earlier is estimated as:

$$\nabla_{\hat{\mathbf{h}}_b(j)}(J_{ZA}(j)) = 2\mathbf{R_{xx}}\hat{\mathbf{h}}_b(j) - 2\mathbf{R_{xy}} - \rho g(f(\hat{\mathbf{h}}_b(j))), \tag{3.12}$$

where $g(f(\hat{\mathbf{h}}_b(j))) = \nabla_{\hat{\mathbf{h}}_b(j)}(f(\hat{\mathbf{h}}_b(j)))$ represents the gradient of the penalty function $f(\cdot)$ which is inducing sparsity, $\rho = \frac{\gamma\mu}{2}$ denotes regularization step-size, $\mathbf{R_{xx}}$ is the auto-covariance of the transmitted pilot in delay-Doppler domain $\mathbf{X}$ computed as $\mathbb{E}\{\mathbf{X}_p^T\mathbf{X}_p\}$, and $\mathbf{R_{xy}}$ is the cross-covariance between the transmitted and received pilot vectors $\mathbf{X}_p$ and $\mathbf{y}_p$ computed as $\mathbb{E}\{\mathbf{X}_p^T\mathbf{y}_p\}$. The gradient of the cost function can be substituted to simplify the weight update equation from (3.12) to (3.11) such that:

$$\hat{\mathbf{h}}_b(j+1) = \hat{\mathbf{h}}_b(j) + \mu(\mathbf{R_{xy}} - \mathbf{R_{xx}}\hat{\mathbf{h}}_b(j)) - \rho g(f(\hat{\mathbf{h}}_b(j))). \tag{3.13}$$

Pursuing the stochastic-gradient approach, the final update expression of the estimated channel can be obtained as:

$$\hat{\mathbf{h}}_b(j+1) = \hat{\mathbf{h}}_b(j) + \mu\mathbf{X}_p^T(j)\mathbf{e}(j) - \rho g(f(\hat{\mathbf{h}}_b(j))), \tag{3.14}$$

where $\mathbf{e}(j)$ represents the instantaneous observation error estimated as:

$$\mathbf{e}(j) = \mathbf{y}_p(j) - \mathbf{X}_p(j)\hat{\mathbf{h}}_b(j), \tag{3.15}$$

Algorithm 2 ZALMS based channel estimation

Require: Received pilot signal $\mathbf{y}_p$ and transmitted pilot signal $\mathbf{X}_p$
Ensure: Maximum iteration=Max_Iter
1: $\hat{\mathbf{h}}_b \Leftarrow 0$
2: **for** j = 1:Max_Iter **do**
3: $\quad \mathbf{e}(j) \Leftarrow \mathbf{y}_p(j) - \mathbf{X}_p(j)\hat{\mathbf{h}}_b(j)$;
4: $\quad$ Update $\hat{\mathbf{h}}_b(j+1)$ using (3.14)
5: **end for**

3.2.1 ZALMS using l_1-norm approximation

The l_1-norm approximation represented as $f_1(\cdot)$, can be determined as [36],

$$f_1(\hat{\mathbf{h}}_b(j)) = \|\hat{\mathbf{h}}_b(j)\|_1 = \sum_{i=1}^{L^2} |\hat{\mathbf{h}}_b(j)(i)|. \tag{3.16}$$

The gradient term $g(f_1(\hat{\mathbf{h}}_b(j)))$ can be estimated as follows:

$$g(f_1(\hat{\mathbf{h}}_b(j))) = \mathrm{sgn}(\hat{\mathbf{h}}_b(j)). \tag{3.17}$$

where $\mathrm{sgn}(\cdot)$ is the signum function. The update equation for ZALMS-l_1-norm is given as:

$$\hat{\mathbf{h}}_b(j+1) = \hat{\mathbf{h}}_b(j) + \mu\mathbf{X}(j)\mathbf{e}(j) - \rho\,\mathrm{sgn}(\hat{\mathbf{h}}_b(j)). \tag{3.18}$$

Upon adaptation, the tap coefficients of the weight to be updated are attracted to zero by the third term present in these equations (also known as zero attractor) i.e. $\rho\mathrm{sgn}(\hat{\mathbf{h}}_b(j))$. The strength of the zero attractor is regulated by the regularization parameter which is represented as ρ. The speed of convergence of the proposed algorithm depends on the sparsity of the channel matrix.

3.3 Analytical BER Expression for VLC-OTFS System Over Mobility Impaired Channel

In this section, the BER expression of the mobility-impaired VLC-OTFS system is derived, assuming a transmitted constellation of BPSK. The average pairwise error probability (PEP) between symbol matrices given by (3.8) can be written as:

$$P(\mathbf{X}_A \to \mathbf{X}_B) = \mathbb{E}\left[Q\left(\sqrt{\frac{\gamma\,\|\mathbf{h_b}(\mathbf{X}_A - \mathbf{X}_B)\|^2}{2}}\right)\right], \tag{3.19}$$

where γ is the signal-to-noise ratio. This can be further simplified by writing:

$$\|\mathbf{h_b}(\mathbf{X}_A - \mathbf{X}_B)\|^2 = \mathbf{h_b}(\mathbf{X}_A - \mathbf{X}_B)(\mathbf{X}_A - \mathbf{X}_B)^H \mathbf{h_b}'^H. \tag{3.20}$$

The matrix $(\mathbf{X}_A - \mathbf{X}_B)(\mathbf{X}_A - \mathbf{X}_B)^H$ is Hermitian and can by diagonalized as:

$$(\mathbf{X}_A - \mathbf{X}_B)(\mathbf{X}_A - \mathbf{X}_B)^H = \mathbf{U}\boldsymbol{\Lambda}\mathbf{U}^H \tag{3.21}$$

where U is unitary and $\boldsymbol{\Lambda} = \mathrm{diag}\{\lambda_1^2, \cdots \lambda_P^2\}$, λ_i is the i_{th} singular value of difference matrix $\boldsymbol{\Delta}_{AB} = (\mathbf{X}_A - \mathbf{X}_B)$. Therefore, (3.19) can be expressed simply as:

$$P(\mathbf{X}_A \to \mathbf{X}_B) = \mathbb{E}\left[Q\sqrt{\frac{\gamma\sum_{l=1}^{L}|h_l|^2\lambda_l^2}{4}}\right]. \tag{3.22}$$

Using an approximation of Q-function:

$$Q(\sqrt{x}) \approx \frac{1}{12}e^{\frac{-x}{2}} + \frac{1}{4}e^{\frac{-2x}{3}}. \tag{3.23}$$

Therefore, (3.22) can be written as:

$$\begin{aligned} P(\mathbf{X}_A \to \mathbf{X}_B) &\approx \mathbb{E}\left[\frac{1}{12}e^{\frac{-\gamma\sum_{l=1}^{L}|h_l|^2\lambda_l^2}{8}} + \frac{1}{4}e^{\frac{-\gamma\sum_{l=1}^{L}|h_l|^2\lambda_l^2}{6}}\right] \\ &\approx \frac{1}{12}\mathbb{E}\left[e^{\frac{-\gamma\sum_{l=1}^{L}|h_l|^2\lambda_l^2}{8}}\right] + \frac{1}{4}\mathbb{E}\left[e^{\frac{-\gamma\sum_{l=1}^{L}|h_l|^2\lambda_l^2}{6}}\right]. \end{aligned} \tag{3.24}$$

$$\mathbb{E}\left[e^{\frac{-\gamma\sum_{l=1}^{L}|h_l|^2\lambda_l^2}{8}}\right] = \mathbb{E}\left[e^{\frac{-\gamma|h_1|^2\lambda_1^2}{8}} e^{\frac{-\gamma|h_2|^2\lambda_2^2}{8}} \dots e^{\frac{-\gamma|h_L|^2\lambda_L^2}{8}}\right]$$
$$= \mathbb{E}\left[e^{\frac{-\gamma|h_1|^2\lambda_1^2}{8}}\right] \mathbb{E}\left[e^{\frac{-\gamma|h_2|^2\lambda_2^2}{8}}\right] \cdot \mathbb{E}\left[e^{\frac{-\gamma|h_L|^2\lambda_L^2}{8}}\right]. \quad (3.25)$$

$$\mathbb{E}\left[e^{\frac{-\gamma|h_1|^2\lambda_1^2}{8}}\right] = \int_{h_{min}^2}^{h_{max}^2} e^{\frac{-\gamma|h_1|^2\lambda_1^2}{8}} \sum_{i=1}^{4} \frac{Q_i}{2} h^{\frac{-\beta_i}{2}} dh$$
$$= \sum_{i=1}^{4} \frac{Q_i}{2} \int_{h_{min}^2}^{h_{max}^2} e^{\frac{-\gamma|h_1|^2\lambda_1^2}{8}} h^{\frac{-\beta_i}{2}} dh \quad (3.26)$$

Let, $\frac{\gamma\lambda_1^2}{8} = a$ and $\frac{\beta_i}{2} = b$. Thus,

$$\mathbb{E}\left[e^{\frac{-\gamma|h_1|^2\lambda_1^2}{8}}\right] = \sum_{i=1}^{4} \frac{Q_i}{2} \int_{h_{min}^2}^{h_{max}^2} e^{-ah} h^{-b} dh$$
$$= \sum_{i=1}^{4} \frac{Q_i}{2} \left[-a^{b-1}\Gamma(1-b, ah)\right]_{h_{min}^2}^{h_{max}^2}$$
$$= \sum_{i=1}^{4} -a^{b-1}\frac{Q_i}{2} \left[\Gamma(1-b, ah_{max}^2) - \Gamma(1-b, ah_{min}^2)\right] \quad (3.27)$$

The upper incomplete gamma function at high signal-to-noise ratio can be approximated as:

$$\Gamma(\frac{-a_i+1}{2}, \beta_i h^2) \approx e^{-\beta_i h^2}(\beta_i h^2)^{\frac{-a_i-1}{2}}. \quad (3.28)$$

Thus, (3.27) can be approximated as:

$$\mathbb{E}\left[e^{\frac{-\gamma|h_1|^2\lambda_1^2}{8}}\right] = \sum_{i=1}^{4} -a^{b-1}\frac{Q_i}{2} \left[e^{-ah_{max}^2}(ah_{max}^2)^{-b} - e^{-ah_{min}^2}(ah_{min}^2)^{-b}\right]$$
$$= \sum_{i=1}^{4} \frac{-Q_i}{2a} \left[e^{-ah_{max}^2}(h_{max}^2)^{-b} - e^{-ah_{min}^2}(h_{min}^2)^{-b}\right]. \quad (3.29)$$

Substituting a and b in (3.29):

$$\mathbb{E}\left[e^{\frac{-\gamma|h_1|^2\lambda_1^2}{8}}\right] = \sum_{i=1}^{4} \frac{-4Q_i}{\gamma\lambda_1^2} \left[e^{\frac{-\gamma\lambda_1^2 h_{max}^2}{8}}(h_{max})^{-\beta_i} - e^{\frac{-\gamma\lambda_1^2 h_{min}^2}{8}}(h_{min})^{-\beta_i}\right]. \quad (3.30)$$

Thus, first part of (3.24) can be written as:

$$\frac{1}{12}\mathbb{E}\left[e^{\frac{-\gamma\sum_{l=1}^{L}|h_l|^2\lambda_l^2}{8}}\right] = \frac{(-1)^L}{12}\prod_{l=1}^{L}\sum_{i=1}^{4}\frac{4Q_i}{\gamma\lambda_l^2}\left[e^{\frac{-\gamma\lambda_l^2 h_{max}^2}{8}}(h_{max})^{-\beta_i} - e^{\frac{-\gamma\lambda_l^2 h_{min}^2}{8}}(h_{min})^{-\beta_i}\right]. \tag{3.31}$$

Similarly, the second part of (3.24) can be estimated as:

$$\frac{1}{4}\mathbb{E}\left[e^{\frac{-\gamma\sum_{l=1}^{L}|h_l|^2\lambda_l^2}{6}}\right] = \frac{(-1)^L}{12}\prod_{l=1}^{L}\sum_{i=1}^{4}\frac{3Q_i}{\gamma\lambda_l^2}\left[e^{\frac{-\gamma\lambda_l^2 h_{max}^2}{6}}(h_{max})^{-\beta_i} - e^{\frac{-\gamma\lambda_l^2 h_{min}^2}{6}}(h_{min})^{-\beta_i}\right]. \tag{3.32}$$

Thus, (3.19) is finally:

$$\begin{aligned} P(\mathbf{X}_A \to \mathbf{X}_B) = {} & \frac{(-1)^L}{12}\prod_{l=1}^{L}\sum_{i=1}^{4}\frac{4Q_i}{\gamma\lambda_l^2}\left[e^{\frac{-\gamma\lambda_l^2 h_{max}^2}{8}}(h_{max})^{-\alpha_i} - e^{\frac{-\gamma\lambda_l^2 h_{min}^2}{8}}(h_{min})^{-\alpha_i}\right] + \\ & \cdot \frac{(-1)^L}{4}\prod_{l=1}^{L}\sum_{i=1}^{4}\frac{3Q_i}{\gamma\lambda_l^2}\left[e^{\frac{-\gamma\lambda_l^2 h_{max}^2}{6}}(h_{max})^{-\beta_i} - e^{\frac{-\gamma\lambda_l^2 h_{min}^2}{6}}(h_{min})^{-\beta_i}\right]. \end{aligned} \tag{3.33}$$

The PEP with a minimum value of L dominates the overall BER. Thus, on assuming L=1.

$$\begin{aligned} P(\mathbf{X}_A \to \mathbf{X}_B) = {} & \frac{-1}{12}\sum_{i=1}^{4}\frac{4Q_i}{\gamma\lambda_1^2}\left[e^{\frac{-\gamma\lambda_1^2 h_{max}^2}{8}}(h_{max})^{-\beta_i} - e^{\frac{-\gamma\lambda_1^2 h_{min}^2}{8}}(h_{min})^{-\beta_i}\right] \\ & - \frac{1}{4}\sum_{i=1}^{4}\frac{3Q_i}{\gamma\lambda_1^2}\left[e^{\frac{-\gamma\lambda_1^2 h_{max}^2}{6}}(h_{max})^{-\beta_i} - e^{\frac{-\gamma\lambda_1^2 h_{min}^2}{6}}(h_{min})^{-\beta_i}\right]. \end{aligned} \tag{3.34}$$

Finally,

$$\begin{aligned} P(\mathbf{X}_A \to \mathbf{X}_B) = {} & \sum_{i=1}^{4}\frac{-Q_i}{3\gamma\lambda_1^2}\left[e^{\frac{-\gamma\lambda_1^2 h_{max}^2}{8}}(h_{max})^{-\beta_i} - e^{\frac{-\gamma\lambda_1^2 h_{min}^2}{8}}(h_{min})^{-\beta_i}\right] \\ & - \frac{3Q_i}{4\gamma\lambda_1^2}\left[e^{\frac{-\gamma\lambda_1^2 h_{max}^2}{6}}(h_{max})^{-\beta_i} - e^{\frac{-\gamma\lambda_1^2 h_{min}^2}{6}}(h_{min})^{-\beta_i}\right]. \end{aligned} \tag{3.35}$$

The exact expression for the PEP using the characteristic function of the RWP channel model is given by (3.33). Using the PEP expression, an upper bound on the BER is obtained given by (3.35). From the simulation results, the analytical results are verified, and it is observed that the BER bound is tight at high SNRs.

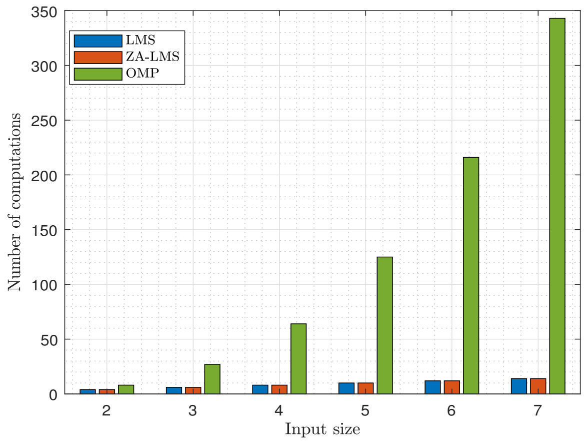

Figure 3.2: Computational complexity of orthogonal matching pursuit and zero attracting least mean square for orthogonal time frequency space-visible light communication system.

3.4 Computational Complexity Analysis

The computational complexity of the channel estimation in each iteration for both LMS and ZALMS-l_1 is in the order of $\mathcal{O}(2N_t)$, while for the OMP is $\mathcal{O}(N_t^3)$, which is significantly higher in comparison to the proposed scheme. From Figure 3.2, it can be observed that the rate of increase in the number of computations with input data size is more in OMP as compared to the traditional LMS and proposed ZALMS algorithm for the VLC-OTFS system.

Table 3.1: Simulation Parameters for ZALMS-aided OTFS VLC systems.

Parameters	**Specifications**
Number of symbols transmitted per frame (N_s)	512
Number of subcarriers (V)	256
Step-size (μ)	0.005
Regularization parameter (γ)	5×10^{-8}

3.5 Numerical and Simulation Results

In this section, the simulation results to illustrate the enhanced performance of the ZALMS-based channel estimator are demonstrated over the classical LMS-based channel estimator and OMP-based channel estimator for the dispersive OTFS-VLC system, with channel modelled by RWP model. The system parameters for simula-

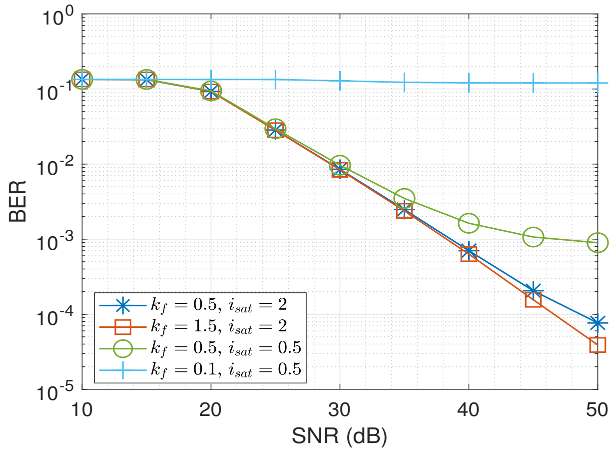

Figure 3.3: Effect of light emitting diode nonlinearity on bit error rate vs signal-to-noise ratio performance of zero attracting least mean square for orthogonal time frequency space-visible light communication system.

tions are listed in **Table 3.1**. We have considered $N_s = 512$ for simulations. The BPSK modulation scheme is used to modulate symbols mapped in delay-Doppler domain. For channel-estimation, step-size (μ) is considered to be 0.005, regularization parameter (γ) for ZALMS is 5×10^{-8}. After OTFS demodulation at the receiver, the ZALMS-based channel estimation algorithm is applied to estimate the CIR from the pilot symbols. Results are compared with the LMS and OMP estimator.

The BER performance of the proposed ZALMS algorithm in the epresence of LED nonlinearity is shown in Figure 3.3. Four different cases of nonlinearity are considered by varying values of knee factor (k_f) and saturation current (i_{sat}). As the value of knee factor or saturation current is decreased the severity of nonlinearity increases. From Figure 3.3, the degradation in the BER performance of the proposed OTFS-VLC system after considering LED non-linearity can be observed.

In Figure 3.4, the convergence performance of ZALMS, OMP, and LMS estimators is compared for signal-to-noise ratio of 50 dB. The convergence plot of ZALMS falls below both the OMP and the LMS on saturation, i.e. ZALMS has lower mean square deviation than OMP and LMS upon saturation. Thus, it can be inferred that for sparse OTFS- VLC systems ZALMS is a better alternative to the OMP and traditional LMS method.

Figure 3.5 presents the BER performance of OMP, LMS and ZALMS. OTFS with ZALMS and LMS-based channel estimator gives considerable gain compared to OMP-based receiver. While ZALMS gives a gain of approximately 4 dB at BER of

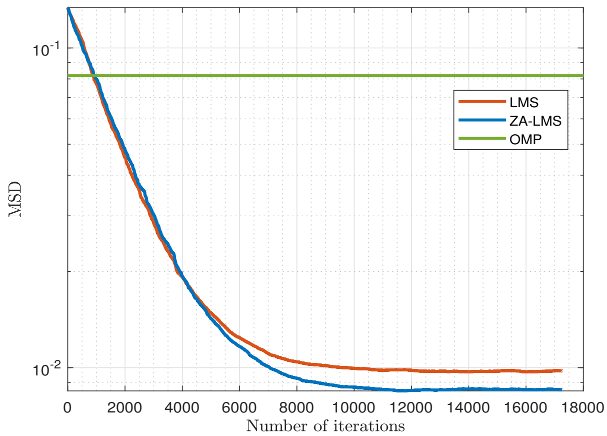

Figure 3.4: Mean square deviation performance for orthogonal time frequency space-visible light communication system at signal-to-noise ratio 30 dB

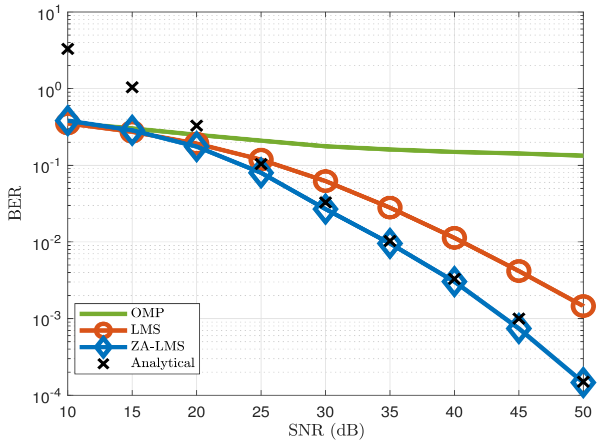

Figure 3.5: Bit error rate performance for orthogonal time frequency space-visible light communication system

10^{-3}. Thus, it can be concluded that the proposed ZALMS-based channel estimator is a better estimator as compared to the conventional techniques for exploiting the inherent sparsity of the OTFS-VLC system.

3.6 Summary

In this chapter, ZALMS-based channel estimator is proposed for a VLC-OTFS system with the dispersive mobile multipath channel. Furthermore, it was observed from the simulations that due to the sparse nature of the VLC channel represented in the delay-Doppler domain, ZALMS performed better than the traditional LMS and OMP algorithm. The simulated findings show that ZALMS is a more suitable low-complexity solution for channel estimation in the OTFS-VLC system. In this chapter and in chapter 2, the distortion effects resulting from user mobility and LED nonlinearity are addressed, with a primary focus on improving BER performance. However, VLC systems often face obstacles leading to LoS blockage, as visible light cannot pass through obstacles due to its high penetration loss causing low sum rate owing to significant signal loss which is explored in the next chapter.

Chapter 4

Rate Maximization for RIS-Assisted Indoor VLC Systems

In the previous chapters, the distortion effects resulting from user mobility and LED nonlinearity were discussed, with a primary focus on improving BER performance. However, transmission in visible light suffers from severe performance degradation due to LoS blockage, as visible light can not pass through obstacles due to its high penetration loss [13, 38]. Moreover, the illumination requirements of LEDs pose a challenge to the practical deployment of VLC [39]. In this context, ORIS and using LEDs as relays have been proposed in the literature [11, 40]. In addition to this, there are other benefits of using ORIS instead of LEDs as relays, such as low power consumption, reduced complexity, easy deployment, and low interference. RIS has recently been introduced in the literature as a solution to mitigate the impact of LoS blockages, broaden the coverage area, and enhance the achievable user rate [11, 41].

ORIS is a promising technology that facilitates NLoS paths to enhance the performance of optical wireless communication systems [42]. The mirror array (MA)-based RIS and the metasurface array (MSA)-based RIS are the two most popular reflecting surface designs employed for ORIS in VLC systems [11] where in MA, the received power gain is always positive. In [43], for the rate maximization problem, a low-complexity iterative solution based on the sine-cosine algorithm is proposed to determine the optimal orientation of the RIS MA. However, the study has only considered a single-user scenario. In [44], a low-complexity algorithm is proposed to maximize the achievable sum rate. In [45], authors have proposed RIS and angle diversity-assisted receivers for indoor VLC systems to improve average SNR performance. Recently, deep Q-learning-based solutions have been investigated to improve the performance of wireless networks [46, 47]. However, since deep learning methods have huge time and space complexity overhead and are more suited for unstructured problems, a function-approximate learning solution with much lower computational overhead for the (structured) phase control problem of the VLC system is proposed. The integration of function approximation into Q-learning has been inspired by the classical works in reinforcement learning (RL). Function approximation is a widely utilized technique in Q learning. Notably, the author in [48] laid the foundational groundwork for Q-learning, which is introduced as a model-free, off-policy RL method. While the original Q-learning algorithm was tabular, the concept of function approximation has since been integrated to handle high-dimensional state spaces. Additionally, the application of function approximation in Q-learning can be traced back to the work in [49]. This marked a significant step towards utilizing function approximation, particularly neural networks, to generalize Q-values across states, enabling more efficient learning in complex environments. Further contributions by authors in [50–52] provide comprehensive insights into the fundamentals of Q-learning and its extensions. Thus, in this letter, a Q-learning framework is proposed for a multi-user, multi-LED, ORIS-assisted VLC system that is one of the RL paradigms as the future machine learning paradigm. The main components of Q-learning are agent, environment, state, action, and reward. After convergence, the agent discovers the optimal policy, a rule of actions that maximizes the reward. In the proposed scheme, Q-learning defines an environment to maximize a sum rate-defined reward. The contributions of this chapter can be listed as follows:

- A Q-learning framework in an ORIS-assisted multi-user VLC system is presented. The proposed ORIS array is divided into subarrays, whose number equals the number of active LEDs or active users. Each subarray is controlled jointly by roll and yaw angles.

- A function approximation is proposed to reduce conventional Q-learning's search and update requirements. The update equation is then obtained using the gradient descent approach. The proposed scheme has less storage and computation needs. The number of trainable parameters is independent of the

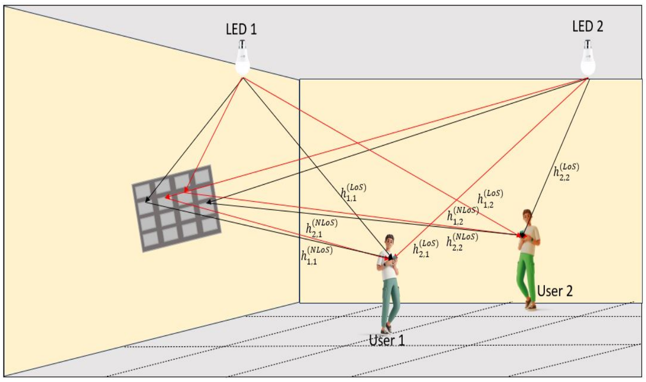

Figure 4.1: Multi-user optical reflecting intelligent surface-aided indoor visible light communication system model.

state size and action spaces.

- Simulations are performed in a standard indoor environment, considering practical constraints. Specifically, a 3D grid is considered for multi-user locations, and their movements follow the Markov process. ORIS effectively improves the sum rates, and function-approximated learning provides similar performance as conventional Q-learning with lower computation resources.

4.1 System Model

A realistic indoor optical ORIS-assisted VLC system is considered, as shown in Figure 4.1. There are N low-cost passive reflecting elements in the MA-based optical ORIS deployed on a wall. Two rotational degrees of freedom given by the yaw angle (γ) and roll angle (ω) can be used to adjust the orientation of each array element. Let $\mathbf{s} = [s_1, s_2, \ldots, s_L]^T \in \mathbb{R}^{L\times 1}$ be the transmitted symbols on L LEDs. Corresponding to U users, the ORIS is divided into U equal parts, with yaw and roll angle of each group of ORIS optimized to cater for the respective user so as to maximize the sum rate. The ORIS is divided into equal parts such that fairness among the users is maintained while maximizing the sum rate. For simplicity, an indoor scenario with two LEDs ($L = 2$) and two users ($U = 2$) where LED 1 is intended for User 1 and LED 2 is intended for User 2 is considered, as shown in Figure 4.1. The symbols are transmitted through the LEDs after adding a DC bias to bring the LEDs into the forward-biased operating region [53]. The resulting signal is sent over a practical VLC channel composed of LoS and NLoS components. Subsequently, at the receiver, the transmitted signals are received by the PD at the u^{th} user:

$$y_u = y_u^{(LoS)} + y_u^{(NLoS)} + z_u, \tag{4.1}$$

where $y_u^{(LoS)}$ and $y_u^{(NLoS)}$ are the symbols received by the LoS and NLoS paths, respectively, and z_u is the AWGN with zero mean and σ^2 variance, i.e., $z_u \sim \mathcal{N}(0, \sigma^2)$ where $u = 1, \cdots, U$.

4.1.1 LoS Channel Gain

The LoS channel gain from the l^{th} LED to the u^{th} user within the field-of-view (FoV) of PD ($0 \leq \xi_{l,u} \leq \xi_{\text{FoV}}$) follows the Lambertian model as

$$h_{l,u}^{(LoS)} = \frac{(L_m + 1)\, A_{\text{PD}} \cos^{L_m}(\phi)\, T\,(\xi_{l,u})\, G_o\,(\xi)\, G_i\,(\xi) \cos(\xi)}{2\pi d_{l,u}^2}, \tag{4.2}$$

where L_m represents the Lambertian index computed as:

$$L_m = \left(\log_2 {}^{1}\!/_{\cos(\theta_{1/2})}\right)^{-1}, \tag{4.3}$$

where $\theta_{1/2}$ denotes the angle of half-intensity radiation. In (4.2), the physical surface area of the PD is represented as A_{PD}, ϕ is the angle of irradiance, ξ is the angle of incidence, $d_{l,u}$ denotes the distance between the LED and the user, $G_o(\xi)$ is the gain of the optical filter and $G_i(\xi)$ denotes the gain of the non-imaging concentrator within the FoV. The gain of the non-imaging concentrator can be computed as:

$$G_i(\xi) = \frac{r_f^2}{\sin^2 \xi_{\text{FoV}}}, \tag{4.4}$$

where $\xi \in [0, \xi_{\text{FoV}}]$ and the refractive index of the concentrator is denoted as r_f. It can be noted that the angle of irradiance (ϕ) is not affected by the orientation of the user's device, whereas the incidence angle (ξ) is highly influenced by the device's orientation. The cosine of the angle of incidence ξ can be represented in terms of the device's elevation angle (α) and the azimuth angle (β) as:

$$\cos(\xi_{l,u}) = \left(\frac{x_l - x_u}{d_{l,u}}\right)\cos(\beta)\sin(\alpha) + \left(\frac{y_l - y_u}{d_{l,u}}\right)\sin(\beta)\sin(\alpha) + \left(\frac{z_l - z_u}{d_{l,u}}\right)\cos(\alpha), \tag{4.5}$$

where $(x_l, y_l, z_l), l = 1, \ldots, L$ are the position vectors specifying the locations of the LEDs on the roof of the room and (x_u, y_u, z_u) are the position vectors specifying the locations of the users. For modelling the elevation angle, the Laplace distribution with the mean and the standard deviation of 41^{o} and 9^{o} is used, respectively. The range of the elevation angle is typically considered to be $[0, \frac{\pi}{2}]$. The azimuth angle follows a uniform distribution $\beta \sim \mathcal{U}[-\pi, \pi]$. The received signal from the LoS path can be obtained as the signals received from all LEDs as:

$$y_u^{(LoS)} = \sum_{l=1}^{L} \rho h_{l,u}^{(LoS)} P s_l. \tag{4.6}$$

where ρ is the responsivity of the PD; and P is the emission power of the LED.

4.1.2 NLoS Channel Gain

The NLoS channel consists of two components: 1) First, the wall/ORIS is the receiver of the light emitted by the LED, and 2) the wall/ORIS acts as a point source that re-emits the light to the user. The reflective surface, i.e. wall/ORIS, is equally divided into K squared surfaces. Each k^{th} surface is considered to have an area of dA_k. Further, it is assumed that the incident ray from the LED is reflected exactly from the centre of the reflective surfaces. For the NLoS channel, the following two cases are considered:

Case I (No-ORIS VLC channel)

In the case of a VLC channel without ORIS, the light is reflected by the k^{th} segment of the wall surface to the u^{th} user. The corresponding NLoS channel can be written for the FoV $(0 \leq \xi_{u,k} \leq \xi_{\text{FoV}})$ as:

$$h_{l,k,u}^{(NLoS)} = \chi_{\text{wall}} \frac{(m+1)A_{\text{PD}}}{2\pi^2 d_{l,k}^2 d_{u,k}^2} dA_k \cos^m(\phi_{l,k}) \cos(\xi_{l,k}) \cos(\phi_{u,k}) \cos(\xi_{u,k}) \, T(\xi_{l,k}) \, G(\xi_{u,k}), \tag{4.7}$$

where χ_{wall} denotes the reflection coefficient of the wall surface; $d_{l,k}$ and $d_{u,k}$ are the distances between the l^{th} LED and the k^{th} wall segment, and the k^{th} wall segment and the user, respectively; $\phi_{l,k}$ and $\phi_{u,k}$ are the angles of irradiance from the LED to the wall segment and from the wall towards the user, respectively; $\xi_{l,k}$ and $\xi_{u,k}$ are the angles of incidence on the wall and the user, respectively.

Case II (ORIS-assisted VLC channel)

Similarly, for an optical ORIS-aided VLC channel, the channel gain of the reflected signal from the k^{th} mirror array is obtained for the FoV $(0 \leq \xi_{u,k} \leq \xi_{\text{FoV}})$ as:

$$h_{l,k,u}^{(NLoS)}\left(\gamma_l, \omega_l\right) = \chi_{\text{RIS}} \frac{(m+1)A_{\text{PD}}}{2\pi^2 d_{l,k}^2 d_{u,k}^2} dA_k \cos^m(\phi_{l,k}) \cos\left(\xi_{l,k}\right) \cos\left(\phi_{u,k}\right) \cos\left(\xi_{u,k}\right) T\left(\xi_{l,k}\right) G\left(\xi_{u,k}\right), \tag{4.8}$$

where χ_{RIS} is the reflection coefficient of the ORIS element. In addition to the reflection coefficient, the channel gain above is different from that of Case I in the sense that the cosine of the angle of irradiance is specified by the yaw and roll angles of the MA and can be computed as:

$$\cos\left(\phi_{u,k}\right) = \frac{(x_k - x_u)}{d_{u,k}} \cos\left(\omega\right) \sin\left(\gamma\right) + \frac{(y_k - y_u)}{d_{u,k}} \cos\left(\omega\right) \cos\left(\gamma\right) + \frac{(z_k - z_u)}{d_{u,k}} \sin\left(\omega\right), \tag{4.9}$$

where (x_k, y_k, z_k) represents the coordinates of the k^{th} element of the ORIS. The received signal from the NLoS path can be given as:

$$y_u^{(NLoS)} = \rho \sum_{l=1}^{L} \sum_{k=1}^{N} h_{l,k,u}^{(NLoS)} P s_l. \tag{4.10}$$

Based on the received signals via LoS and NLoS paths, the sum rate across users can be computed as:

$$R = \frac{W}{2} \sum_{u=1}^{L} \log_2 \left(1 + \frac{e}{2\pi} \delta_u\right), \tag{4.11}$$

where e is the value of the base of natural logarithms. The modulation bandwidth is denoted as W. The signal-to-interference-plus noise ratio (SINR) of u_{th} user is

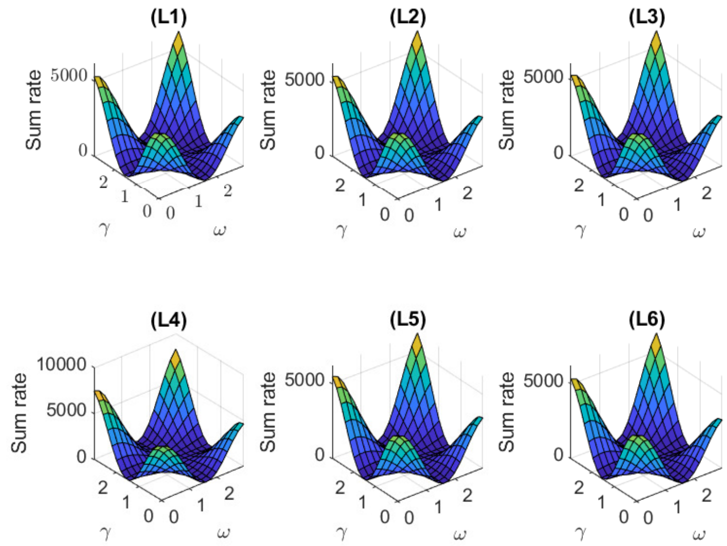

Figure 4.2: Impact of roll and yaw angle on sum rate at different user locations of User 2.

represented as δ_u and can be obtained as:

$$\delta_u = \frac{\rho^2 P^2 \left| h_{l,u}^{(LoS)} + \sum_{k=1}^{N} h_{l,k,u}^{(NLoS)} \right|_{l=u}^{2}}{\sigma^2 + \rho^2 P^2 \left| \sum \left(h_{l,u}^{(LoS)} + \sum_{k=1}^{N} h_{l,k,u}^{(NLoS)} \right) \right|_{l\neq u}^{2}}. \tag{4.12}$$

The objective is to maximize the rate by jointly optimizing the ORIS yaw and roll angles for all users. The impact of roll and yaw angle on the sum rate is shown in Figure 4.2. It can be observed that the sum rate is maximum at a fixed roll and yaw angle.

Towards this, Q-learning is employed, where the problem is translated to the maximization problem of the long-term average discounted sum rate described in the following section.

4.2 Proposed Q-learning framework

In this section, the conventional and the proposed Q-learning approaches are presented. First, the rate maximization problem can be formulated in terms of Q-learning framework by defining the states, actions, and rewards as follows. Subsequently, the proposed approach is presented.

4.2.1 State space

It can be noted that the variations in the VLC channel are assumed to follow a Markov process, since different channels are estimated at different user positions. For this framework, a state of the system is defined in terms of user location as:

$$s = (x_u, y_u, z_u, \forall u) \in \mathcal{S} \subset \mathbb{R}^3, \tag{4.13}$$

where $\mathcal{S}$ is a finite set specifying the grid locations in an indoor environment. Regarding state transitions, it can be noted that a user can move to its neighbour grid, not to other places in the grid state space, which makes these states a part of the Markov chain. It can be noted that VLC channel gain depends on the user's location. Therefore, the variations in the channel can also be modelled as a Markov process.

4.2.2 Action space

In the present system model, actions are to select the roll and yaw angles of the mirror elements. Since there are L LEDs, the mirror elements of the ORIS array are grouped into L groups corresponding to each LED. Each group will be set with the same yaw and roll angle values. Thus, there are $2L$ variables need to be obtained for action selection, that is, $\gamma_l, \omega_l \in \left[-\frac{\pi}{2}, \frac{\pi}{2}\right], l = 1, \ldots, L$. For finite angles resolutions, the values of these angles are selected from an angle codebook $\mathcal{C} = \left\{\tilde{\theta}_1, \ldots, \tilde{\theta}_{|\mathcal{C}|} : \tilde{\theta}_i \in \left[-\frac{\pi}{2}, \frac{\pi}{2}\right]\right\}$. For simplicity, a uniform codebook is chosen, e.g., for b-bit codebook, $\mathcal{C} = \left\{-\frac{\pi}{2}, -\frac{\pi}{2} + \Delta, -\frac{\pi}{2} + 2\Delta, \ldots\right\}$, where $\Delta = \frac{\pi}{2^b}$. With yaw and roll angles combined, the action space can be represented with $2Lb$ bits codebook as:

$$a = (\gamma_l, \omega_l, \forall l = 1, \ldots, L) \in \mathcal{C}^{2L}. \tag{4.14}$$

4.2.3 Reward function

The objective of the Q-learning is to maximize the long-term discounted rates as:

$$\begin{aligned} &\max_{\gamma_l(t),\omega_l(t),\forall l} \sum_{i=t}^{\infty} \overline{\gamma}^{i-t} R(\gamma_l(t),\omega_l(t)) \\ &\text{s.t. } \gamma_l(t),\omega_l(t) \in \left[-\frac{\pi}{2},\frac{\pi}{2}\right], \forall l, \end{aligned} \tag{4.15}$$

where the notation of (t) is introduced to show the time-slot dependent operations. Thus, the reward function can be written in terms of the rate as:

$$r(s,a) = R(\gamma_l,\omega_l,\forall l). \tag{4.16}$$

4.2.4 Conventional Q-learning

Algorithm 3 Coventional Q-learning algorithms.

Require: Initial state s_0 randomly and $Q_0(s,a) = 0, \forall s,a$
  for $t = 1,2,\ldots$ **do**
    ORIS configuration: take ϵ-greedy action a_{t+1}

$$a_{t+1} = \begin{cases} \arg\max_a Q_t(s_t,a) & \text{w.p. } 1-\epsilon_t \\ \text{random } a & \text{w.p. } \epsilon_t \end{cases}$$

    Obtain reward r_t and get users' next position s_{t+1}
    Update Q-function using (4.21)
  end for

In this section, the conventional Q-learning algorithm given in **Algorithm 3** is explained. Q-learning is a trial-and-error algorithm, where, based on the observations, actions are taken in order to find better actions in a sequential manner by computing Q-function. The Q-function, also known as the state-action value function, evaluates the pair of a state and an action. Using Bellman's equation, the relation for optimum Q-value can be written as:

$$Q^*(s,a) = r(s,a) + \overline{\gamma}\mathbb{E}\max_b Q^*(s_1,b), \tag{4.17}$$

where s_1 is the next state obtained after taking action a in the state s; and $\overline{\gamma}$ is the discount factor. Given the optimum Q-values, one can take an optimal action for a given state as:

$$a_{t+1}^{*} = \arg\max_{a} Q^{*}(s_t, a), \tag{4.18}$$

which yields the optimum policy $\pi^* : \mathcal{S} \rightarrow \mathcal{C}$. However, since optimum Q-values are not known, the square of the difference of both sides, i.e. Δ_t^2, is minimized by using the gradient descent method, where Δ_t is the temporal difference. Thus, providing the Q-update equation as:

$$Q_{t+1}(s_t, a_{t+1}) = Q_t(s_t, a_{t+1}) + \beta_t \Delta_t, \tag{4.19}$$

where β_t is the step-size. The temporal difference is calculated as:

$$\Delta_t = \left[r_t + \overline{\gamma} \max_{b} Q_t(s_{t+1}, b) \right] - Q_t(s_t, a_{t+1}), \tag{4.20}$$

with $r_t = r(s_t, a_{t+1})$ being the instantaneous reward. However, since the optimal Q-values are not available, they are obtained iteratively using the update equation in the stochastic gradient descent as:

$$Q_t(s_t, a_{t+1}) = (1 - \beta_t)\, Q_{t-1}(s_t, a_{t+1}) + \beta_t \left[r_t + \gamma \max_{b} Q_{t-1}(s_{t+1}, b) \right]. \tag{4.21}$$

In gradient descent method, if the function $F(\mathbf{x})$ is defined and differentiable in a neighborhood of a point $\mathbf{x}_n$, then it follows that:

$$\mathbf{x}_{n+1} = \mathbf{x}_n - \beta \nabla F(\mathbf{x}_n). \tag{4.22}$$

In conventional Q-learning, $F \coloneqq \frac{1}{2}\Delta^2$ and $\mathbf{x} \coloneqq Q$, thus giving:

$$\begin{aligned}
Q_t &= Q_{t-1} - \beta \nabla_Q \left[\frac{1}{2} \Delta_{t-1}^2 \right] \\
&= Q_{t-1} - \beta \Delta_{t-1} \nabla_Q \Delta_{t-1} \\
&= Q_{t-1} + \beta \Delta_{t-1} \\
&= Q_{t-1} + \beta \left[r_{t-1} + \gamma \max_{b} Q(s_t, b) \right] - \beta Q_{t-1}(s_{t-1}, a_t) \\
&= (1 - \beta) Q_{t-1}(s_{t-1}, a_t) + \beta \left[r_{t-1} + \gamma \max_{b} Q(s_t, b) \right]
\end{aligned} \tag{4.23}$$

where,

$$\nabla_{Q(s,a)}\Delta = \nabla_Q \left[r_t + \gamma \max_b Q(s', b) \right] - \nabla_Q Q(s,a) \tag{4.24}$$

$$= \nabla_Q \left[\gamma \max_b Q(s', b) \right] - 1 \tag{4.25}$$

$$= -1 \tag{4.26}$$

Now, when Q-learning is replaced by the linear function approximation (LFA) as:

$$Q_\theta(s_t, a_{t+1}) \approx \mathbf{u}^T(s_t, a_{t+1})\boldsymbol{\theta}, \tag{4.27}$$

then the differentiation will be done with respect to $\boldsymbol{\theta}$. That is, the updated equation of gradient descent is:

$$\begin{aligned}\boldsymbol{\theta}_t &= \boldsymbol{\theta}_{t-1} - \beta \frac{\partial}{\partial \boldsymbol{\theta}} \left[\frac{1}{2} \Delta_{t-1}^2 \right] \\ &= \boldsymbol{\theta}_{t-1} - \beta \Delta_{t-1} \frac{\partial}{\partial \boldsymbol{\theta}} \left[\Delta_{t-1} \right] \\ &= \boldsymbol{\theta}_{t-1} - \beta \Delta_{t-1} \frac{\partial Q}{\partial \boldsymbol{\theta}} \cdot \frac{\partial}{\partial Q} \left[\Delta_{t-1} \right] \\ &= \boldsymbol{\theta}_{t-1} + \beta \Delta_{t-1} \mathbf{u}(s_{t-1}, a_t) \end{aligned} \tag{4.28}$$

where $\frac{\partial}{\partial Q}\left[\Delta_{t-1}\right] = -1$ and $\frac{\partial Q(s,a)}{\partial \boldsymbol{\theta}} = \mathbf{u}(s,a)$. Steps of the iterative update algorithm are presented in the **Algorithm 3**, where after initialization of the state of users, a ϵ-greedy random action is performed. The action leads to rewards, and the next state, which is used to update the Q-values. These steps are run until episodes are completed. In each episode, the exploration and the step-update factors are updated. From the literature [54], it can be seen that for finite sets, the Q-learning algorithm converges if step size and exploration are chosen appropriately. The decay parameter ζ as $\beta_t = \beta_{t-1}(1-\zeta)$ and $\epsilon_t = \epsilon_{t-1}(1-\zeta)$.

4.2.5 Function approximated Q-learning

In this section, the proposed function approximated Q-learning algorithm is explained as given in **Algorithm 4**. Despite the simplicity of the updates in the conventional Q-learning, it has limited practical utility when applied to real-world

Algorithm 4 Approximated Q-learning algorithms.

Require: Initial state s_0 randomly and $Q_0(s,a)=0, \forall s, a$

for $t = 1, 2, \ldots$ **do**

ORIS configuration: take ϵ-greedy action a_{t+1}

$$a_{t+1} = \begin{cases} \arg\max_{a} Q_t(s_t, a) & \text{w.p. } 1-\epsilon_t \\ \text{random } a & \text{w.p. } \epsilon_t \end{cases}$$

Obtain reward r_t and get users' next position s_{t+1}

Update $\theta_{k,l}$ using (4.32) and compute Q-function approximation.

end for

systems. Specifically, the size of Q-matrix is of the order $|\mathcal{S}| \times |\mathcal{C}|^{2L}$, which grows prohibitively with the number of LEDs, rendering convergence of the table entries unacceptably slow. In addition, action selection in $\max\limits_{a} Q(s,a)$ requires an extensive exhaustive search of the feasible action set.

A popular method for making Q-learning applicable in real-world settings is through function approximation [55, 56]. The approximation in our set-up is inspired by the fractional form of the rate expression. Specifically, $Q(s_t, a_t)$ is approximated to $\hat{Q}(s_t, a_t)$ as:

$$\hat{Q}(s_t, a_t) = \frac{W}{2}\sum_{u=1}^{L}\log_2\left(1 + \frac{e}{2\pi}\frac{\rho^2 P^2 \left| h_{l,u}^{(LoS)}\theta_{0,l} + \sum_{k=1}^{N}\theta_{k,l}h_{l,k,u}^{(NLoS)}\right|_{l=u}^2}{\sigma^2 + \rho^2 P^2 \left|\sum\left(h_{l,u}^{(LoS)}\theta_{0,l} + \sum_{k=1}^{N}\theta_{k,l}h_{l,k,u}^{(NLoS)}\right)\right|_{l\neq u}^2}\right). \tag{4.29}$$

where $\theta_{k,l}, k = 1, \ldots, N, l = 1, \ldots, L$ are the coefficients introduced for the approximation. Here, N and L are the number of mirrors in the mirror array and the number of LEDs, respectively. In function approximation, a function that maximizes the reward function is used. Intuitively, in every iteration, the action taken by the next policy at a given state is obtained by selecting the action that yields the best action value (in our case, maximizes the sum rate). Thus, function approximation in our setup is inspired by the sum rate across users, as is given in (4.12).

Function approximation reduces the original task in conventional Q-learning algorithm of learning nearly $|\mathcal{S}| \cdot |\mathcal{C}|^{2L}$ parameters to learn $(L+1)L$ parameters. In practical scenarios, which will generally have a very large size of states and actions, this reduction has a significant computational improvement as only $(L+1)L$

parameters are to be learned to maximize the sum rates. The error in function approximation for approximate Q-learning can be given by the temporal difference equation. The parameters can be updated by minimizing the squared temporal difference using the gradient descent method as:

$$\theta_{k,l}(t) = \theta_{k,l}(t-1) - \frac{\alpha_{k,l}}{2} \nabla_{k,l} \Delta_t^2(s_t, a_t, \theta_{k,l}), \forall k, l \tag{4.30}$$

Regarding the non-linear function approximation (NLFA) of the Q-values:

$$\nabla_{k,l} = \frac{\partial \hat{Q}}{\partial \theta_{k,l}} = \frac{\partial \frac{W}{2} \sum_{u=1}^{L} \log_2 \left(1 + \frac{e}{2\pi} \frac{\rho^2 P^2 \left| h_{l,u}^{(LoS)} \theta_{0,l} + \sum_{k=1}^{N} \theta_{k,l} h_{l,k,u}^{(NLoS)} \right|_{l=u}^2}{\sigma^2 + \rho^2 P^2 \left| \sum \left(h_{l,u}^{(LoS)} \theta_{0,l} + \sum_{k=1}^{N} \theta_{k,l} h_{l,k,u}^{(NLoS)} \right) \right|_{l \neq u}^2} \right)}{\partial \theta_{k,l}} \tag{4.31}$$

For User 1, the (4.31) can be simplified as:

$$\nabla_{k,1} = \frac{\partial \frac{W}{2} \log_2 \left(1 + \frac{e}{2\pi} \frac{\rho^2 P^2 \left| h_{1,1}^{(LoS)} \theta_{0,1} + \sum_{k=1}^{N} \theta_{k,1} h_{1,k,1}^{(NLoS)} \right|^2}{\sigma^2 + \rho^2 P^2 \left| \sum \left(h_{2,1}^{(LoS)} \theta_{0,2} + \sum_{k=1}^{N} \theta_{k,2} h_{2,k,1}^{(NLoS)} \right) \right|^2} \right)}{\partial \theta_{k,1}} \tag{4.32}$$

$$\nabla_{k,1} = \frac{W e \rho^2 P^2 |h_{1,1}^{(LoS)} \theta_{0,1} + \sum_{k=1}^{N} \theta_{k,1} h_{1,k,1}^{(NLoS)}|}{\left\{ \begin{array}{l} e\rho^2 P^2 |h_{1,1}^{(LoS)} \theta_{0,1} + \sum_{k=1}^{N} \theta_{k,1} h_{1,k,1}^{(NLoS)}|^2 \\ \quad + 2\pi \left(\sigma^2 + \rho^2 P^2 \left| \sum \left(h_{2,1}^{(LoS)} \theta_{0,2} + \sum_{k=1}^{N} \theta_{k,2} h_{2,k,1}^{(NLoS)} \right) \right|^2 \right) \end{array} \right\}} \tag{4.33}$$

Similarly for User 2,

$$\nabla_{k,2} = \frac{W e \rho^2 P^2 |h_{2,2}^{(LoS)} \theta_{0,2} + \sum_{k=1}^{N} \theta_{k,2} h_{2,k,2}^{(NLoS)}|}{\left\{ \begin{array}{l} e\rho^2 P^2 |h_{2,2}^{(LoS)} \theta_{0,2} + \sum_{k=1}^{N} \theta_{k,2} h_{2,k,2}^{(NLoS)}|^2 \\ \quad + 2\pi \left(\sigma^2 + \rho^2 P^2 \left| \sum \left(h_{1,2}^{(LoS)} \theta_{0,1} + \sum_{k=1}^{N} \theta_{k,1} h_{1,k,2}^{(NLoS)} \right) \right|^2 \right) \end{array} \right\}} \tag{4.34}$$

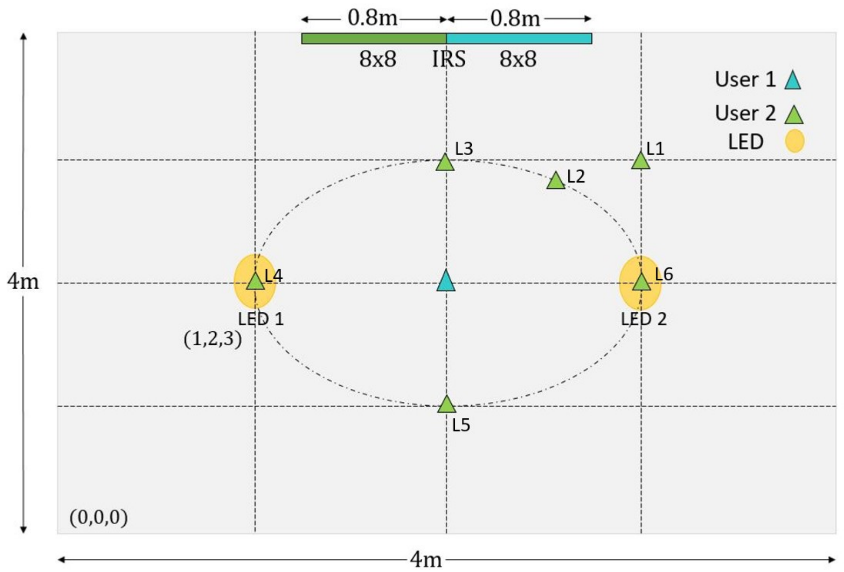

Figure 4.3: Locations of light emitting diode, optical intelligent reflecting surface and users.

4.3 Computational Complexity

In this section, the computational complexity of the proposed function approximated Q-learning algorithm is compared with the exhaustive search method and conventional Q-learning algorithm. In order to compare the proposed function approximated Q-learning, it is assumed that one Q-value is approximated per step of an episode. Using an exhaustive search method, both roll and yaw angles were searched in the range $[0, \pi]$ with a step size of $\pi/16$. Thus, the number of computations required in an exhaustive search method for one user position is $128 \times 16 \times 16$. As the dimension of ORIS increases with an increase in the number of users, the search space also increases dramatically. Since Q-values depend on θ-values, after updation of θ-values, one can compute more Q-values to fill the Q-matrix faster, that is, to converge in lower iterations and subsequently get better rewards in earlier episodes. In terms of complexity, conventional Q-learning requires to learn Q-matrix of size nearly $|\mathcal{S}| \cdot |\mathcal{C}|^{2L}$ to learn $(L+1)L$ parameters. While for function approximated Q-learning, only $(L+1)L$ parameters are to be learnt to maximize the sum rates.

4.4 Numerical and Simulation Results

In an indoor environment, without loss of generality, an environment is considered with two LEDs of 5 W and two users, one fixed at the centre of the area and one moving in a circular path. The mobile user (User 2) is considered to be moving on a circular trajectory to provide dynamic conditions while the static user (User 1) is considered to be standing at a random location. In Figure 4.3, LED 1 and LED 2 are represented by yellow circles placed on the roof at axis positions (1,2,3) and (3,2,3), respectively. User 1 is fixed at the centre of the room (2,2,0.75), while User 2 is moving on a circular trajectory. The trajectory of User 2 is considered such that it enters the room and then moves on a circular trajectory. **L1** is the point on trajectory when User 2 enters the room thus **L1** lies outside the circular trajectory, then User 2 moves on circular trajectory following **L2** $\rightarrow$ **L3** $\rightarrow$ **L4** $\rightarrow$ **L5** $\rightarrow$ **L6**. The locations considered on the circular trajectory are (L1:3,3,0.75), (L2:2,3,0.75), (L3:3,2,0.75), (L4:1,2,0.75), (L5:2,1,0.75), and (L6:2.5,2.87,0.75). Two LEDs are optimally placed so as to completely illuminate the room of dimension 4m $\times$ 4m $\times$ 3m as shown in Figure 4.3. With respect to the position of LEDs, the ORIS is placed on the centre of a wall so as to have the minimum distance from both LEDs to reduce the loss between the LED and the ORIS. The modulation bandwidth is considered to be 200 MHz. The reflection coefficients of the ORIS element and the wall are 0.95 and 0.8, respectively. The PD's responsivity with FoV 85° is 0.53 A/W. The half-intensity radiation angle of the LED is 70°. The PD's area is 1cm^2. The refractive index of the concentrator is 1.5, and the optical fibre gain is 1. Yaw and roll angles are computed for one ORIS array having 128 elements since one user location is fixed. Simulations assuming perfect instantaneous channel state information of the composite channel (LED-ORIS-user) for Q-learning are run for 6000 episodes, where each episode has 2000 steps. Other Q-learning parameters are as follows: $\overline{\gamma} = 0.7$, $\zeta = 0.001$, $\epsilon_0 = 1$, $\beta_0 = 0.8$.

Figure 4.4 compares the cases of ORIS and no-ORIS for conventional Q-learning and function approximated Q-learning framework at SNR=30 dB. First, it can be seen that the average reward increases and converges for both Q-learning and the proposed function approximated Q-learning method. In the case of no-ORIS, the

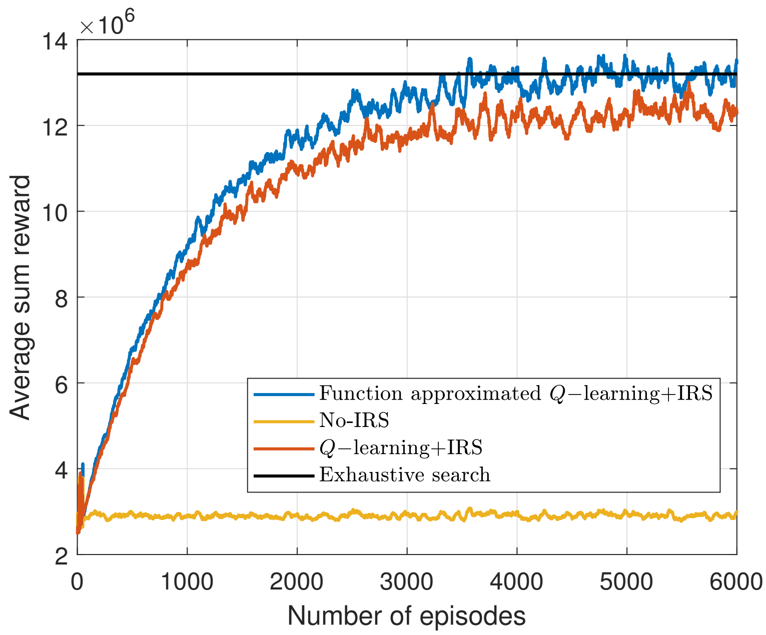

Figure 4.4: Performance comparison and convergence of Q-learning and function approximated Q-learning.

average rewards (sum rates) are much lower and almost similar for different user positions across episodes. After convergence of the roll and yaw angle selection policy, the achievable rates of Q-learning are approximately 4.5 times of the without ORIS, which is due to the number of ORIS elements, creating multi-path diversity. It can be observed that the proposed algorithm gives the best result as it coincides with the exhaustive search method after convergence.

Figure 4.5 shows the performance of the proposed function-approximate Q-leaning framework considering different SNR values to depict the sensitivity of the SNR on the sum rate, i.e., the average sum reward. As can also be seen from (4.12), when the SNR value decreases, the sum rate also decreases. The same is also observed in our simulation results. On increasing the SNR from 10 dB to 30 dB, the gain of around 10^2 times is observed, while on increasing SNR from 30 dB to 60 dB, the gain observed is around 10^3 times.

4.5 Summary

In this chapter, optimum ORIS (roll and yaw) angles for multi-user VLC systems using the RL framework are obtained. Two approaches are presented, of which the proposed function approximation method achieves the same performance with

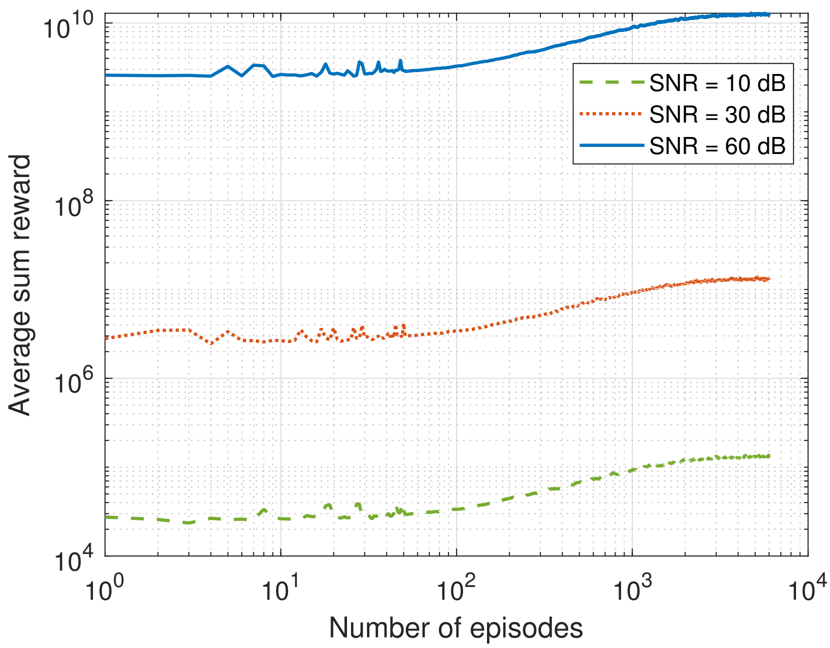

Figure 4.5: Performance of function approximated Q-learning with different signal-to-noise ratio values.

lower computational complexity. In the simulation-based 3D grid world, a subarray of ORIS elements is learned to align according to the multi-user positions. The proposed approach has significantly less overhead and is independent of the sizes of state and action spaces. In this chapter, the performance of ORIS is analyzed for VLC systems. To further provide 360^0 coverage, the performance of an OSTAR-RIS is analyzed in the next chapter.

Chapter 5

CSK Modulation and Symbol Detection in OSTAR-RIS-aided VLC Systems

In the previous chapter, the performance of a ORIS is analyzed for VLC systems. To further provide 360^0 coverage in this chapter, we analyze the performance of an OSTAR-RIS aided VLC system based on a CSK modulation scheme. However, most studies relied on OOK modulation in VLC systems. CSK-based VLC systems offer several advantages over conventional modulation schemes like OOK and pulse-amplitude modulation (PAM). These advantages include maintaining a constant combined intensity of the RGB bands to prevent flickering, reducing intensity fluctuations perceived by the human eye, minimizing inrush currents when used with large LED arrays, and achieving higher data rates [57]. The performance of CSK has been analyzed in the case with AWGN [58], where a mathematical expression for the BER was provided. Additionally, [59] introduced a four-color CSK format that is utilized in the IEEE 802.15.7 standard. In addition, LEDs introduce distortions due to their nonlinear characteristics, resulting in poor channel estimation. Traditional methods like LS and minimum mean square error (MMSE) have been used for channel estimation and symbol detection in linear wireless systems. The traditional schemes, including LS, MMSE, and LMS, explicitly estimate the CSI before detecting the transmitted symbols. In contrast, DNN models can be trained under various channel conditions to predict transmitted data, allowing for direct recovery

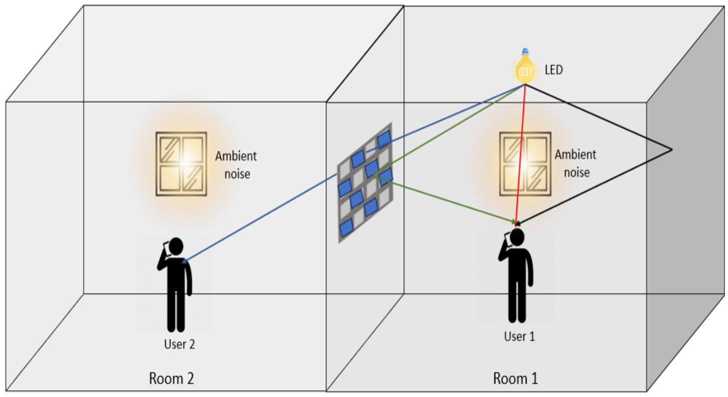

Figure 5.1: OSTAR-RIS-aided indoor VLC system model.

of transmitted symbols without explicitly estimating CSI [60]. Our contributions in this chapter are listed as follows:

- An OSTAR-RIS-based indoor VLC system model impaired by LoS blockage, ambient noise, and LED nonlinearity is proposed.
- A DNN-based symbol detector is proposed for direct symbol detection without explicit channel estimation.
- For performance analysis, the expressions of BER is derived. The data rate and BER performance of OOK, 3-CSK and 4-CSK are compared and analyzed.

5.1 System Model

We consider a practical indoor OSTAR-RIS-assisted VLC system, as depicted in Figure 5.1, where there are N-low-cost elements on the OSTAR-RIS mounted on a wall between Room 1 and Room 2. The LED is in the centre of the ceiling of Room 1 and serves users in the two rooms simultaneously. Due to room design requirements, Room 1 with LED serves as a workspace and Room 2 without any light fixtures serves as a relaxation or sleeping area. The mirror elements on the OSTAR-RIS act as reflector elements, while the liquid crystal (LC)-based elements act as refractor elements to serve User 2. The symbol set of M-CSK modulation is denoted by $A = \{\mathbf{x}_1, \mathbf{x}_2, \ldots, \mathbf{x}_M\}$ where $\mathbf{x}_i = (I_R, I_G, I_B)$ is a vector and I_R, I_G, and I_B represent the emitted power from forward-biased RGB LED, respectively whose nonlinear characteristics distorts the input symbols. This nonlinear behaviour can be characterized by AM/AM modelling and can be described using Rapp's model:

$$\mathbf{s} = f(\mathbf{x}) = \frac{\mathbf{x}}{(1 + (\frac{\mathbf{x}}{\mathrm{i_{sat}}})^{2\mathrm{k_f}})^{\frac{1}{2\mathrm{k_f}}}}, \tag{5.1}$$

where $\mathrm{i_{sat}}$ and $\mathrm{k_f}$ are the saturation current and knee factor of the LED, respectively. The knee factor regulates the transitional smoothness of LED features from the linear to the saturation region. The resulting signal is sent over a VLC channel, which comprises of LoS and NLoS components. The effective channel h_j between the LED and users where $(j = 1, 2)$, corresponding to User 1 and User 2, respectively, can be estimated as:

$$h_j = \begin{cases} h_j^{\mathrm{LoS}} + h_j^{\mathrm{MA}} + h_j^{\mathrm{Wall}}, j = 1, \\ h_j^{\mathrm{LC}}, j = 2, \end{cases} \tag{5.2}$$

where h^{LoS} is the LoS path between the LED and the User 1, h^{MA} and h^{Wall} are the NLoS reflected channels of the User 1 reflected from the MA elements of OSTAR-RIS and the wall, respectively. Similarly, h^{LC} is the channel gain of User 2, refracted from the LC element of the OSTAR-RIS. The channel coefficients h^{LoS}, h^{MA}, h^{LC} and h^{Wall} can be calculated as in [1]. Subsequently, at the receiver, the transmitted signals are received by the photodetector, which yields the following output:

$$\mathbf{y}_j = \rho h_j \mathbf{s} + \mathbf{z}_j, \tag{5.3}$$

where the received symbol by the j^{th} user $\mathbf{y}_j = (y_R, y_G, y_B)$ is composed of elements which represent the electric currents of the photodetectors with RGB optical filters, and ρ is the responsivity of the photodetector. A zero-mean Gaussian distribution is used in this study to simulate ambient light noise denoted by $\mathbf{z} = (z_R, z_G, z_B)$ is additive i.i.d. with variance σ^2. The symbols received by the PD are then passed through a DNN for direct symbol detection without explicit channel estimation. Before deploying the DNN online, the weights for the neurons are optimized, and the optimal weights are obtained on a training set.

5.1.1 LoS Channel Gain

The LoS channel between the LED and the j^{th} user in Room 1 follows the Lambertian model within the FoV $0 \leq \xi \leq \xi_{\text{FoV}}$ as

$$h_j^{\text{LoS}} = \iota \left(\frac{(L+1)\, A_{\text{PD}} \cos^{L}(\phi)\, G_o(\xi)\, G_i(\xi) \cos(\xi)}{2\pi d_j^2} \right), \tag{5.4}$$

where $\iota \in 0, 1$ a parameter to indicate whether the LoS path is present or blocked by possible blockers, L represents the Lambertian index and can be computed as

$$L = \left(\log_2 \frac{1}{\cos(\theta_{1/2})} \right)^{-1}, \tag{5.5}$$

$\theta_{1/2}$ represents the angle of half-intensity radiation. The physical surface area of the photodetector is denoted by A_{PD}, ϕ and ξ are the angles of irradiance and incidence, respectively, d_j is the distance between the LED and the j^{th} user, $G_o(\xi)$ and $G_i(\xi)$ denotes the gain of the optical filter and the non-imaging concentrator, i.e. $G_i(\xi)$ is defined as

$$G_i(\xi) = \frac{{\text{r}_\text{f}}^2}{\sin^2 \xi_{\text{FoV}}}, \tag{5.6}$$

The refractive index of the concentrator is denoted by r_f. The cosine of ξ can be expressed as a function of the azimuth angle (α_a) and the elevation angle (α_e) of the device:

$$\cos(\xi) = \left(\frac{x_l - x_j}{d_{l,j}} \right) \sin(\alpha_e) \cos(\alpha_a) + \left(\frac{y_l - y_j}{d_{l,j}} \right) \sin(\alpha_e) \sin(\alpha_a) + \left(\frac{z_l - z_j}{d_{l,j}} \right) \cos(\alpha_e), \tag{5.7}$$

The position vectors specifying the location of the LED is denoted by (x_l, y_l, z_l) and the position vectors specifying the location of the j^{th} user is denoted by (x_j, y_j, z_j). $d_{l,j}$ is the distance between the LED and the j^{th} user. For modelling the elevation angle, the Laplace distribution with the mean being 41° and the variance being 9°. The range of the elevation angle is typically considered to be $[0, \frac{\pi}{2}]$. The uniform distribution $\alpha_a \sim \mathcal{U}[-\pi, \pi]$ is considered for the azimuth angle.

In Room 1, the NLoS channel of the j^{th} user after reflection from the wall is computed as

$$h_j^{\mathrm{Wall}} = \chi_{\mathrm{wall}} \frac{(L+1)A_{\mathrm{PD}}}{2\pi^2 d_{l,k}^2 d_{j,k}^2} dA \cos^L(\phi_{l,k}) \cos(\xi_{l,k}) \cos(\phi_{j,k}) \cos(\xi_{j,k}) G_o(\xi_{l,k}) G_i(\xi_{j,k}), \tag{5.8}$$

where χ_{wall} is the reflection coefficient of the wall surface, and dA represents the area of the wall segment. The LED-to-k^{th} wall segment distance is denoted by $d_{l,k}$, and the distance between the k^{th} wall segment and the j^{th} user is denoted by $d_{j,k}$. The angles of irradiance from the LED to the wall segment and from the wall segment towards the j^{th} user are $\phi_{l,k}$ and $\phi_{j,k}$, respectively. The angles of incidence on the wall and on the j^{th} user are $\xi_{l,k}$ and $\xi_{j,k}$, respectively. Similarly, the NLoS channel of users in Room 1 after reflection from the OSTAR-RIS is computed as

$$h_j^{\mathrm{MA}} = \chi_{\mathrm{RIS}} \frac{(L+1)A_{\mathrm{PD}}}{2\pi^2 d_{l,i}^2 d_{j,i}^2} dA \cos^L(\phi_{l,i}) \cos(\xi_{l,i}) \cos(\phi_{j,i}) \cos(\xi_{j,i}) G_o(\xi_{l,i}) G_i(\xi_{j,i}), \tag{5.9}$$

where the reflection coefficient of the MA in OSTAR-RIS is denoted by the χ_{RIS}. The distance between the LED and the i^{th} OSTAR-RIS segment is denoted by $d_{l,i}$, while $d_{j,i}$ is the distance between i^{th} MA and the j^{th} user. The angles of irradiance from the LED to the MA and the MA to the j^{th} user are denoted by $\phi_{l,i}$ and $\phi_{j,i}$, respectively. The angle of incidence on the MA and the j^{th} user are $\xi_{l,i}$ and $\xi_{j,i}$, respectively. The cosine of the angle of irradiance is represented in the form of the yaw (γ_{MA}) and roll (ω_{MA}) angles of the MA elements of the OSTAR-RIS array and can be computed as

$$\cos(\phi_{j,i}) = \frac{(x_i - x_j)}{d_{j,i}} \sin(\gamma_{MA}) \cos(\omega_{MA}) + \frac{(y_i - y_j)}{d_{j,i}} \cos(\gamma_{MA}) \cos(\omega_{MA}) + \frac{(z_i - z_j)}{d_{j,i}} \sin(\omega_{MA}), \tag{5.10}$$

where (x_i, y_i, z_i) represents the coordinates of the i^{th} element of the OSTAR-RIS.

Similarly, for users in Room 2, the effective channel is given by

$$h_j^{\mathrm{LC}} = \begin{cases} \psi_{\mathrm{LC}} \frac{(L+1)A_D}{2\pi^2 \left(d_{l,i}\right)^2 \left(d_{j,i}\right)^2} dA G_o\left(\xi_{l,i}\right) G_i\left(\xi_{l,i}\right) \cos^L\left(\phi_{l,i}\right) \\ \times \cos\left(\xi_{l,i}\right) \cos\left(\phi_{j,i}\right) \cos\left(\xi_{j,i}\right), 0 \leq \xi_{j,i} \leq \xi_{\mathrm{FoV}}, \\ 0, \qquad \xi_{j,i} > \xi_{\mathrm{FoV}}, \end{cases} \tag{5.11}$$

where

$$\cos\left(\phi_{j,i}\right) = \left(\frac{x_i - x_j}{d_{j,i}}\right) \sin\left(\gamma_{LC}\right) \cos\left(\omega_{LC}\right) + \left(\frac{y_i - y_j}{d_{j,i}}\right) \cos\left(\gamma_{LC}\right) \cos\left(\omega_{LC}\right) + \left(\frac{z_i - z_j}{d_{j,i}}\right) \sin\left(\omega_{LC}\right), \tag{5.12}$$

where yaw (γ_{LC}) and roll (ω_{LC}) are the angles of the LC elements of the OSTAR-RIS array. The transition coefficient, ψ_{LC}, can be given by

$$\psi_{\mathrm{LC}} = T_{\mathrm{an}}\left(\xi_{j,i}\right) \times T_{\mathrm{na}}\left(\theta\right), \tag{5.13}$$

where the angular transmittances as the signal enters and exits the LC cell are denoted by $T_{\mathrm{an}}\left(\xi_{j,i}\right)$ and $T_{\mathrm{na}}\left(\theta\right)$, respectively. They can be respectively expressed in terms of the angular reflectance as $T_{\mathrm{an}}\left(\xi_{j,i}\right) = 1 - R_{\mathrm{an}}\left(\xi_{j,i}\right)$ and $T_{\mathrm{na}}\left(\theta\right) = 1 - R_{\mathrm{na}}\left(\theta\right)$. The angular reflectance can be derived as

$$R_{\mathrm{an}}\left(\xi_{j,i}\right) = \frac{1}{2}\left(\frac{\eta^2 \cos\left(\xi_{j,i}\right) - \sqrt{\eta^2 - \sin^2\left(\xi_{j,i}\right)}}{\eta^2 \cos\left(\xi_{j,i}\right) + \sqrt{\eta^2 - \sin^2\left(\xi_{j,i}\right)}}\right)^2 + \frac{1}{2}\left(\frac{\cos\left(\xi_{j,i}\right) - \sqrt{\eta^2 - \sin^2\left(\xi_{j,i}\right)}}{\cos\left(\xi_{j,i}\right) + \sqrt{\eta^2 - \sin^2\left(\xi_{j,i}\right)}}\right)^2, \tag{5.14}$$

$$R_{\mathrm{na}}\left(\theta\right) = \frac{1}{2}\left(\frac{\cos\left(\theta\right) - \sqrt{\eta_r^2 - \sin^2\left(\theta\right)}}{\cos\left(\theta\right) + \sqrt{\eta_r^2 - \sin^2\left(\theta\right)}}\right)^2 + \frac{1}{2}\left(\frac{\eta_r^2 \cos\left(\theta\right) - \sqrt{\eta_r^2 - \sin^2\left(\theta\right)}}{\eta_r^2 \cos\left(\theta\right) + \sqrt{\eta_r^2 - \sin^2\left(\theta\right)}}\right)^2, \tag{5.15}$$

where η_c and η_a represent the refractive indices of the LC cell and air, respectively, and $\eta = {}^{\eta_c}/_{\eta_a}$ and $\eta_r = {}^{\eta_a}/_{\eta_c}$ denotes the relative refractive indices. The range of η_c varies from 1.5 to 1.7 and needs to be tuned because ψ_{LC} can be optimized by tuning η_c. In the OSTAR-RIS light amplification for the emerging signal can be achieved by the LC elements via stimulated emission. Beer's absorption law can be used to determine the output signal power P_{out} following the amplification of light signal in the presence of an external electric field when an optical signal with power P_{in} refracts from an LC cell with the transition coefficient ψ_{LC}:

$$P_{\text{out}} = P_{\text{in}} \times \ \exp\left(A_{GC} D\right) \times \psi_{\text{LC}}, \tag{5.16}$$

where the amplification gain coefficient denoted by A_{GC} is given by

$$A_{GC} = \frac{2\pi\eta_c^3}{\cos\left(\xi_{\hat{u}}^n\right)\lambda} E_o E, \tag{5.17}$$

The LC cell's depth is indicated by D, and the exponential rise in incident signal power is shown by the expression $\exp(A_{GC}D)$. In (5.16), λ is the wavelength of the optical signal, E_o is the electro-optic coefficient, and E (in V/m) is the external electric field. The external electric field E can be calculated as $E = {}^{V_E}/_{D}$, where V_E is

$$V_{\text{E}} = V_{\text{TH}} - \log\left(-\tan\left[\frac{\tan^{-1}\left(\frac{\eta_o\sqrt{(\eta_e^2-\eta_o^2)(\eta_e^2-\eta_c^2)}}{\eta_c(\eta_e^2-\eta_o^2)}\right)}{2} - \frac{\pi}{4}\right]\right). \tag{5.18}$$

where η_e and η_o denote the extraordinary and ordinary refractive indices of the LC based element's in OSTAR-RIS, respectively.

5.2 Modulation Schemes

This section introduces CSK modulation for ORIS-aided VLC systems, where Figure 5.2 illustrates the constellation diagrams for different modulation techniques: OOK, 3-CSK, and 4-CSK. In OOK, LED switching is controlled by turning it "ON" or "OFF" based on bit streams, with high and low amplitude pulses representing logical '1' and '0', respectively, as shown in Figure 5.2(a). The OOK constellation features two symbols corresponding to two LED intensity levels. The color bands used in CSK modulation are specified in IEEE 802.15.7 VLC standard, where each symbol is associated with a specific color combination. This chapter introduces two CSK modulation schemes, 3-CSK and 4-CSK, depicted in Figure 5.2(b) and Figure 5.2(c),

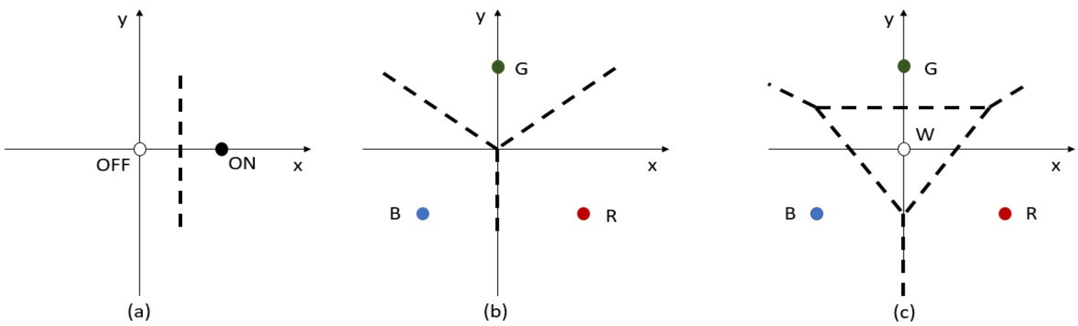

Figure 5.2: Constellation diagram and decision region of modulated techniques: (a) OOK, (b) 3-CSK, and (c) 4-CSK.

respectively.

5.2.1 CSK Modulation

In this subsection, the 3-CSK and 4-CSK modulation schemes are discussed for RIS-aided indoor VLC systems. In the 3-CSK modulation, three peripheral symbols are utilized, as presented in the constellation diagram in Figure 5.2(b). Let coordinates $\bar{\mathbf{x}} = (x_x, x_y)$, $\bar{\mathbf{z}} = (z_x, z_y)$ and $\bar{\mathbf{y}} = (y_x, y_y)$ denote the 2D coordinates of the projected points on plane $I_R + I_G + I_B = P_T$ from $\mathbf{x} = (x_R, x_G, x_B)$, $\mathbf{z} = (z_R, z_G, z_B)$, $\mathbf{y} = (y_R, y_G, y_B)$, respectively. The 2D coordinates $\bar{\mathbf{x}} = (x_x, x_y)$, $\bar{\mathbf{z}} = (z_x, z_y)$, and $\bar{\mathbf{y}} = (y_x, y_y)$ could be calculated as

$$\bar{\mathbf{x}} = \mathbf{T}\mathbf{x} \tag{5.19}$$

$$\bar{\mathbf{z}} = \mathbf{T}\mathbf{z} \tag{5.20}$$

$$\bar{\mathbf{y}} = \mathbf{T}\mathbf{y} \tag{5.21}$$

where the geometric transformation matrix $\mathbf{T}$ from the 3D coordinate system to the 2D coordinate system is given by

$$\mathbf{T} = \begin{bmatrix} -\frac{1}{\sqrt{2}} & \frac{1}{\sqrt{2}} & 0 \\ -\frac{1}{\sqrt{6}} & -\frac{1}{\sqrt{6}} & \frac{2}{\sqrt{6}} \end{bmatrix} \tag{5.22}$$

Likewise, the equivalent 2D symbol set is presented by $\bar{A} = \{\bar{\mathbf{x}_1}, \bar{\mathbf{x}_2}, \ldots, \bar{\mathbf{x}_M}\}$. As shown in Figure 5.2(c), in 4-CSK, three of the symbols denoted by R, G, and B are located at the centers of the RGB color bands on the xy color coordinates, while the fourth symbol, W, is chosen such that its distance is the maximum from the other three symbols. The constellation diagram for 4-CSK is shown in Figure 5.2(c). In 4-CSK, the symbols are positioned within an equilateral triangle on the plane, as defined by the transformation in (5.22).

5.2.2 Constraints on CSK signals

In this subsection, the constraints on CSK signals due to the illumination requirements of VLC systems are outlined as:

1. Optical power emitted from LEDs is always positive, thus the elements in the signal vector $\mathbf{x}$ satisfy the following constraint:

$$I_R \geq 0, \quad I_G \geq 0, \quad I_B \geq 0, \tag{5.23}$$

2. The total optical power P_T of the RGB LEDs is assumed to be a constant in every symbol duration to avoid flickering, such that:

$$I_R + I_G + I_B = P_T \tag{5.24}$$

Based on these constraints the generated CSK symbols are transmitted through LED with nonlinear characteristics.

5.3 DNN-based symbol detection

In this section, we propose a DNN-based model for direct symbol detection without explicit channel estimation. The model designed for offline training comprises of 5-layers with, 1-input layer and 1-output layer, and remaining 3 layers in between are hidden layers as shown in Figure 5.3. The number of neurons in each layers are 512, 700, 400, 120, 16, respectively. Every 16 bits of the data transmitted through LEDs are grouped together and predicted simultaneously based on a single model trained independently at SNR 40 dB. These bits are then concatenated for the final output. For activation, the rectified linear activation function (ReLU) defined as $f(a) = \max(0, a)$ is used after each hidden layer, where a is the input to the

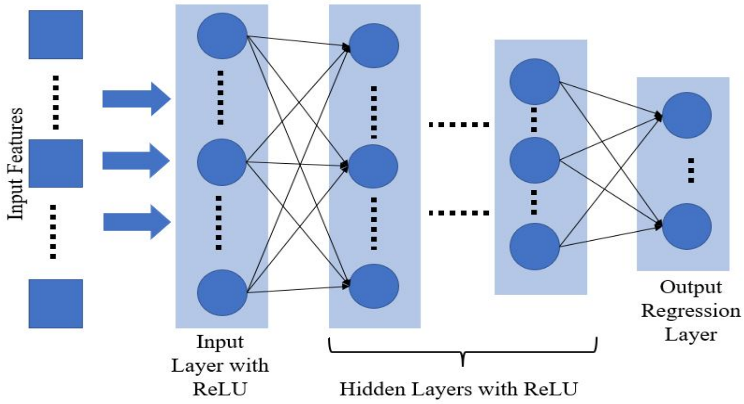

Figure 5.3: Proposed DNN model for training.

activation function. The regression layer is used for the output layer to predict a real-valued output. For online deployment output of the trained DNN model $\hat{x}$ is a cascade of nonlinear transformation of y,

$$\hat{\mathbf{x}} = f(\mathbf{y}, \mathbf{w}) = f^{L-1}(f^{L-2}(\ldots(f^{1}(\mathbf{y})))), \tag{5.25}$$

where L is the number of layers and $\mathbf{w}$ denotes the weights of the neural network. Thus, for the proposed architecture with 3 hidden layers, the estimated output is computed as:

$$\hat{\mathbf{x}} = f^{4}(f^{3}(f^{2}(f^{1}(\mathbf{y})))). \tag{5.26}$$

Before deploying the neural network online the weights for the neurons are optimized and, the optimal weights are obtained on a training set, with known desired outputs given in Eq. (5.3). The proposed DNN-based model is designed to minimize the error between the predicted output generated by the network and the actual transmitted data. This discrepancy is quantified by the L_2 loss or mean squared error (MSE) loss. The L_2 loss is a standard metric used in regression tasks, where the goal is to measure how well the predicted values align with the true values. The MSE loss function is chosen as the cost function owing to its sensitivity to large deviations and is given as

$$L_2 = \frac{1}{N_t}(\mathbf{x} - \hat{\mathbf{x}})^2, \tag{5.27}$$

where N_t is the number of training symbols per frame, and $\hat{\mathbf{x}}$ are the predicted

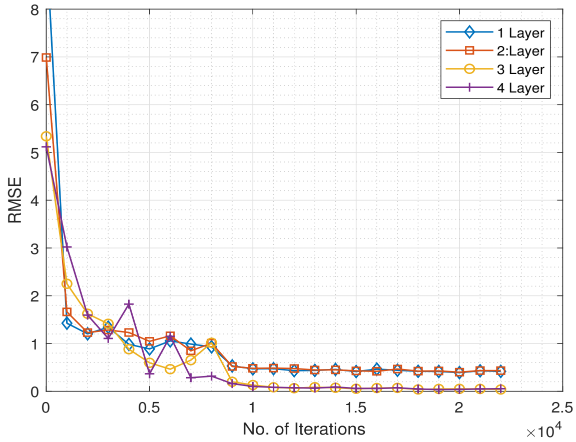

Figure 5.4: Root mean square error vs iteration plot by varying no. of layers.

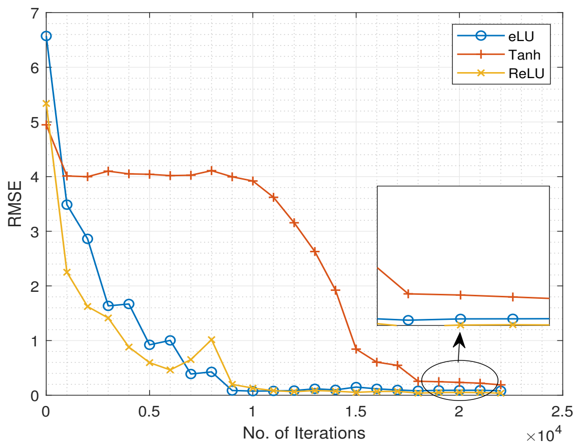

Figure 5.5: Root mean square error vs iteration plot by varying activation function.

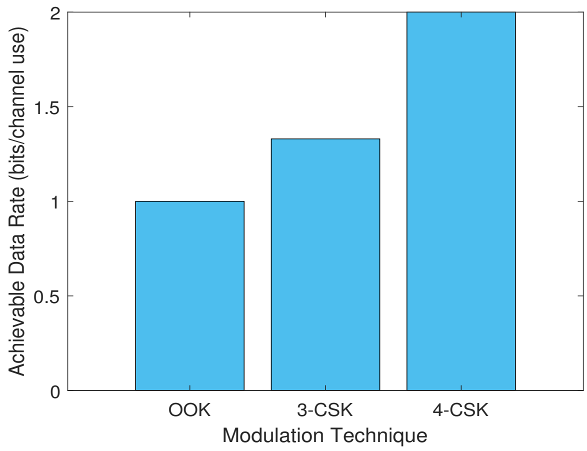

Figure 5.6: Achievable data rate for different modulation schemes.

symbols employing the trained DNN model. The number of training samples is determined through experimentation, starting with a minimal configuration of hidden layers and progressively increasing them until the DNN achieves satisfactory performance, as shown in Figure 5.4. It can be observed from Figure 5.4 that as the number of hidden layers is increased from 1 to 2, there is marginal enhancement in the performance. However, on further increasing the number of layers to 3, significant improvement in the performance can be observed. On further increasing the number of layers, no improvement was observed in addition to high computational complexity. Thus, for the neural network, the number of hidden layers is fixed to 3. The selection of an appropriate activation function was determined through comparative analysis of commonly used functions including eLU, ReLU, and tanh. Figure 5.5 presents the comparative performance metrics of these activation functions. Based on the results demonstrated in the performance curves, ReLU emerged as the optimal choice for the neural network architecture.

5.3.1 BER Analysis

In this section, we derive the BER for the CSK scheme. To estimate the BER, we first define the transition probability. The transition probability is defined as the probability of a symbol detected as another symbol i.e. the probability that a symbol transmitted, $\mathbf{x}_k$, is decoded incorrectly as another symbol, $\mathbf{x}_l$. This transition probability, also referred to as the symbol PEP, $P_e(\mathbf{x}_l|\mathbf{x}_k)$, can be calculated using decision region partitioning [58]. This method determines the transition probability

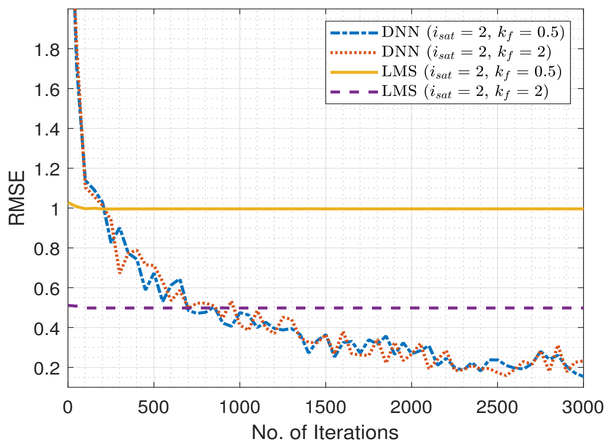

Figure 5.7: Root mean square error vs iteration for different modulation schemes.

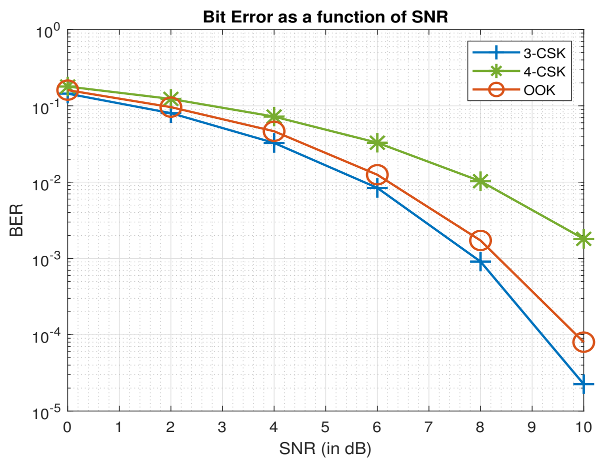

Figure 5.8: Bit error rate vs signal-to-noise ratio for different modulation schemes.

by evaluating the noise superimposed on the transmitted symbol within the decision regions of two types, I and II, characterized by parameters α, δ, γ, and β [58]. For type II decision regions, the transition probability is expressed as:

$$P_e(\mathbf{x}_l|\mathbf{x}_k) = \int_{\alpha}^{\gamma} \int_{R(\theta)}^{\infty} p_n(r,\theta) dr d\theta, \tag{5.28}$$

where $R(\theta) = \frac{\sqrt{\alpha |h|^2 \gamma} \sin(\beta)}{\sin(|\theta - \alpha| + \beta)}$, γ represents the SNR at the receiver, p_n is the PDF of the noise. Gauss formula denoted by $G(\cdot)$ can be used to numerically evaluate the definite integral given in (5.28) with the desired accuracy [58]. Therefore, if any symbol in the received sequence is incorrect, the entire sequence will be interpreted erroneously. The sequence PEP is given by:

$$P(\mathbf{S}_l|\mathbf{S}_k) = \prod_{i=1}^{N_s} P(\mathbf{x}_{l,i}|\mathbf{x}_{k,i}), \tag{5.29}$$

where $\mathbf{x}_{k,i}$ and $\mathbf{x}_{l,i}$ denote the i^{th} codewords corresponding to the transmitted $\mathbf{S}_k$, and the received $\mathbf{S}_l$ sequence, respectively. The Hamming distance $d(C_l, C_k)$ between the transmitted and the received code words gives the number of erroneous bits, where C_l and C_k are the codewords associated with sequence $\mathbf{S}_k$ and $\mathbf{S}_l$, respectively. Therefore, the obtained exact analytical expression of the BER, P_b, by summing all the PEP is

$$P_b = \frac{1}{M} \sum_{t=1}^{2^M} \sum_{r=1, r\neq t}^{3^{N_s}} d(C_l, C_k) P(\mathbf{S}_k) P(\mathbf{S}_l|\mathbf{S}_k), \tag{5.30}$$

where $P(\mathbf{x}_k)$ is the a priori probability of transmitting a sequence, $M = \lfloor \log_2 3^{N_s} \rfloor$ bits, where $\lfloor \cdot \rfloor$ is the floor operator and N_s is the number of symbols in the sequence ($N_s = 2$). It is assumed that no error correction coding is employed.

5.4 Numerical and Simulation Results

In this Section, we present the simulation results and compare the performance of OOK, 3-CSK, and 4-CSK for the proposed OSTAR-RIS aided indoor VLC system. The simulation parameters are summarized in Table 5.1.

Figure 5.6 compares the achievable data rates of the considered modulation tech-

Table 5.1: Simulation Parameters for CSK modulated OSTAR-RIS aided OTFS VLC systems[1]

Parameter	**Symbol**	**Specification**
Photodetector's responsivity	ρ	0.53 A/w
Photodetector's field-of-view (FOV)	ξ_{FoV}	85^{o}
Photodetector's area	A_D	1cm^2
Concentrator refractive index	$\mathrm{r_f}$	1.5
Gain optical filter	$G_o(\xi)$	1.0
Reflection coefficient of mirror array	χ_{RIS}	0.95
Reflection coefficient of wall	χ_{WALL}	0.8
Refractive index of air	η_a	1
Ordinary refractive index of LC cell	η_o	1.5
Extraordinary refractive index of LC cell	η_e	1.7
Depth of LC cell	D	0.75 mm
Electro-optic coefficient	E_o	12pm/V
Critical voltage threshold	V_{th}	1.34 V
Bandwidth	W	200 MHz

niques, i.e. OOK, 3-CSK, and 4-CSK. To ensure a fair comparison, equal symbol duration for all modulation techniques is assumed. It can be observed that 4-CSK can provide the maximum achievable data rate of 2 bits/channel use (bpcu). 3-CSK ($N_s = 2$) provides a better achievable data rate of 1.33 bpcu as compared to OOK which has an achievable data rate of 1 bpcu.

Figure 5.7 compares the RMSE performance of the proposed DNN-based receiver and traditional LMS-based algorithm by varying the nonlinearity parameter, i.e., knee factor (k_f). The performance of LMS deteriorates as the knee factor value is decreased from 2 to 0.5. This is due to the fact that the severity of the VLC system's nonlinearity increases on decreasing the knee factor. The DNN-based receiver shows consistent and better performance than LMS for both cases of nonlinearity considered. This further proves the robustness of DNN-based receivers.

Figure 5.8 depicts the BER performance of OOK, 3-CSK and, 4-CSK modulation techniques as a function of the SNR considering $k_f = 2$ and $i_{sat} = 2$. As expected, 4-CSK has the worst BER performance as it gives the maximum data rate, closely followed by the OOK, while, 3-CSK gives the best BER performance. BER of 10^{-2} is achieved at 6 dB, 6.2 dB and 8 dB, respectively, for 3-CSK, OOK and 4-CSK. Thus, 3-CSK provides a gain of 2 dB over 4-CSK.

5.5 Summary

In this chapter, a CSK modulation scheme was proposed to enhance the achievable data rate of ORIS-aided indoor VLC systems impaired by LED nonlinearity. A DNN-based symbol detector was proposed for direct symbol detection and compared with the traditional LMS-based channel estimator. In this context, 3-CSK and 4-CSK modulation techniques were introduced and compared with the OOK modulation technique. The provided simulation results demonstrated that 3-CSK offered the best BER performance compared to both 4-CSK and OOK and also a relatively higher achievable data rate as compared to OOK. Owing to its superior performance, 3-CSK is thus a desirable modulation technique for a variety of applications in OSTAR-RIS-aided indoor VLC systems, with different requirements which depend on data rate, reliable communication, and implementation complexity.

However, in addition to low data rate, and loss of the VLC signal due to the absence of a direct link the SSR of a VLC system is also compromised by the presence of an eavesdropper which we will analyze in the next chapter.

Chapter 6

NOMA OSTAR-RIS-Aided VLC Systems

In the previous chapter, the achievable user rate and BER performance of nonlinear VLC system was enhanced by employing CSK modulation scheme and DNN-based detection scheme. However, we considered only a scenario with no eavesdropper. An eavesdropper can intercept transmitted data, gaining unauthorized access to sensitive information. In scenarios like VLC, where the broadcast nature of light makes the signals easily detectable, this risk increases. The SSR performance of a VLC system is highly compromised due to the presence of an eavesdropper. Simultaneously, to address the growing data demands of users in VLC systems for beyond 5G communication, a novel multiple access scheme known as NOMA, or more specifically, power division multiple access, has garnered significant attention. [61–63]. Recently, NOMA has been recognized as a viable option for integration into STAR-RIS VLC systems for several reasons: (a) NOMA effectively manages a small number of users, which is typical in a Li-Fi attocell environment [12], and (b) tuning the angles of STAR-RIS and adjusting the FoV provide additional degrees of freedom for multiplexing signals of different users present in the environment. This results in differential channel gains, which enhance power diversity [64]. In [1], authors investigated power-domain NOMA and rate splitting multiple access (RSMA) to enhance the sum rate of optical STAR-RIS-Aided VLC systems. However, the impact of LED nonlinearity and the presence of eavesdroppers on the SSR has not yet been explored in OSTAR-VLC-based systems. For the maximization problem

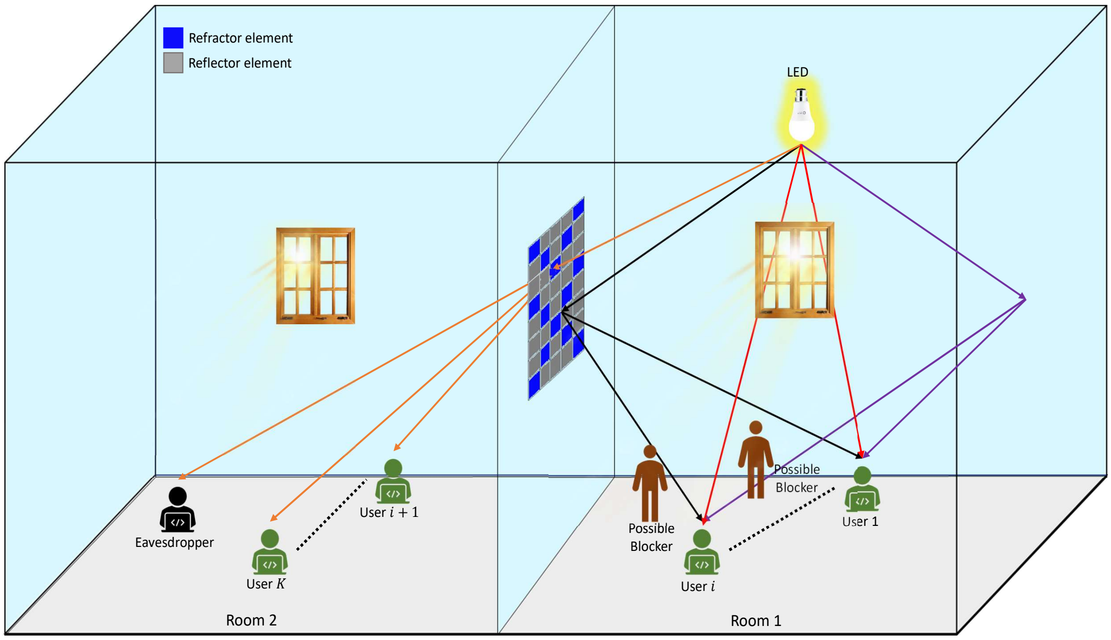

Figure 6.1: Optical simultaneously transmitting and reflecting-reflecting intelligent surface assisted indoor visible light communication system model.

of the SSR, authors in [65] have employed the particle swarm optimization (PSO) based method owing to its simplicity in optimum solutions to complex problems with efficient self-adaptability, robustness and lower complexity as compared to the straightforward exhaustive search method. Poor channel estimation can be caused by nonlinear distortions, which can seriously impair signal reception [13] and add an equivalent additive distortion at the receiver. Similarly, practical VLC systems also suffer from ambient and thermal noise. Ambient light noises may arise from sunlight, skylights, incandescent and fluorescent lamps, and other light sources present in the indoor environment. Furthermore, the transimpedence receiver circuitry produces the thermal noise. The primary contributions of this chapter are summarized as follows:

- A novel multi-user indoor VLC system employing NOMA and assisted by OSTAR-RIS is proposed. The impact of LED nonlinearity, ambient and thermal noise, device orientation, and the existence of non-user blockers are all taken into consideration in the proposed system.

- We thoroughly examine the design of the realistic STAR-RIS NOMA VLC system, taking into account both perfect and imperfect successive interference cancellation (SIC) and CSI.

- For a special case of two users, we propose a PSO-based solution to the problem of maximizing the SSR by optimizing the roll and yaw angle of the STAR-RIS, refractive indices of the LC cell, and power allocation factor for NOMA within some constraints. The same can be further extended to more than two user scenarios.

- Detailed simulation results demonstrate that the NOMA scheme outperforms the OMA scheme for the proposed system, particularly in terms of the SSR.

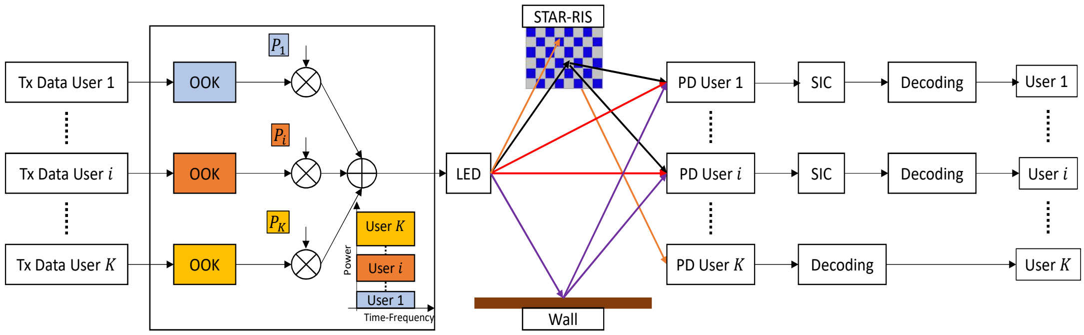

Figure 6.2: Considered indoor visible light communication system model.

6.0.1 System Model

We consider a realistic indoor OSTAR-RIS-assisted VLC system, as shown in Figure 6.1, where we consider N-low-cost passive elements on the OSTAR-RIS mounted on a wall between Room 1 and Room 2. The LED is in the centre of the ceiling of Room 1 and serves K users in the two rooms simultaneously by modulating the intensity of the light emitted. The eavesdropper is assumed to be in Room 2. Multiple blockers are also present in Room 1, which can potentially block the path of light. The OSTAR-RIS is composed of κ and ϑ MA-based and LC-based elements, respectively, such that $\kappa + \vartheta = N$. The mirror elements on the OSTAR-RIS act as reflector elements, while the LC-based elements act as refractor elements. As the channel strength of the users present in Room 1 is stronger than the users present in Room 2, the channel strength of all the users can be sorted out as $h_1 \geq \cdots \geq h_i \geq \cdots \geq h_K$. Without the loss of generality, we assume that the users in Room 1, i.e. User 1,$\cdots$, User i, are sorted in a descending order according to their channels, i.e. $h_1 \geq h_2 \geq \cdots \geq h_i$. Similarly, users in Room 2, i.e. User $i+1$,$\cdots$, User K, are sorted in a descending order according to their channels, i.e. $h_{i+1} \geq h_{i+2} \geq \cdots \geq h_K$. As shown in the considered indoor VLC system model shown in Figure 6.2, using NOMA, the LED transmits the OOK symbols $s_1, \cdots, s_K$ with associated power values $P_1, \cdots, P_K$, where s_j conveys information intended for the j^{th} user. Thus, the K transmitted signals are superimposed in the power domain as follows:

$$x = \sum_{j=1}^{K} P_j s_j, \tag{6.1}$$

where $P_j = \alpha P_{j-1}$, α denotes the power allocation factor ($0 < \alpha < 1$), and the LED peak transmit power is expressed as

$$P_T = \sum_{j=1}^{K} P_j. \tag{6.2}$$

These modulated symbols are transmitted through a forward-biased LED with nonlinear characteristics, which distorts the symbols. As LEDs have AM/AM modelling, the nonlinear characteristic is modelled by Rapp's model as follows:

$$\hat{s} = f(x) = \frac{x}{(1 + (\frac{x}{\mathrm{i_{sat}}})^{2\mathrm{k_f}})^{\frac{1}{2\mathrm{k_f}}}}, \tag{6.3}$$

where $\mathrm{i_{sat}}$ and $\mathrm{k_f}$ are the saturation current and knee factor of the LED, respectively. The knee factor regulates the transitional smoothness of LED features from the linear to the saturation region. With the aid of the Bussgang theorem, if the input signal of a memoryless nonlinear function is Gaussian, then the output of the function corrupted by a distortion component can be expressed in the form of the input signal as its scaled version. Therefore, we have

$$\hat{s} = \varsigma x + z_{dis}, \tag{6.4}$$

where ς is the scaling factor and z_{dis} is the distortion signal with zero mean and variance σ_d^2. The resulting signal, $\hat{s}$, is transmitted over a VLC channel. For the users and eavesdropper, the effective channel is given as

$$h_j^{\text{eff}} = \begin{cases} h_j^{\text{LoS}} + h_j^{\text{MA}} + h_j^{\text{Wall}}, 1 \leq j \leq i, \\ h_j^{\text{LC}}, i+1 \leq j \leq K, \end{cases} \tag{6.5}$$

$$h_{\text{eav}}^{\text{eff}} = h_{\text{eav}}^{\text{LC}}, \tag{6.6}$$

where h_j^{LoS} is the LoS path between the LED and the j^{th} users, h_j^{MA} and h_j^{Wall} are the NLoS reflected channels of the j^{th} user reflected from the MA elements of OSTAR-RIS and the wall, respectively. Similarly, h_j^{LC} and $h_{\text{eav}}^{\text{LC}}$ are the channel gain of the j^{th} user and eavesdropper, respectively, refracted from the LC element of the OSTAR-RIS. Subsequently, at the receiver, the transmitted signal is received by the photodetector of the users and the eavesdropper as follows:

$$y_j = \rho h_j^{\text{eff}} \sum_{m=1}^{K} P_m \hat{s}_m + n_j, \tag{6.7}$$

$$y_{eav} = \rho h_{eav}^{\text{eff}} \sum_{m=1}^{K} P_m \hat{s}_m + n_{eav}, \tag{6.8}$$

where $\mathbf{y}_j$ and $\mathbf{y}_{eav}$, are the symbol vectors received by the j^{th} user and eavesdropper, respectively, ρ is the responsivity of the photodetector, n_j and n_{eav} are all zero mean i.i.d. AWGN with variance σ^2, $\sigma^2 = \sigma_a^2 + \sigma_t^2$ and σ_a^2 and σ_t^2 are the variances of ambient light noise and thermal noise, respectively. At the receiver, as per the mechanism of NOMA, User 1 to User $K-1$ adopt SIC to decode the messages with the same decoding order. As it is assumed that User K has the weakest channel, it can directly decode its own message without performing SIC.

6.0.2 VLC Channel

The LoS channel between the LED and the j^{th} user in Room 1 follows the Lambertian model within the FoV $0 \leq \xi \leq \xi_{\text{FoV}}$ as

$$h_j^{\text{LoS}} = \iota \left(\frac{(L+1)\, A_{\text{PD}} \cos^L(\phi)\, G_o(\xi)\, G_i(\xi) \cos(\xi)}{2\pi d_j^2} \right), \tag{6.9}$$

where $\iota \in 0, 1$ a parameter to indicate whether the LoS path is present or blocked by possible blockers, L represents the Lambertian index and can be computed as

$$L = \left(\log_2 \frac{1}{\cos(\theta_{1/2})} \right)^{-1}, \tag{6.10}$$

$\theta_{1/2}$ represents the angle of half-intensity radiation. The physical surface area of the photodetector is denoted by A_{PD}, ϕ and ξ are the angles of irradiance and incidence, respectively, d_j is the distance between the LED and the j^{th} user, $G_o(\xi)$ and $G_i(\xi)$ denotes the gain of the optical filter and the non-imaging concentrator, i.e. $G_i(\xi)$ is defined as

$$G_i(\xi) = \frac{\mathrm{r_f}^2}{\sin^2 \xi_{\mathrm{FoV}}}, \tag{6.11}$$

The refractive index of the concentrator is denoted by $\mathrm{r_f}$. The cosine of ξ can be computed in terms of the azimuth angle (α_a) and the elevation angle (α_e) of the device as

$$\begin{aligned} \cos(\xi) = &\left(\frac{x_l - x_j}{d_{l,j}} \right) \sin(\alpha_e) \cos(\alpha_a) + \left(\frac{y_l - y_j}{d_{l,j}} \right) \sin(\alpha_e) \\ &\times \sin(\alpha_a) + \left(\frac{z_l - z_j}{d_{l,j}} \right) \cos(\alpha_e), \end{aligned} \tag{6.12}$$

The position vectors specifying location of the LED is denoted by (x_l, y_l, z_l) and the position vectors specifying location of the j^{th} user is denoted by (x_j, y_j, z_j). $d_{l,j}$ is the distance between the LED and the j^{th} user. For modelling the elevation angle, the Laplace distribution with the mean and the standard deviation of 41^{o} and 9^{o} is used, respectively. The range of the elevation angle is typically considered to be $[0, \frac{\pi}{2}]$. The uniform distribution $\alpha_a \sim \mathcal{U}[-\pi, \pi]$ is considered for the azimuth angle.

In Room 1, the NLoS channel of the j^{th} user after reflection from the wall is computed as

$$h_j^{\mathrm{Wall}} = \chi_{\mathrm{wall}} \frac{(L+1) A_{\mathrm{PD}}}{2\pi^2 d_{l,k}^2 d_{j,k}^2} dA \cos^L(\phi_{l,k}) \cos(\xi_{l,k}) \cos(\phi_{j,k}) \cos(\xi_{j,k})\, G_o(\xi_{l,k})\, G_i(\xi_{j,k}), \tag{6.13}$$

where χ_{wall} is the reflection coefficient of the wall surface, and dA represents the area of the wall segment. The LED-to-k^{th} wall segment distance is denoted by $d_{l,k}$, and the distance between the k^{th} wall segment and the j^{th} user is $d_{j,k}$. The angles of irradiance from the LED to the wall segment and from the wall segment towards the j^{th} user are $\phi_{l,k}$ and $\phi_{j,k}$, respectively. The angles of incidence on the wall and on the j^{th} user are $\xi_{l,k}$ and $\xi_{j,k}$, respectively. Similarly, the NLoS channel of users in Room 1 after reflection from the OSTAR-RIS is computed as

$$h_j^{\mathrm{MA}} = \chi_{\mathrm{RIS}} \frac{(L+1)A_{\mathrm{PD}}}{2\pi^2 d_{l,i}^2 d_{j,i}^2} dA \cos^L(\phi_{l,i}) \cos(\xi_{l,i}) \cos(\phi_{j,i}) \cos(\xi_{j,i}) G_o(\xi_{l,i}) G_i(\xi_{j,i}), \tag{6.14}$$

where the reflection coefficient of the MA in OSTAR-RIS is denoted by the χ_{RIS}. The distance between the LED and the i^{th} OSTAR-RIS segment is denoted by $d_{l,i}$, while $d_{j,i}$ is the distance between i^{th} MA and the j^{th} user. The angles of irradiance from the LED to the MA and the MA to the j^{th} user are denoted as $\phi_{l,i}$ and $\phi_{j,i}$, respectively. The angle of incidence on the MA and the j^{th} user are $\xi_{l,i}$ and $\xi_{j,i}$, respectively. The cosine of the angle of irradiance is represented in the form of the yaw (γ_{MA}) and roll (ω_{MA}) angles of the MA elements of the OSTAR-RIS array and can be computed as

$$\begin{aligned} \cos(\phi_{j,i}) = &\frac{(x_i - x_j)}{d_{j,i}} \sin(\gamma_{MA}) \cos(\omega_{MA}) + \frac{(y_i - y_j)}{d_{j,i}} \\ &\times \cos(\gamma_{MA}) \cos(\omega_{MA}) + \frac{(z_i - z_j)}{d_{j,i}} \sin(\omega_{MA}), \end{aligned} \tag{6.15}$$

where (x_i, y_i, z_i) represents the coordinates of the i^{th} element of the OSTAR-RIS. Similarly, for users in Room 2, the effective channel is given by

$$h_j^{\mathrm{LC}} = \begin{cases} \psi_{\mathrm{LC}} \frac{(L+1)A_D}{2\pi^2 \left(d_{l,i}\right)^2 (d_{j,i})^2} dA G_o(\xi_{l,i}) G_i(\xi_{l,i}) \cos^L(\phi_{l,i}) \\ \times \cos(\xi_{l,i}) \cos(\phi_{j,i}) \cos(\xi_{j,i}), 0 \le \xi_{j,i} \le \xi_{\mathrm{FoV}}, \\ 0, \qquad \xi_{j,i} > \xi_{\mathrm{FoV}}, \end{cases} \tag{6.16}$$

where

$$\cos\left(\phi_{j,i}\right) = \left(\frac{x_i - x_j}{d_{j,i}}\right)\sin\left(\gamma_{LC}\right)\cos\left(\omega_{LC}\right) + \left(\frac{y_i - y_j}{d_{j,i}}\right) \\ \times \cos\left(\gamma_{LC}\right)\cos\left(\omega_{LC}\right) + \left(\frac{z_i - z_j}{d_{j,i}}\right)\sin\left(\omega_{LC}\right), \tag{6.17}$$

where yaw (γ_{LC}) and roll (ω_{LC}) are the angles of the LC elements of the OSTAR-RIS array. The transition coefficient, ψ_{LC}, can be given by

$$\psi_{\text{LC}} = T_{\text{an}}\left(\xi_{j,i}\right) \times T_{\text{na}}\left(\theta\right), \tag{6.18}$$

where the angular transmittance as the signal enters and exits the LC cell is denoted by $T_{\text{an}}\left(\xi_{j,i}\right)$ and $T_{\text{na}}\left(\theta\right)$. They can be respectively expressed in terms of the angular reflectance as $T_{\text{an}}\left(\xi_{j,i}\right) = 1 - R_{\text{an}}\left(\xi_{j,i}\right)$ and $T_{\text{na}}\left(\theta\right) = 1 - R_{\text{na}}\left(\theta\right)$. The angular reflectance can be derived as

$$R_{\text{an}}\left(\xi_{j,i}\right) = \frac{1}{2}\left(\frac{\eta^2\cos\left(\xi_{j,i}\right) - \sqrt{\eta^2 - \sin^2\left(\xi_{j,i}\right)}}{\eta^2\cos\left(\xi_{j,i}\right) + \sqrt{\eta^2 - \sin^2\left(\xi_{j,i}\right)}}\right)^2 + \frac{1}{2}\left(\frac{\cos\left(\xi_{j,i}\right) - \sqrt{\eta^2 - \sin^2\left(\xi_{j,i}\right)}}{\cos\left(\xi_{j,i}\right) + \sqrt{\eta^2 - \sin^2\left(\xi_{j,i}\right)}}\right)^2, \tag{6.19}$$

$$R_{\text{na}}\left(\theta\right) = \frac{1}{2}\left(\frac{\cos\left(\theta\right) - \sqrt{\eta_r^2 - \sin^2\left(\theta\right)}}{\cos\left(\theta\right) + \sqrt{\eta_r^2 - \sin^2\left(\theta\right)}}\right)^2 + \frac{1}{2}\left(\frac{\eta_r^2\cos\left(\theta\right) - \sqrt{\eta_r^2 - \sin^2\left(\theta\right)}}{\eta_r^2\cos\left(\theta\right) + \sqrt{\eta_r^2 - \sin^2\left(\theta\right)}}\right)^2, \tag{6.20}$$

where $\eta = {}^{\eta_c}/_{\eta_a}$ and $\eta_r = {}^{\eta_a}/_{\eta_c}$ denotes the relative refractive indices and η_c and η_a represent the refractive indices of the LC cell and air, respectively. The range of η_c varies from 1.5 to 1.7 and needs to be tuned because ψ_{LC} can be optimized by tuning η_c. In the ORIS light amplification for the emerging signal can be achieved by the LC elements via stimulated emission. Beer's absorption law can be used to determine the output signal power P_{out} following the amplification of light signal in the presence of an external electric field when an optical signal with power P_{in} refracts from an LC cell with the transition coefficient ψ_{LC}:

$$P_{\text{out}} = P_{\text{in}} \times \exp\left(A_{GC}D\right) \times \psi_{\text{LC}}, \tag{6.21}$$

where the amplification gain coefficient denoted as A_{GC} is given by

$$A_{GC} = \frac{2\pi\eta_c^3}{\cos\left(\xi_{\hat{u}}^n\right)\lambda} E_o E, \tag{6.22}$$

The LC cell's depth is indicated by D, and the exponential rise in incident signal power is shown by the expression $\exp(A_{GC}D)$. In (6.22), λ is the wavelength of the optical signal, E_o is the electro-optic coefficient, and E (in V/m) is the external electric field. The external electric field E can be calculated as $E = {}^{V_E}/_{D}$, where V_E is

$$V_{\mathrm{E}} = V_{\mathrm{TH}} - \log\left(-\tan\left[\frac{\tan^{-1}\left(\frac{\eta_o\sqrt{(\eta_e^2-\eta_o^2)(\eta_e^2-\eta_c^2)}}{\eta_c(\eta_e^2-\eta_o^2)}\right)}{2} - \frac{\pi}{4}\right]\right). \tag{6.23}$$

where η_e and η_o denote the extraordinary and ordinary refractive indices of the LC based element's in OSTAR-RIS, respectively. Similar to users in Room 2, the effective channel of the eavesdropper can be computed.

6.1 Performance Analysis

In this section, we formulate the analytical expression of SSR for the OSTAR-RIS-VLC-NOMA system impaired by LED nonlinearity for both scenarios with both perfect and imperfect SIC and CSI operations. For the sake of simplicity and deep insight into the performance of NOMA, we will consider a two-user ($K = 2$, $i = 1$) system such that one user is present in Room 1 and another user is present in Room 2 with an eavesdropper. The obtained insight can be extended to a general scenario with more users. Depending on the characteristics of the channel, users might be grouped into several clusters. The same time-frequency resources are used to transmit user signals inside the same cluster [66]. To perform SIC successfully within each cluster, the differences in the users' channel conditions need to be sufficiently large [67–69].

6.1.1 OSTAR-RIS-VLC-NOMA with perfect CSI and SIC

We first derive the expressions for the received SINR and sum rate considering perfect CSI and SIC. Based on (6.7) for two users, the received signal can be written as

$$r_1 = \rho h_1^{\text{eff}}(\zeta(P_1 s_1 + P_2 s_2) + z_{dis}) + n_1, \tag{6.24}$$

$$r_2 = \rho h_2^{\text{eff}}(\zeta(P_1 s_1 + P_2 s_2) + z_{dis}) + n_2. \tag{6.25}$$

where $h_1^{\text{eff}} = h_1^{\text{LoS}} + h_1^{\text{MA}} + h_1^{\text{Wall}}$, $P_1 = {}^{P_T}/_{1+\alpha}$ and $P_2 = {}^{\alpha P_T}/_{1+\alpha}$. As User 1 is the strong user, carried out SIC, where User 2 decodes its own signal directly. Therefore, in the case of perfect CSI and SIC, the received the SINR at User 1 to decode User 2's message directly is

$$\text{SINR}_1^2 = \frac{|\rho\zeta P_2 h_1^{\text{eff}}|^2}{\sigma^2 + |\rho\zeta P_1 h_1^{\text{eff}}|^2 + |\rho h_1^{\text{eff}}\sigma_d|^2}. \tag{6.26}$$

where $\sigma^2 = \sigma_a^2 + \sigma_t^2$. SINR at User 1, when User 1 decodes its own message, is

$$\text{SINR}_1^1 = \frac{|\rho\zeta P_1 h_1^{\text{eff}}|^2}{\sigma^2 + |\rho h_1^{\text{eff}}\sigma_d|^2}. \tag{6.27}$$

Similarly, the received SINR at User 2 on decoding its own message is

$$\text{SINR}_2^2 = \frac{|\rho\zeta P_2 h_2^{\text{eff}}|^2}{\sigma^2 + |\rho\zeta P_1 h_2^{\text{eff}}|^2 + |\rho h_2^{\text{eff}}\sigma_d|^2}. \tag{6.28}$$

The received SINRs at the eavesdropper of the message $\hat{s}_1$ and $\tilde{s}_2$ is

$$\text{SINR}_e^1 = \frac{|\rho\zeta P_1 h_{\text{eav}}^{\text{eff}}|^2}{\sigma^2 + |\rho\zeta P_2 h_{\text{eav}}^{\text{eff}}|^2 + |\rho h_{\text{eav}}^{\text{eff}}\sigma_d|^2}, \tag{6.29}$$

$$\text{SINR}_e^2 = \frac{|\rho\zeta P_2 h_{\text{eav}}^{\text{eff}}|^2}{\sigma^2 + |\rho\zeta P_1 h_{\text{eav}}^{\text{eff}}|^2 + |\rho h_{\text{eav}}^{\text{eff}}\sigma_d|^2}. \tag{6.30}$$

Thus, the respective rates across the User 1 (R_{u1}), User 2 (R_{u2}) and the eavesdropper (R_{eav}) can be computed as

$$R_{u1} = \frac{W}{2}\log_2\left(1+\mathrm{SINR}_1^1\right), \tag{6.31}$$
$$R_{u2} = \frac{W}{2}\log_2\left(1+\mathrm{SINR}_2^2\right), \tag{6.32}$$
$$R_{eav}^1 = \frac{W}{2}\log_2\left(1+\mathrm{SINR}_e^1\right), \tag{6.33}$$
$$R_{eav}^2 = \frac{W}{2}\log_2\left(1+\mathrm{SINR}_e^2\right). \tag{6.34}$$

where the available modulation bandwidth is denoted by W. The SSR of the proposed system can be defined as

$$R_{sec} = [R_{u1} + R_{u2} - R_{eav}^1 - R_{eav}^2]^+, \tag{6.35}$$

where $[a]^+ = \max(0, a)$. The goal is to maximize the SSR, which depends on parameters γ_{MA}, ω_{MA}, η_c and α.

6.1.2 OSTAR-RIS-VLC-NOMA with imperfect CSI

In this section, we have analyzed the impact of imperfect CSI on the performance of OSTAR-RIS-VLC systems. NOMA configurations rely heavily on having precise channel coefficients for all users. This is pivotal for the receiver to recover data successfully and for the transmitter to determine the appropriate power allocation for each user. To effectively utilize SIC, users must receive signals at different power levels depending on their channel gains. However, assuming perfect CSI is impractical for indoor VLC systems. Quantization errors are introduced during the ADC of channel estimates [70]. Thus, quantifying the impact of CSI imperfection on NOMA OSTAR-RIS VLC system performance is therefore crucial. In this context, the following noisy CSI model is considered:

$$\hat{h}_j^{eff} = h_j^{eff} + \epsilon_n, \tag{6.36}$$

where the channel estimation error is denoted by ϵ_n and is modeled with a zero-mean Gaussian distribution with variance $\sigma_{\epsilon_n}^2$, i.e, $\epsilon_n \sim \mathcal{N}(0, \sigma_{\epsilon_n}^2)$, reasonable model commonly used for indoor VLC systems [71, 72]. Consequently, it immediately follows that the channel estimate $\hat{h}_j^{eff}$ can be represented as $\hat{h}_j^{eff} \sim \mathcal{N}(h_j^{eff}, \sigma_{\epsilon_n}^2)$. Thus, the SINRs for the users and eavesdropper in the presence of imperfect CSI are:

$$\mathrm{SINR}_1^2|_{\mathrm{CSI}} = \frac{|\rho\zeta P_2 \hat{h}_1^{\mathrm{eff}}|^2}{\sigma^2 + |\rho\zeta P_2 \sigma_{\epsilon_n}|^2 + |\rho\zeta P_1 \hat{h}_1^{\mathrm{eff}}|^2 + |\rho \hat{h}_1^{\mathrm{eff}} \sigma_d|^2}. \tag{6.37}$$

$$\mathrm{SINR}_1^1|_{\mathrm{CSI}} = \frac{|\rho\zeta P_1 \hat{h}_1^{\mathrm{eff}}|^2}{\sigma^2 + |\rho\zeta P_1 \sigma_{\epsilon_n}|^2 + |\rho \hat{h}_1^{\mathrm{eff}} \sigma_d|^2}. \tag{6.38}$$

$$\mathrm{SINR}_2^2|_{\mathrm{CSI}} = \frac{|\rho\zeta P_2 \hat{h}_2^{\mathrm{eff}}|^2}{\sigma^2 + |\rho\zeta P_2 \sigma_{\epsilon_n}|^2 + |\rho\zeta P_1 \hat{h}_2^{\mathrm{eff}}|^2 + |\rho \hat{h}_2^{\mathrm{eff}} \sigma_d|^2}. \tag{6.39}$$

$$\mathrm{SINR}_e^1|_{\mathrm{CSI}} = \frac{|\rho\zeta P_1 \hat{h}_{\mathrm{eav}}^{\mathrm{eff}}|^2}{\sigma^2 + |\rho\zeta P_1 \sigma_{\epsilon_n}|^2 + |\rho\zeta P_2 \hat{h}_{\mathrm{eav}}^{\mathrm{eff}}|^2 + |\rho \hat{h}_{\mathrm{eav}}^{\mathrm{eff}} \sigma_d|^2}. \tag{6.40}$$

$$\mathrm{SINR}_e^2|_{\mathrm{CSI}} = \frac{|\rho\zeta P_2 \hat{h}_{\mathrm{eav}}^{\mathrm{eff}}|^2}{\sigma^2 + |\rho\zeta P_2 \sigma_{\epsilon_n}|^2 + |\rho\zeta P_1 \hat{h}_{\mathrm{eav}}^{\mathrm{eff}}|^2 + |\rho \hat{h}_{\mathrm{eav}}^{\mathrm{eff}} \sigma_d|^2}. \tag{6.41}$$

6.1.3 OSTAR-RIS-VLC-NOMA with imperfect SIC

In this section, we have analyzed the impact of imperfect SIC on the performance of OSTAR-RIS-VLC systems. The imperfect SIC occurs during the decoding process when a fraction residue at the channel-information properties is left due to SIC errors causing imperfect SIC at the receiver. For imperfect SIC receiver signals, User 1 does not have perfect knowledge of User 2's signal information. Consequently, User 2's signal is not perfectly removed at User 1. This scenario can be modeled by incorporating the effect of VLC channel interference, resulting in a more realistic situation compared to the ideal case of perfect SIC. Thus, the SINR for User 1 decoding its own message considering imperfect SIC is:

$$\mathrm{SINR}_1^1|_{\mathrm{SIC}} = \frac{|\rho\zeta P_1 h_1^{\mathrm{eff}}|^2}{\sigma^2 + \beta|\rho\zeta P_2 h_1^{\mathrm{eff}}|^2 + |\rho h_1^{\mathrm{eff}} \sigma_d|^2}. \tag{6.42}$$

where β is the residual interference due to imperfect SIC, $0 \leq \beta \leq 1$, and $\beta = 0$ refers to perfect SIC.

Thus, the SINRs of respective users and eavesdropper under imperfect CSI and

SIC can be computed as:

$$\mathrm{SINR}_1^2|_{\mathrm{I}} = \frac{|\rho\zeta P_2 \hat{h}_1^{\mathrm{eff}}|^2}{\sigma^2 + |\rho\zeta P_1 \hat{h}_1^{\mathrm{eff}}|^2 + |\rho\zeta P_2 \sigma_{\epsilon_n}|^2 + |\rho \hat{h}_2^{\mathrm{eff}} \sigma_d|^2}. \tag{6.43}$$

$$\mathrm{SINR}_1^1|_{\mathrm{I}} = \frac{|\rho\zeta P_1 \hat{h}_1^{\mathrm{eff}}|^2}{\begin{Bmatrix} \sigma^2 + |P_2 \hat{h}_1^{\mathrm{eff}}|^2 + \beta |P_2 \hat{h}_1^{\mathrm{eff}}|^2 \\ + |P_1 \sigma_{\epsilon_n}|^2 + |\rho \hat{h}_2^{\mathrm{eff}} \sigma_d|^2 \end{Bmatrix}}. \tag{6.44}$$

$$\mathrm{SINR}_2^2|_{\mathrm{I}} = \frac{|\rho\zeta P_2 \hat{h}_2^{\mathrm{eff}}|^2}{\sigma^2 + |P_2 \sigma_{\epsilon_n}|^2 + |\rho \hat{h}_2^{\mathrm{eff}} \sigma_d|^2}. \tag{6.45}$$

$$\mathrm{SINR}_e^1|_{\mathrm{I}} = \frac{|\rho\zeta P_1 \hat{h}_{\mathrm{eav}}^{\mathrm{eff}}|^2}{\begin{Bmatrix} \sigma^2 + |P_2 \hat{h}_{\mathrm{eav}}^{\mathrm{eff}}|^2 + \beta |P_2 \hat{h}_{\mathrm{eav}}^{\mathrm{eff}}|^2 \\ + |P_1 \sigma_{\epsilon_n}|^2 + |\rho \hat{h}_2^{\mathrm{eff}} \sigma_d|^2 \end{Bmatrix}}. \tag{6.46}$$

$$\mathrm{SINR}_e^2|_{\mathrm{I}} = \frac{|\rho\zeta P_2 \hat{h}_{\mathrm{eav}}^{\mathrm{eff}}|^2}{\begin{Bmatrix} \sigma^2 + |P_1 \hat{h}_{\mathrm{eav}}^{\mathrm{eff}}|^2 + \beta |P_2 \hat{h}_{\mathrm{eav}}^{\mathrm{eff}}|^2 \\ + |P_2 \sigma_{\epsilon_n}|^2 + |\rho \hat{h}_2^{\mathrm{eff}} \sigma_d|^2 \end{Bmatrix}}. \tag{6.47}$$

Similarly, the data rates of the users and eavesdropper in the presence of imperfect CSI and SIC would be:

$$\hat{R}_{u1} = \frac{W}{2} \log_2 \left(1 + \mathrm{SINR}_1^1|_{\mathrm{I}}\right). \tag{6.48}$$

$$\hat{R}_{u2} = \frac{W}{2} \log_2 \left(1 + \mathrm{SINR}_2^2|_{\mathrm{I}}\right). \tag{6.49}$$

$$\hat{R}_{eav}^1 = \frac{W}{2} \log_2 \left(1 + \mathrm{SINR}_e^1|_{\mathrm{I}}\right). \tag{6.50}$$

$$\hat{R}_{eav}^2 = \frac{W}{2} \log_2 \left(1 + \mathrm{SINR}_e^2|_{\mathrm{I}}\right). \tag{6.51}$$

Thus, the SSR of the proposed system with imperfect CSI and SIC can be defined as

$$\hat{R}_{sec} = [\hat{R}_{u1} + \hat{R}_{u2} - \hat{R}_{eav}^1 - \hat{R}_{eav}^2]^+. \tag{6.52}$$

The goal is to maximize the SSR, which depends on parameters γ_{MA}, ω_{MA}, η_c and α.

6.1.4 BER analysis with perfect CSI

In this section, we will derive the BER equations for our proposed OSTAR-RIS NOMA VLC system, considering perfect CSI. Considering OOK modulation for transmitting signal, the probability of error ($P_{e,U2}$) for the User 2 can be expressed as

$$\begin{aligned}P_{e,U2} &= P(y_2 = 1|s_1 = 0, s_2 = 0)P(s_1 = 0, s_2 = 0) + P(y_2 = 0|s_1 = 0, s_2 = 1)P(s_1 = 0, s_2 = 1)\\ &+ P(y_2 = 1|s_1 = 1, s_2 = 0)P(s_1 = 1, s_2 = 0) + P(y_2 = 0|s_1 = 1, s_2 = 1)P(s_1 = 1, s_2 = 1).\end{aligned} \tag{6.53}$$

It is assumed that the symbols of User 1 and User 2 are independent, such that $P(s_1, s_2) = P(s_1)P(s_2)$. Thus,

$$\begin{aligned}P_{e,U2} = \frac{1}{4}\{&P\left(n_2 > i_{th_2}\right) + P\left(2P_2\rho h_2^{eff} + n_2 < i_{th_2}\right) + P\left(2P_1\rho h_2^{eff} + n_2 < i_{th_2}\right)\\ &+ P\left(2P_1\rho h_2^{eff} + 2P_2\rho h_2^{eff} + n_2 < i_{th_2}\right)\},\end{aligned} \tag{6.54}$$

where i_{th_2} is the threshold for User 2 symbol detection and $2P_2\rho h_2^{eff}$ is the generated photocurrent at User 2. It is to be noted that $y_k, k \in (1, 2)$, defined in (6.9) is a Gaussian distributed random variable with the PDF

$$f_{y_k}(l) = \frac{1}{\sqrt{2\pi\sigma_k^2}} e^{-(l-m_k)^2/2\sigma_k^2}, \tag{6.55}$$

where $m_k = 2P_1\rho h_j^{eff} s_1 + 2P_2\rho h_j^{eff} s_2$ and $\sigma_k^2 = \sigma_n^2$ are the mean and variance of the k^{th} user. The probability of error of $y_k, y_k \neq s_k$, can be given as

$$\begin{aligned}P\left(y_k = 1 \mid s_1, s_2\right) &= \frac{1}{\sqrt{2\pi\sigma_k^2}} \int_{i_{m_k}}^{\infty} e^{-(l-m_k)^2/2\sigma_k^2} dl\\ &= \frac{1}{2}\,\mathrm{erfc}\left(\frac{i_{lk_k} - m_k}{\sqrt{2}\sigma_k}\right).\end{aligned} \tag{6.56}$$

Similarly,

$$P\left(y_k=0 \mid s_1, s_2\right)=\frac{1}{\sqrt{2\pi\sigma_k^2}}\int_{-\infty}^{i_{lk_k}} e^{-(l-m_k)^2/2\sigma_k^2}dl$$
$$=\frac{1}{2}\operatorname{erfc}\left(\frac{m_k-i_{k_k}}{\sqrt{2}\sigma_k}\right). \tag{6.57}$$

Thus, using (6.56) and (6.57), (6.54) can be solved as

$$P_{e,U2}=\frac{1}{4}\left\{2Q\left(\beta_1 P_2\right)+Q\left(\beta_1\left(P_2-2P_1\right)\right)+Q\left(\beta_1\left(2P_1+P_2\right)\right)\right\}, \tag{6.58}$$

where $\beta_1 = {}^{\rho h_2^{eff}}/_{\sigma}$ The probability of error for the User 1 can be given as

$$P_{e,U1}=P'_{e,U1}P^{U1}_{c,U2}+P''_{e,U1}P^{U1}_{e,U2}, \tag{6.59}$$

where $P'_{e,U1}$ is the error probability of User 1's signal when User 2's signal is correctly decoded at User 1, i.e., SIC is successfully implemented, $P''_{e,U1}$ is the error probability of User 1's signal when User 2's signal is incorrectly decoded at User 1, i.e., failure of SIC, $P^{U1}_{c,U2}=1-P^{U1}_{e,U2}$ is the probability that User 2's signal is correctly decoded at User 1, and $P^{U1}_{e,U2}$ is the error probability of User 2's signal decoded at User 1. The terms involved in (6.59) are derived below. The probability of error for User 2's signal decoded by User 1 can be given as

$$\begin{aligned}P^{U1}_{e,U2}=&P\left(y_1=1 \mid s_1=0, s_2=0\right)P\left(s_1=0, s_2=0\right)\\&+P\left(y_1=0 \mid s_1=0, s_2=1\right)P\left(s_1=0, s_2=1\right)\\&+P\left(y_1=1 \mid s_1=1, s_2=0\right)P\left(s_1=1, s_2=0\right)\\&+P\left(y_1=0 \mid s_1=1, s_2=1\right)P\left(s_1=1, s_2=1\right).\end{aligned} \tag{6.60}$$

Thus, again using (6.56) and (6.57), (6.60) can be written as

$$\begin{aligned}P^{U1}_{e,U2}=&\frac{1}{4}\{P\left(n_1>i'_{th_2}\right)+P\left(2P_2\rho h^1_{eff}+n_1<i'_{th_2}\right)+P\left(2P_1\rho h^1_{eff}+n_1<i'_{th_2}\right)\\&+P\left(2P_1\rho h^1_{eff}+2P_2\rho h^1_{eff}+n_1<i'_{th_2}\right)\},\end{aligned} \tag{6.61}$$

where i'_{th_2} is the threshold for User 2 symbol detection at User 1. Thus, the terms in (6.61) can be solved as:

$$P_{e,U2}^{U1} = \frac{1}{4}\{2Q\left(\beta_2 P_2\right) + Q\left(\beta_2\left(P_2 - 2P_1\right)\right) + Q\left(\beta_2\left(2P_1 + P_2\right)\right)\}, \tag{6.62}$$

where $\beta_2 = {}^{\rho h_1^{eff}}/_{\sigma}$. In order to evaluate $P_{e,U1}$ SIC is implemented after the User 2's signal is decoded first. Following the effective implementation of SIC, the signal at User 1 can be estimated as

$$y'_1 = 2P_1 \rho h_1^{eff} s_1 + n_1. \tag{6.63}$$

The threshold for User 1 signal detection is $i_{th_1} = P_1 \rho h_1^{eff}$. (6.63) can be solved as

$$P'_{e,U1} = Q\left(\beta_2 P_1\right). \tag{6.64}$$

In case of SIC failure, the signal at User 1 can be expressed as

$$y''_1 = 2P_1 \rho h_1^{eff} s_1 + 2P_2 \rho h_1^{eff} s_2 + n_1 - 2P_2 \rho h_1^{eff} \tilde{s}_2, \tag{6.65}$$

where $\tilde{s}_2$ is the incorrectly decoded User 2's signal at User 1. The error probability of User 1 when User 2's signal is incorrectly decoded at User 1 can be given as in (6.66).

$$\begin{aligned} P''_{e,U1} P_{e,U2}^{U1} =& P\left(y''_1 = 1 \mid s_1 = 0, \tilde{s}_2 = 1\right) P\left(\tilde{s}_2 = 1 \mid s_1 = 0, s_2 = 0\right) P\left(s_1 = 0\right) P\left(s_2 = 0\right) \\ &+ P\left(y''_1 = 1 \mid s_1 = 0, \tilde{s}_2 = 0\right) P\left(\tilde{s}_2 = 0 \mid s_1 = 0, s_2 = 1\right) P\left(s_1 = 0\right) P\left(s_2 = 1\right) \\ &+ P\left(y''_1 = 0 \mid s_1 = 1, \tilde{s}_2 = 1\right) P\left(\tilde{s}_2 = 1 \mid s_1 = 1, s_2 = 0\right) P\left(s_1 = 1\right) P\left(s_2 = 0\right) \\ &+ P\left(y''_1 = 0 \mid s_1 = 1, \tilde{s}_2 = 0\right) P\left(\tilde{s}_2 = 0 \mid s_1 = 1, s_2 = 1\right) P\left(s_1 = 1\right) P\left(s_2 = 1\right). \end{aligned} \tag{6.66}$$

$$\begin{aligned}P''_{e,U1}P^{U1}_{e,U2} =&\frac{1}{4}\left\{P\left(n_1 - 2P_2\rho h_1^{eff} > i_{th_1}\right) P\left(n_1 > i'_{th_2}\right)\right.\\&+ P\left(2P_2\rho h_1^{eff} + n_1 < i_{th_1}\right) P\left(2P_2\rho h_1^{eff} + n_1 < i'_{th_2}\right)\\&+ P\left(2P_1\rho h_1^{eff} + n_1 - 2P_2\rho h_1^{eff} < i_{th_1}\right) P\left(2P_1\rho h_1^{eff} + n_1 < i'_{th_2}\right)\\&\left.+P\left(2P_1\rho h_1^{eff} + 2P_2\rho h_1^{eff} + n_1 < i_{th_1}\right) P\left(2P_1\rho h_1^{eff} + 2P_2\rho h_1^{eff} + n_1 < i'_{th_2}\right)\right\}.\end{aligned} \tag{6.67}$$

Using the same approach as in (6.56) and (6.57), Eq. (6.67) can be solved as:

$$\begin{aligned}P''_{e,U1}P^{U1}_{e,U2} =& \frac{1}{4}Q\left(\beta_2\left(P_1 + 2P_2\right)\right)Q\left(\beta_2 P_2\right) + Q\left(\beta_2\left(P_1 - 2P_2\right)\right)Q\left(\beta_2 P_2\right)\\&+ Q\left(\beta_2\left(P_1 - 2P_2\right)\right)Q\left(\beta_2\left(P_2 - 2P_1\right)\right) + Q\left(\beta_2\left(P_1 + 2P_2\right)\right)Q\left(\beta_2\left(2P_1 + P_2\right)\right).\end{aligned} \tag{6.68}$$

Finally, substituting (6.68), (6.62), and (6.64) in (6.59), the error probability of User 1 can be calculated.

6.2 Secrecy sum rate optimization

In this section, we formulate the SSR maximization problem under the constraints on total power transmitted by LED, roll and yaw angles of MA elements of the OSTAR-RIS, refractive index of the LC cell and power allocation factor for NOMA scheme.

Using (6.52), the SSR maximization problem is formulated as

$$\begin{aligned}
&\max_{\{\gamma_{MA},\omega_{MA},\eta_c\}} \hat{R}_{sec},\\
&\text{s.t.} C1: \sum_{j=1}^{K} P_j = P_T,\\
&C2: -\frac{\pi}{2} \leq \omega_{MA} \leq \frac{\pi}{2},\\
&C3: -\frac{\pi}{2} \leq \gamma_{MA} \leq \frac{\pi}{2},\\
&C4: 1.5 \leq \eta_c \leq 1.7,\\
&C5: 0.2 \leq \alpha \leq 0.6. \qquad (6.69)
\end{aligned}$$

In the problem (6.69), $\hat{R}_{sec}$ is SSR to be maximized within the given constraints. For maximizing the SSR the OSTAR-RIS angles γ_{MA} and ω_{MA} can take values within the range $[{}^{-\pi}/_{2}\ {}^{\pi}/_{2}]$. The refractive index of the LC cell can be varied in the limits 1.5 to 1.7, and the power allocation factor (α) for the NOMA scheme can be varied between 0.2 to 0.6.

6.3 PSO-based optimization method

In this section, PSO-based optimizer is proposed to minimize the SSR. PSO is an evolutionary algorithm proposed by Eberhart and Kennedy [73] that starts with a random solution and iteratively improves it to find the optimal solution, similar to the simulated annealing algorithm. It evaluates solutions based on their fitness. PSO follows the best solutions found so far to locate the global optimum. Because of its efficient search capabilities, PSO is effective for solving multi-objective optimization problems. Thus, the PSO-based optimization algorithm can be applied to solve the optimization problem given in (6.69), owing to its simplicity, less complexity and its ability to efficiently explore complex search spaces as compared to an exhaustive search. In PSO each particle symbolizes a possible solution to the optimization problem. The algorithm used is presented in **Algorithm 5**. First, the PSO parameters, such as particle position and velocity, are randomly initialized, and we set the maximum iterations to 120. To determine the fitness value, particles modify their movement based on their own experience and the experience of other

Algorithm 5 PSO-based secrecy rate optimization algorithm.

% ***Initialization:*** Initialize PSO parameters, particle position and velocity. Swarm size ($N_p = 40$), maximum iteration (i_{max}) = 120

% ***Computation:***

for $i = 1; i++$

1. Evaluate R_{sec} for each particle to estimate the local and global best solution.
2. Update the velocity and position of each particle.
3. Check for constraints on γ_{MA}, ω_{MA}, η_c, and α.
4. Go back to (1) and repeat till maximum iterations are reached.

end for

% ***Output:***

Optimum values of γ_{MA}, ω_{MA}, η_c, and α.

particles. The fitness function is the SSR that needs to be maximised under the constraints given in (6.69). The fitness value of all the particles is estimated using the fitness function, and this value is considered the local optimum for that particle. The position corresponding to each particle's local optimum is then initialized accordingly. Considering a D-dimensional search space and a swarm consisting of N_P particles, each particle's position is denoted by a vector X. The particle's velocity, which guides its trajectory through the search space, is represented by a vector V, and is influenced by both its own movement history and that of the other particles. The t_{th} particle in the population is represented by the position and velocity at the i_{th} iteration. In the first iteration, the value of R_{sec} is evaluated for each particle to estimate the local and best solution. Based on the best solution, the velocity and position of each particle are updated. Position vector can be expressed as

$$X_t(i) = [x_t^1(i),\ x_t^2(i), \ldots, x_t^D(i)]^T. \tag{6.70}$$

The velocity vector is as follows:

$$V_t(i) = [v_t^1(i), v_t^2(i), \ldots, v_t^D(i)]^T. \tag{6.71}$$

As of the i_{th} iteration, the best position searched by particle t is calculated as

$$P_t^{best}(i) = [p_t^1(i), p_t^2(i), \ldots, p_t^D(i)]^T. \tag{6.72}$$

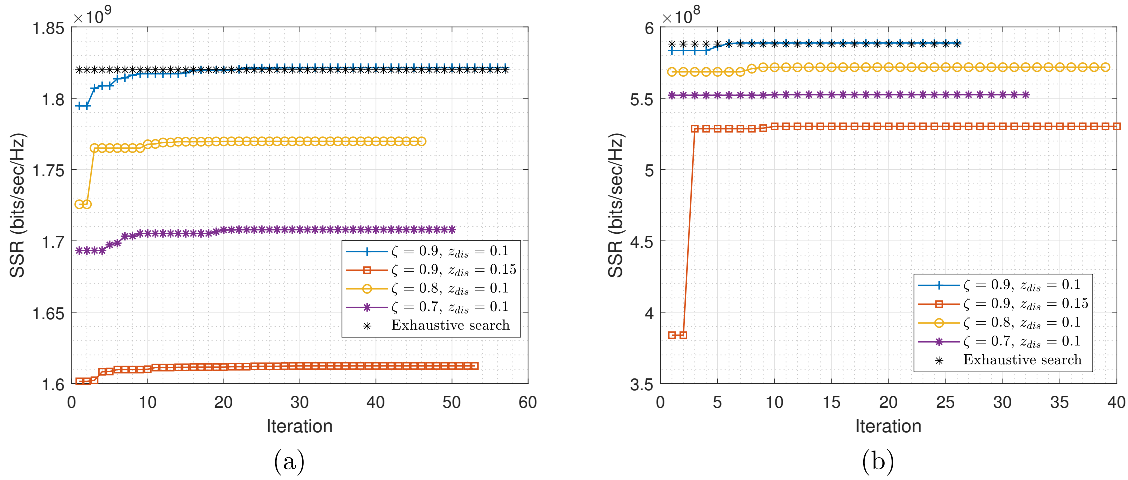

Figure 6.3: Convergence performance of particle swarm optimization algorithm for (a) non orthogonal multiple access and (b) orthogonal multiple access.

$P_t^{best}(i)$ is also called the local history optimal position. After comparing the fitness values of each particle, the maximum fitness value, which represents the population's global ideal value, is determined. The global optimal position experienced by all particles in a particle swarm is denoted as

$$G^{best}(i) = \min\{p_1^{best}(i), p_2^{best}(i), \ldots, p_K^{best}(i)\}. \tag{6.73}$$

For the next iteration, the velocity and the position of each particle can be updated as:

$$v_t^j(i+1) = \omega \cdot v_t^j(i) + c_1 \cdot r \cdot (p_t^{best,j}(i) - x_t^j(i)) + c_2 \cdot r \cdot \left(g^{best,j}(i) - x_t^j(i)\right), \tag{6.74}$$

$$x_t^j(i+1) = x_t^j(i) + v_t^j(i+1), \tag{6.75}$$

where ω represents the inertia weight and plays an important role in balancing the global search and local search, r is a random function within the range [0,1], c_1 adjusts the particle's movement towards its personal best position, and c_2 directs the particle towards the global best position in the swarm. c_1 and c_2 enable the particles to have the ability to learn both socially and individually, making them close to the individual optimal position and global optimal position, respectively. For our application, when using the PSO algorithm, we have considered $c_1 = 2$ and $c_2 = 2$. The PSO algorithm primarily ensures validity of solutions by optimizing

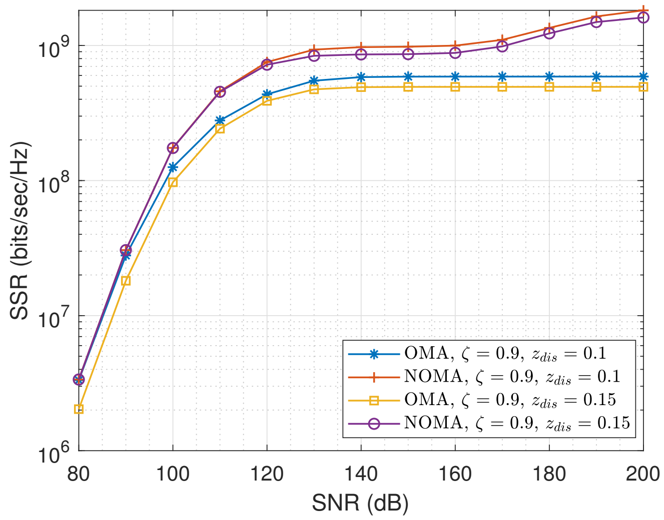

Figure 6.4: Sum rate vs signal-to-noise ratio performance of optical simultaneously transmitting and reflecting-reflecting intelligent surface visible light communication system.

within the feasible solution space when addressing constraint conditions. Before proceeding to the next iteration, the constraints on γ_{MA}, ω_{MA}, η_c, and α are verified as specified by constraints $C1$ to $C5$. This process repeats until the maximum number of iterations (i_{max}) is reached. A comparative analysis with the exhaustive search method is provided to highlight the advantages of the PSO for the proposed model. Once the optimal values for γ_{MA}, ω_{MA}, η_c, and α are obtained, the channel coefficients for both the users and the eavesdropper are calculated based on these values.

6.3.1 Computational Complexity

The PSO method has a close performance compared to the benchmark exhaustive search method with lower complexity. For exhaustive search, the complexity is $\mathcal{O}(N_d^{N_v})$ where N_d is the number of possible values for each decision variable, and N_v is the number of decision variables. The values of parameters γ_{MA} and ω_{MA} are searched in the range $^{-pi}/_2$ to $^{pi}/_2$ with interval size $^{\pi}/_{16}$, α is searched in the range 0.2 to 0.6 with interval size 0.1 and η_c is searched in the range 1.5 to 1.7 with interval size 0.01. Thus, N_d is 94 and N_v is 6. While for PSO, the complexity is $\mathcal{O}(N_p i_{conv})$ where N_p is the swarm size considered as 40 and i_{conv} is the total number of iterations required to reach the optimum solution which is 20.

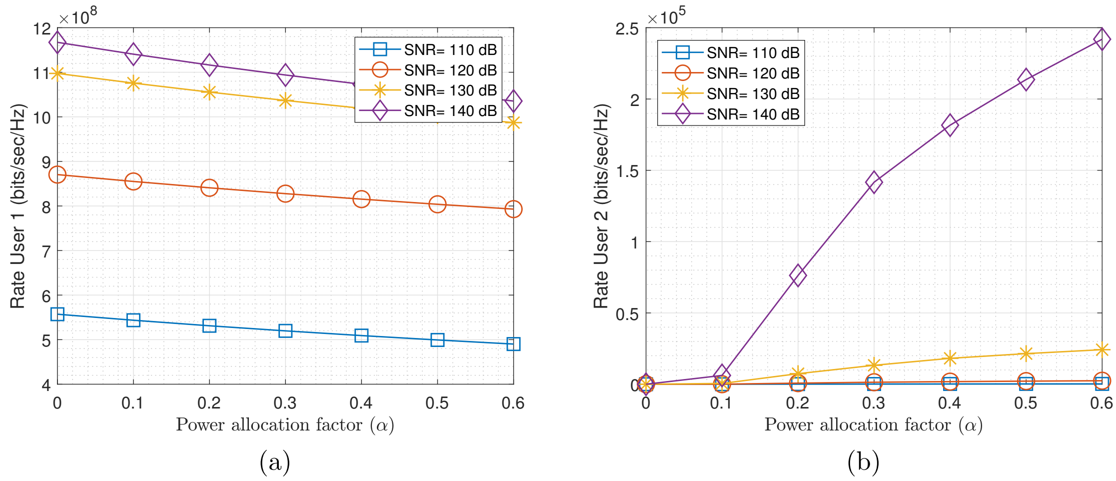

Figure 6.5: Impact of varying power allocation factor on individual rate of both the users.

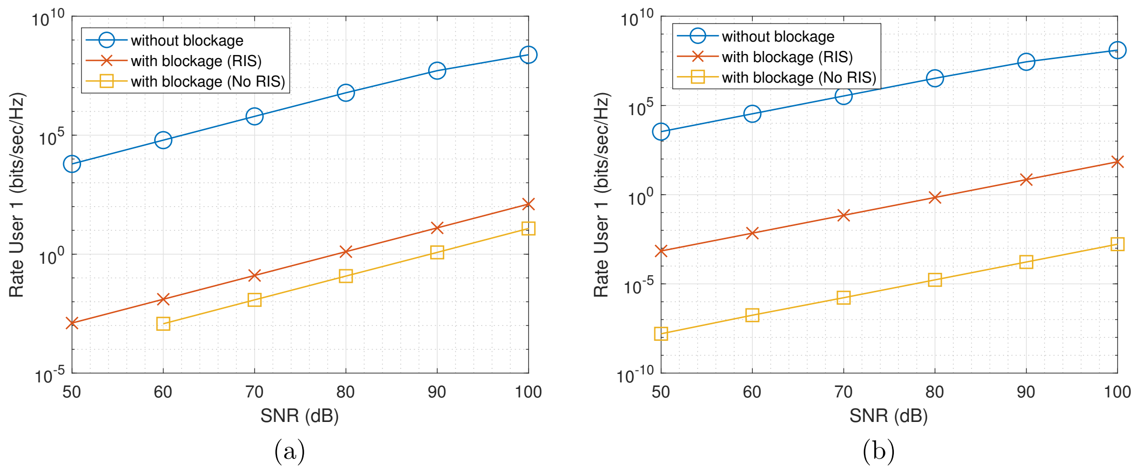

Figure 6.6: Impact of line-of-sight blockage on the secrecy sum rate performance of (a) non orthogonal multiple access and (b) orthogonal multiple access schemes.

Table 6.1: Simulation Parameters for NOMA OSTAR-RIS aided VLC systems.[1]

Parameter	**Symbol**	**Specification**
Photodetector's responsivity	ρ	0.53 A/w
Photodetector's FOV	ξ_{FoV}	85^o
Photodetector's area	A_D	1cm^2
Concentrator refractive index	$\mathrm{r_f}$	1.5
Gain optical filter	$G_o(\xi)$	1.0
Reflection coefficient of mirror array	χ_{RIS}	0.95
Reflection coefficient of wall	χ_{WALL}	0.8
Refractive index of air	η_a	1
Ordinary refractive index of LC cell	η_o	1.5
Extraordinary refractive index of LC cell	η_e	1.7
Depth of LC cell	D	0.75 mm
Optical signal wavelength	λ	510 nm
Electro-optic coefficient	E_o	12pm/V
Critical voltage threshold	V_{th}	1.34 V
Bandwidth	W	200 MHz

6.3.2 Numerical and Simulation Results

In this section, we present simulation results of the proposed optical RIS-aided indoor VLC system. Both rooms are considered to have the same dimensions $5\times5\times3$ m. All the users, eavesdropper and possible blockers are considered to be at a height of 1.65 m, and the receiver is considered to be at a distance of 0.35 m from the body of the user at a height of 0.85 m. The OSTAR-RIS has 8 rows and 8 columns with an equal number of MA and LC elements i.e. 32. The reflection coefficients of the MA OSTAR-RIS element and the wall are 0.95 and 0.8, respectively. The photodetector's responsivity with FoV 85^o is 0.53 A/W. The half-intensity radiation angle of the LED is 70^o. The photodetector's area is 1cm^2. The refractive index of the concentrator is 1.5, and the optical filter gain is 1 [1]. All the simulation parameters are summarised in **Table 6.1**.

Figs. 6.3(a) and 6.3(b) illustrate the convergence performance of the PSO algorithm at SNR of 200 dB employing NOMA and OMA schemes, respectively. To illustrate the effect of LED nonlinearity, different values of ζ and variance of z_{dis} are considered. It can be observed that by decreasing the value of scaling parameter ζ or by increasing the value of z_{dis}, the optimum value of the SSR is reduced owing to the increase in severity of nonlinearity. Considering $\zeta = 0.9$ and $z_{dis} = 0.1$ the SSR for NOMA and OMA schemes converges at 1.82×10^9 and 5.88×10^8. Thus, a gain of approximate 3 times is observed in SSR on employing NOMA as compared to OMA. We can observe that the PSO algorithm converges around 10 iterations for OMA-STAR-RIS VLC system and in around 20 iterations for NOMA-STAR-RIS VLC system.

Figure 6.4 illustrates the SSR performance of the PSO algorithm for OMA and NOMA schemes for different values of SNR at different considered values of ς and variance of z_{dis}. It can be observed that by increasing the value of z_{dis} from 0.1 to 0.15, the optimum value of the SSR for NOMA is reduced from 1.82×10^9 to 1.42×10^9. While for OMA the SSR for NOMA has fallen from 5.88×10^9 to 4.94×10^9. The degradation in the performance on increasing the value of z_{dis} is expected due to the increase in severity of nonlinearity, which is also in line with the results obtained in Figure 6.3. For both the cases with considered nonlinearity, we can observe that the NOMA scheme outperforms the benchmark OMA scheme by providing a gain of around 3 times at SNR 200 dB. This is due to the fact that PD-NOMA accommodates multiple users on the same frequency band through power domain separation while OMA relies on separating users in time which leads to insufficient utilization of resources.

Figs. 6.5(a) and 6.5(b) depict the impact of the power allocation factor of the NOMA scheme on the individual performance of User 1 and User 2, respectively. The simulations are done for different SNR values. For User 1, the sum rate decreases with a decrease in the SNR value, as can be seen in Figure 6.5(a). The same trend is observed in Figure 6.5(b) for User 2, emphasizing the sensitivity of users' rates on the SNR. The rate achieved by User 1 is higher as compared to User 2, due to

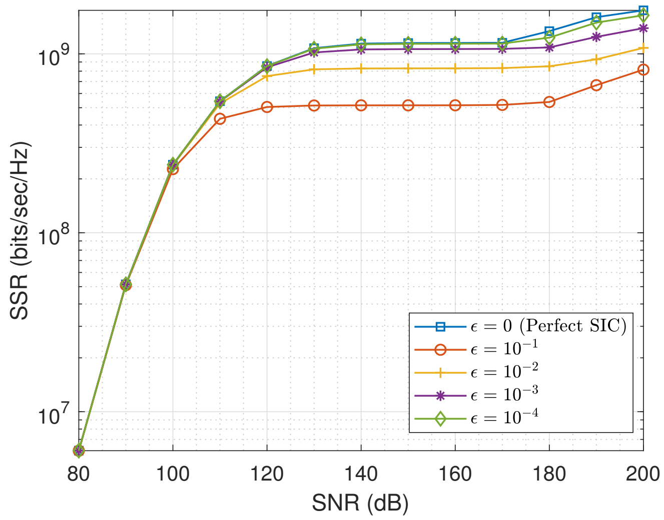

Figure 6.7: Impact of imperfect SIC on the SSR performance.

the presence of the LoS path in Room 1, which carries maximum channel strength. Further, it can be seen that on increasing the power allocation factor the rate of User 2 enhances while the rate of User 1 deteriorates further. As expected, with more power allocated to User 2 on increasing the power allocation factor the rate of User 2 increases.

Figs. 6.6(a) and 6.6(b) depict the impact of the presence of blockage on the rate of User 1 employing both OMA and NOMA schemes. As already stated, the LoS link has the maximum strength and, as a result, has a larger impact on the user rate. For scenario of blockage in Room 1, we have considered $\iota = 0$ in (9), similarly, for blockage free scenario $\iota = 1$. For both NOMA and OMA a loss of around 2.4990×10^6. It can be inferred that the presence of blockage degrades the rate of User 1 as LoS link with maximum channel strength is blocked. This further necessitates the deployment of OSTAR-RIS in VLC system as a promising solution to overcome the drawbacks of LoS blockages.

Figure 6.7 shows the SSR performance of the proposed indoor OSTAR-RIS VLC system in the presence of an eavesdropper while considering imperfect SIC. The perfect SIC is the case where, $\epsilon = 0$. It can be seen that by increasing the SIC error, the SSR of the proposed system degrades. The worst performance is observed when the SIC error is considered to be $\epsilon = 0.1$. Due to imperfect SIC, User 1 can not successfully discard the information of User 2, which leads to inaccurate signal decoding of User 1 and residual interference, ultimately degrading the SSR of the

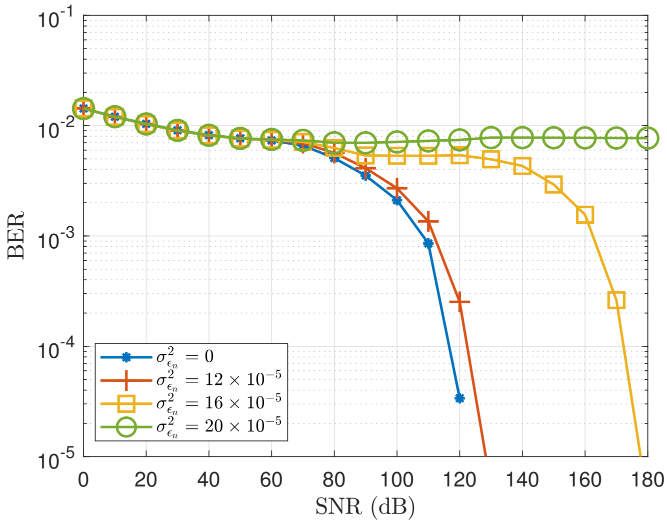

Figure 6.8: BER performance of NOMA considering imperfect CSI.

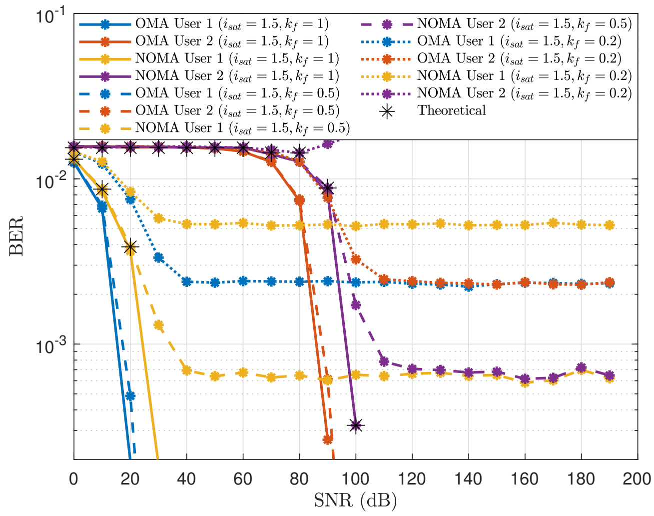

Figure 6.9: BER performance of OMA and NOMA considering perfect SIC and CSI.

NOMA system.

Figure 6.8 shows the BER performance of the proposed indoor NOMA OSTAR-RIS VLC system in the presence of an eavesdropper while considering imperfect CSI and perfect SIC. The perfect CSI is the case with $\sigma^2_{\epsilon_n} = 0$. It can be seen that by increasing the CSI error, the BER of the proposed system degrades. The worst performance is observed when CSI error is considered to be $\sigma^2_{\epsilon_n} = 20 \times 10^{-5}$. The degradation in performance is due to imperfect CSI, which leads to inaccurate power allocation, ineffective SIC, and increased interference in the NOMA system.

Figure 6.9 shows the BER results of both OMA and NOMA schemes by varying the severity of the nonlinearity of LED. Following, three cases of nonlinearity are considered: 1) $i_{sat} = 1.5$, and $k_f = 1$, 2) $i_{sat} = 1.5$, and $k_f = 0.5$, and 3) $i_{sat} = 1.5$, and $k_f = 0.2$, where the nonlinearity severity increases as the value of k_f is decreased. The first case with $I_{sat} = 1.5$, and $k_f = 1$, represents the almost linear case and is compared with our theoretical BER calculated. As expected, the performance of both OMA and NOMA schemes is degraded with the increase in the severity of LED nonlinearity. Although NOMA outperforms OMA in terms of SSR, however as OMA signalling is interference-free, the simulation results show that OMA has the best BER performance for both users. Thus it can be concluded that while NOMA has the advantage of higher spectral efficiency and capacity by serving multiple users simultaneously, the increased complexity of managing interference and ensuring effective SIC often results in worse BER performance compared to OMA. OMA's orthogonal allocation inherently avoids interference, leading to better BER performance.

6.4 Summary

This chapter considered an OSTAR-RIS VLC system model impaired by LED nonlinearity with two indoor users, an eavesdropper and possible blockers. However, the challenges such as LED nonlinearities, limited coverage, signal loss due to blockages, and security vulnerabilities impede its performance. The introduction of an OSTAR-RIS offers a potential solution to enhance coverage and mitigate dead zones. This chapter further explored the integration of NOMA to enhance the SSR of VLC systems. Through the application of PSO, which optimizes the reflector elements of OSTAR-RIS along with the power allocation in NOMA, and the refractive index of the LC cell of the OSTAR-RIS array, significant improvements are achieved. Comparative simulations underscore the effectiveness of the proposed optimization methods, demonstrating their superiority over existing benchmark techniques.

Chapter 7

Conclusions and Future Works

7.1 Conclusions

This thesis presented a comprehensive analysis of various advancements and techniques aimed at enhancing the performance of VLC systems, particularly within the context of future wireless networks integrating RIS, OSTAR-RIS, and advanced modulation techniques. VLC is becoming an increasingly promising alternative to traditional RF communication due to its numerous advantages, such as being environmentally friendly, cost-effective, and secure. These advantages make VLC a highly viable candidate for next-generation wireless communication systems, especially in dense indoor environments where traditional RF-based systems face challenges such as interference, congestion, and security concerns. However, VLC systems also face several challenges that need to be addressed for their successful implementation. These include issues such as LED nonlinearity, which can cause distortions in the transmitted signals, multipath interference, which arises from reflections and scattering of light, ambient noise, which can degrade signal quality, and coverage limitations due to LoS blockages. These include issues such as LED nonlinearity, which can cause distortions in the transmitted signals, multipath interference, which arises from reflections and scattering of light, ambient noise, which can degrade signal quality, and coverage limitations due to LoS blockages. Additionally, user mobility and immobility pose significant challenges, as the changing positions of users can affect the reliability and stability of VLC links, particularly in dynamic environments. While mobile users may experience Doppler shifts and signal fading, immobile users may still face challenges due to fixed obstacles and varying channel conditions. These mobility-related factors further complicate the design and deployment of VLC systems. The proposed RFF-based post-distortion technique for OTFS in nonlinear VLC demonstrated superior BER performance in dynamic VLC environments, showing its robustness and effectiveness in real-world scenarios. In addition, a ZA-LMS sparse channel estimator was proposed for multi-carrier VLC systems, taking advantage of the inherent sparsity in the delay-Doppler domain of the channel. The ZA-LMS algorithm significantly outperformed traditional channel estimation methods, providing more accurate channel estimation, which is crucial for achieving high data rates and reliable communication. Furthermore, the research introduced rate-maximization strategies for RIS-aided indoor VLC systems through Q-Learning, a reinforcement learning technique. Using a function-approximated learning approach, RIS was effectively utilized to enhance the system's data rates, overcome LoS blockages, and adapt to user movement, demonstrating its potential to significantly improve VLC performance in indoor environments. The study also explored the use of CSK modulation along with a DNN-based symbol detector for OSTAR-RIS-aided VLC, which greatly improved the BER and data rates while mitigating interference. This hybrid approach, combining advanced modulation techniques with deep learning, proved to be highly effective in addressing the limitations posed by interference in VLC systems. In addition, the integration of NOMA with OSTAR-RIS was explored to further enhance spectral efficiency and increase the SSR, an important metric for securing communication in multi-user environments. A PSO-based optimization framework was designed for SSR maximization under realistic constraints, demonstrating the potential of NOMA to increase capacity while simultaneously improving security in multi-user VLC environments.

The thesis comprehensively addresses the practical requirements necessary for implementing the advanced VLC techniques and algorithms it proposes. To realize OTFS modulation and its hyperparameter-free RFF-based post-distorter, VLC systems must employ high-speed LEDs with sufficient modulation bandwidth and photodetectors capable of wide dynamic range and fast response. Real-time digital signal processing hardware, such as FPGAs or high-performance DSPs, is essential to handle the computational demands of OTFS transformations, kernel-based post-distortion, and message passing detection. For RIS- and OSTAR-RIS-assisted systems, the deployment of tunable metasurfaces-such as mirror arrays or liquid crystal elements-requires precise mechanical or electronic control to dynamically adjust reflection and refraction angles, along with a controller capable of running reinforcement learning algorithms for optimal configuration in response to user mobility and blockage scenarios. Implementing CSK modulation and DNN-based symbol detection demands multi-channel RGB LED arrays with accurate color calibration, as well as embedded processors or GPUs for training and inference of deep learning models. NOMA and advanced resource allocation schemes necessitate sophisticated driver circuits for power-domain multiplexing and robust software for real-time optimization of power allocation, user scheduling, and successive interference cancellation. Across all these techniques, accurate channel modeling and estimation-often leveraging ray-tracing tools or stochastic models-are vital, as is the integration of robust error correction and security protocols to meet the reliability and privacy requirements of practical deployments. Finally, adherence to industry standards (such as IEEE 802.15.7) and careful system calibration for illumination constraints, safety, and interoperability are crucial for translating these research advances into scalable, real-world VLC solutions.

In conclusion, this thesis provides valuable insights and practical design guidelines for the future development of VLC systems. By leveraging advanced modulation techniques, machine learning, and RIS technologies, it presents innovative solutions to overcome the challenges associated with VLC, including interference, mobility, and coverage limitations. These advancements represent significant steps toward the realization of high-performance VLC networks that are capable of achieving high data rates, reliability, and adaptability, particularly in complex indoor environments. Furthermore, the integration of these technologies positions VLC as a key enabler for the next generation of wireless communication systems, laying the foundation for the development of VLC networks in the realms of 5G, and the emerging 6G technologies. These advancements are pivotal in shaping the future of wireless communication, offering new possibilities for secure, efficient, and sustainable communication systems.

7.2 Future Works

- In this work, MIMO techniques are not explored for dynamic OTFS-aided VLC systems. However, considering the inherent advantages of MIMO in addressing challenges related to capacity, reliability, and coverage, it becomes crucial to analyze and optimize MIMO for such systems. In the literature, MIMO techniques have been widely recognized for their ability to exploit spatial multiplexing and diversity, which significantly improve data rates and robustness in VLC systems. Integrating MIMO with OTFS—a modulation scheme known for its superior performance in multipath and high-mobility scenarios—has the potential to further enhance the efficiency and reliability of VLC systems, particularly in dynamic environments where challenges like signal fading, LED non-linearity, and mobility-induced alignment issues are prevalent.

- Analyzing the performance of movable-ORIS-aided VLC systems for dynamic scenarios is essential for addressing real-world communication challenges. In this work fixed ORIS is considered to be mounted on a wall which does not cater to the need of mobile users. Movable-ORIS introduces a layer of adaptability that can dynamically adjust its orientation or position to maintain optimal link quality, even in environments with mobility or changing obstacles. Dynamic scenarios bring challenges like frequent misalignment, rapid changes in line-of-sight (LoS) conditions, and multipath propagation. By incorporating movable-ORIS, the system can actively reconfigure itself to optimize the channel gain and mitigate impairments like signal blockages or multipath fading.

- In this work, movement of multiple users is not considered which leads to communication conditions which are constantly evolving. ORIS with OTFS-based VLC systems presents a promising research avenue to address challenges such as limited coverage and LoS blockages. In traditional VLC systems, LoS is critical for maintaining high signal quality, but obstacles, mobility, and dynamic environmental changes can lead to significant signal degradation. By combining IRS technology with OTFS modulation, it becomes possible to dynamically manipulate signal propagation and improve system robustness in such scenarios.

These future directions could significantly enhance the performance, robustness, and versatility of VLC systems in practical scenarios.

References

[1] O. Maraqa, S. Aboagye, and T. M. N. Ngatched, "Optical STAR-RIS-Aided VLC Systems: RSMA Versus NOMA," *IEEE Open J. Commun. Soc.*, vol. 5, pp. 430–441, 2024.

[2] T. Komine and M. Nakagawa, "Performance evaluation of visible-light wireless communication system using white LED lightings," in *Proceedings. ISCC 2004. Ninth International Symposium on Computers And Communications (IEEE Cat. No. 04TH8769)*, vol. 1. IEEE, 2004, pp. 258–263.

[3] K. Lee, H. Park, and J. R. Barry, "Indoor channel characteristics for visible light communications," *IEEE Commun. Lett.*, vol. 15, no. 2, pp. 217–219, 2011.

[4] D. C. O'Brien, L. Zeng, H. Le-Minh, G. Faulkner, J. W. Walewski, and S. Randel, "Visible light communications: Challenges and possibilities," in *IEEE 19th International Symposium on Personal, Indoor and Mobile Radio Communications*, Sep. 2008, pp. 1–5.

[5] J. Barry, J. Kahn, W. Krause, E. Lee, and D. Messerschmitt, "Simulation of multipath impulse response for indoor wireless optical channels," *IEEE J. Sel. Areas Commun.*, vol. 11, no. 3, pp. 367–379, 1993.

[6] S. Long, M.-A. Khalighi, M. Wolf, S. Bourennane, and Z. Ghassemlooy, "Channel characterization for indoor visible light communications," in *2014 3rd International Workshop in Optical Wireless Communications (IWOW)*. IEEE, 2014, pp. 75–79.

[7] F. Miramirkhani and M. Uysal, "Channel Modeling and Characterization for Visible Light Communications," *IEEE Photonics J.*, vol. 7, no. 6, pp. 1–16, 2015.

[8] L. Yin, W. O. Popoola, X. Wu, and H. Haas, "Performance Evaluation of Non-Orthogonal Multiple Access in Visible Light Communication," *IEEE Trans. Commun.*, vol. 64, no. 12, pp. 5162–5175, 2016.

[9] A. Gupta and P. Garg, "Statistics of SNR for an Indoor VLC System and Its Applications in System Performance," *IEEE Commun. Lett.*, vol. 22, no. 9, pp. 1898–1901, 2018.

[10] M. A. Arfaoui, M. D. Soltani, I. Tavakkolnia, A. Ghrayeb, C. Assi, H. Haas, and M. Safari, "SNR Statistics of Indoor Mobile VLC Users with Random Device Orientation," in *Proc. IEEE Int. Conf. Commun. (ICC)*, 2019, pp. 1–6.

[11] A. M. Abdelhady *et al.*, "Visible Light Communications via Intelligent Reflecting Surfaces: Metasurfaces vs Mirror Arrays," *IEEE Open J. Commun. Soc.*, vol. 2, pp. 1–20, Dec. 2021.

[12] H. Haas, "LiFi: Conceptions, misconceptions and opportunities," in *Proc. IEEE Photon. Conf.*, Oct 2016, pp. 680–681.

[13] R. Mitra and V. Bhatia, "Chebyshev Polynomial-Based Adaptive Predistorter for Nonlinear LED Compensation in VLC," *IEEE Photon. Technol. Lett.*, vol. 28, no. 10, pp. 1053–1056, May 2016.

[14] K. Reddy Sekhar, F. Miramirkhani, R. Mitra, and A. C. Turlapaty, "Generic BER Analysis of VLC Channels Impaired by 3D User-Mobility and Imperfect CSI," *IEEE Commun. Lett.*, pp. 1–1, 2021.

[15] J. Armstrong, "OFDM for Optical Communications," *J. Light. Technol.*, vol. 27, no. 3, pp. 189–204, Feb 2009.

[16] R. Mitra, S. Jain, and V. Bhatia, "Least Minimum Symbol Error Rate Based Post-Distortion for VLC Using Random Fourier Features," *IEEE Commun. Lett.*, vol. 24, no. 4, pp. 830–834, 2020.

[17] R. Hadani, S. Rakib, M. Tsatsanis, A. Monk, A. J. Goldsmith, A. F. Molisch, and R. Calderbank, "Orthogonal Time Frequency Space Modulation," in *Proc. IEEE Wireless Commun. Netw. Conf. (WCNC)*, March 2017, pp. 1–6.

[18] G. Stepniak, J. Siuzdak and P. Zwierko, “Compensation of a VLC Phosphorescent White LED Nonlinearity by Means of Volterra DFE,” *IEEE Photon. Technol. Lett.*, vol. 25, no. 16, pp. 1597–1600, 2013.

[19] H. Qian, S. J. Yao, S. Z. Cai and T. Zhou, “Adaptive Postdistortion for Nonlinear LEDs in Visible Light Communications,” *IEEE Photonics J.*, vol. 6, no. 4, pp. 1–8, 2014.

[20] Y. Wang, L. Tao, X. Huang, J. Shi and N. Chi, “Enhanced Performance of a High-Speed WDM CAP 64 VLC System Employing Volterra Series-Based Nonlinear Equalizer,” *IEEE Photonics J.*, vol. 7, no. 3, pp. 1–7, 2015.

[21] D. Zheng, H. Zhang, and J. Song, “DCO-OTFS-based full-duplex relay-assisted visible light communications,” *Opt. Express*, vol. 29, no. 25, pp. 41 323–41 332, Dec 2021.

[22] G. D. Surabhi, R. M. Augustine, and A. Chockalingam, “On the Diversity of Uncoded OTFS Modulation in Doubly-Dispersive Channels,” *IEEE Trans. Wireless Commun.*, vol. 18, no. 6, pp. 3049–3063, June 2019.

[23] P. Raviteja, K. T. Phan, Y. Hong, and E. Viterbo, “Interference Cancellation and Iterative Detection for Orthogonal Time Frequency Space Modulation,” *IEEE Trans. Wireless Commun.*, vol. 17, no. 10, pp. 6501–6515, Oct 2018.

[24] P. Raviteja, E. Viterbo, and Y. Hong, “OTFS Performance on Static Multipath Channels,” *IEEE Wireless Commun. Lett.*, vol. 8, no. 3, pp. 745–748, June 2019.

[25] A. Sharma, S. Jain, R. Mitra and V. Bhatia, “Performance Analysis of OTFS Over Multipath Channels for Visible Light Communication,” in *Proc. Int. Conf. Commun., Signal Process., their Appl. (ICCSPA)*, 2021, pp. 1–6.

[26] H. Elgala, R. Mesleh, and H. Haas, “An LED Model for Intensity-Modulated Optical Communication Systems,” *IEEE Photon. Technol. Lett.*, vol. 22, no. 11, pp. 835–837, 2010.

[27] D. Suvra Sekhar, R. Vivek, T. Shashank, M. Subhas Chandra, “Time Domain Channel Estimation and Equalization of CP-OTFS Under Multiple Frac-

tional Dopplers and Residual Synchronization Errors," *IEEE Access*, vol. 9, pp. 10 561–10 576, 2021.

[28] A. Thomas, K. Deka, P. Raviteja, and S. Sharma, "Convolutional Sparse Coding based Channel Estimation for OTFS-SCMA in Uplink," *IEEE Transactions on Communications*, pp. 1–1, 2022.

[29] O K. Rasheed, G. D. Surabhi and A. Chockalingam, "Sparse Delay-Doppler Channel Estimation in Rapidly Time-Varying Channels for Multiuser OTFS on the Uplink," in *Proc. IEEE Veh. Technol. Conf. (VTC-Spring)*, 2020, pp. 1–5.

[30] H. S. C. L. I. S. Wenqian, D. Linglong and R. W. Heath, "Channel estimation for orthogonal time frequency space (otfs) massive mimo," in *IEEE International Conference on Communications (ICC)*, 2019, pp. 1–6.

[31] S. Srivastava, P. Sharma, S. Dwivedi, A. K. Jagannatham, and L. Hanzo, "Fast Block LMS Based Estimation of Angularly Sparse Channels for Single-Carrier Wideband Millimeter Wave Hybrid MIMO Systems," *IEEE Transactions on Vehicular Technology*, vol. 70, no. 1, pp. 666–681, 2021.

[32] A. Sharma, V. Shukla, Bhaskar, and V. Bhatia, "ZA-LMS based Sparse Channel Estimator for VLC-OTFS," in *2021 ANTS*, 2022.

[33] D. Middleton and R. Esposito, "Simultaneous optimum detection and estimation of signals in noise," *IEEE Transactions on Information Theory*, vol. 14, no. 3, pp. 434–444, 1968.

[34] J. Lee, G.-T. Gil, and Y. H. Lee, "Channel estimation via orthogonal matching pursuit for hybrid MIMO systems in millimeter wave communications," *IEEE Trans. Commun.*, vol. 64, no. 6, pp. 2370–2386, Jun. 2016.

[35] S. Srivastava, A. Mishra, A. K. Jagannatham, and G. Ascheid, "SBL-based hybrid precoder/combiner design for power and spectrally efficient millimeter wave MIMO systems," in *2020 Int. Conf. Signal Process. Commun. (SPCOM)*. IEEE, Jul. 2020, pp. 1–5.

[36] J. Jin, Y. Gu, and S. Mei, "A stochastic gradient approach on compressive sensing signal reconstruction based on adaptive filtering framework," *IEEE J. Sel. Topics Signal Process.*, vol. 4, no. 2, pp. 409–420, Apr. 2010.

[37] H. Sayed, Ali, *Fundamentals of Adaptive Filtering.* John Wiley & Sons, 2003.

[38] D. Sabui, S. Chatterjee, and G. S. Khan, "Impact of different receiver geometries on a reconfigurable intelligent surface assisted multi-cell VLC system in the presence of light path blockage," *Appl. Opt.*, vol. 63, no. 10, pp. 2404–2414, Apr 2024. [Online]. Available: https://opg.optica.org/ao/abstract.cfm?URI=ao-63-10-2404

[39] C. Liu, J. Wang, L. Feng, H. Chen, and Z. Xue, "Robust layout optimization for intelligent reflecting surfaces-based visible light communication systems," *Appl. Opt.*, vol. 63, no. 8, pp. 2020–2029, Mar 2024. [Online]. Available: https://opg.optica.org/ao/abstract.cfm?URI=ao-63-8-2020

[40] R. C. Kizilirmak, O. Narmanlioglu, and M. Uysal, "Relay-Assisted OFDM-Based Visible Light Communications," *IEEE Transactions on Communications*, vol. 63, no. 10, pp. 3765–3778, 2015.

[41] D. Kumar, P. K. Singya, O. Krejcar, K. Choi, and V. Bhatia, "Performance of IRS-Aided FD Two-Way Communication Network With Imperfect SIC," *IEEE Trans. Veh. Technol.*, vol. 72, no. 4, pp. 5491–5496, 2023.

[42] G. Singh, A. Srivastava, and V. A. Bohara, "Visible Light and Reconfigurable Intelligent Surfaces for Beyond 5G V2X Communication Networks at Road Intersections," *IEEE Trans. Veh. Tech.*, vol. 71, no. 8, pp. 8137–8151, 2022.

[43] S. Aboagye *et al.*, "Intelligent Reflecting Surface-Aided Indoor Visible Light Communication Systems," *IEEE Commun. Lett.*, vol. 25, no. 12, pp. 3913–3917, Dec. 2021.

[44] S. Sun, F. Yang, and J. Song, "Sum Rate Maximization for Intelligent Reflecting Surface-Aided Visible Light Communications," *IEEE Commun. Lett.*, vol. 25, no. 11, pp. 3619–3623, Nov. 2021.

[45] T. Yang, P. Wang, G. Li, H. Wang, S. Li, H. Shi, H. He, F. Shi, and S. Chi, "Average signal-to-noise ratio maximization for an intelligent reflecting surface and angle diversity receiver jointly assisted indoor visible light communication system," *Appl. Opt.*, vol. 61, no. 35, pp. 10 390–10 399, Dec 2022. [Online]. Available: https://opg.optica.org/ao/abstract.cfm?URI=ao-61-35-10390

[46] N. C. Luong *et al.*, "Applications of Deep Reinforcement Learning in Communications and Networking: A Survey," *IEEE Commun. Surv. Tutor.*, vol. 21, no. 4, pp. 3133–3174, 2019.

[47] X. Kong, G. Duan, M. Hou, G. Shen, H. Wang, X. Yan, and M. Collotta, "Deep Reinforcement Learning-Based Energy-Efficient Edge Computing for Internet of Vehicles," *IEEE Trans. Industr. Inform.*, vol. 18, no. 9, pp. 6308–6316, 2022.

[48] H. Henniger and O. Wilfert, "An Introduction to Free-space Optical Communications," *Radioengineering journal*, vol. 19, pp. 203–212, 06 2010.

[49] G. Tesauro, "Temporal Difference Learning and TD-Gammon," *Commun. ACM*, vol. 38, no. 3, p. 58–68, mar 1995.

[50] R. Sutton and A. Barto, *Reinforcement Learning, second edition: An Introduction*, ser. Adaptive Computation and Machine Learning series. MIT Press, 2018.

[51] L. P. Devroye, "On the Convergence of Statistical Search," *IEEE Transactions on Systems, Man, and Cybernetics*, vol. SMC-6, no. 1, pp. 46–56, 1976.

[52] R. Sutton, A. Barto, and R. Williams, "Reinforcement learning is direct adaptive optimal control," *IEEE Control Systems Magazine*, vol. 12, no. 2, pp. 19–22, 1992.

[53] R. Mitra and V. Bhatia, "Precoded Chebyshev-NLMS-Based Pre-Distorter for Nonlinear LED Compensation in NOMA-VLC," *IEEE Trans. Commun.*, vol. 65, no. 11, pp. 4845–4856, 2017.

[54] J. Tsitsiklis and B. Van Roy, "An analysis of temporal-difference learning with function approximation," *IEEE Trans. Autom. Control*, vol. 42, no. 5, pp. 674–690, 1997.

[55] N. Garg, M. Sellathurai, V. Bhatia, and T. Ratnarajah, "Function approximation based reinforcement learning for edge caching in massive mimo networks," *IEEE Trans. Commun.*, vol. 69, no. 4, pp. 2304–2316, 2021.

[56] N. Garg, M. Sellathurai, and T. Ratnarajah, "Linear approximation based q-learning for edge caching in massive mimo networks," in *53rd Asilomar Conference on Signals, Systems, and Computers*, 2019, pp. 1769–1773.

[57] E. Monteiro and S. Hranilovic, "Constellation design for color-shift keying using interior point methods," in *Proc. IEEE Global Commun. Wrkshps. (GLOBECOM)*, 2012, pp. 1224–1228.

[58] J. Tang, L. Zhang, and Z. Wu, "Exact Bit Error Rate Analysis for Color Shift Keying Modulation," *IEEE Commun. Lett.*, vol. 22, no. 2, pp. 284–287, 2018.

[59] R. Singh, T. O'Farrell, and J. David, "An Enhanced Color Shift Keying Modulation Scheme for High-Speed Wireless Visible Light Communications," *J. Light. Technol.*, vol. 32, pp. 2582–2592, 07 2014.

[60] H. Ye, G. Y. Li, and B.-H. Juang, "Power of Deep Learning for Channel Estimation and Signal Detection in OFDM Systems," *IEEE Wireless Commun. Lett.*, vol. 7, no. 1, pp. 114–117, Feb. 2018.

[61] Y. Saito, Y. Kishiyama, A. Benjebbour, T. Nakamura, A. Li, and K. Higuchi, "Non-Orthogonal Multiple Access (NOMA) for Cellular Future Radio Access," in *Proc. IEEE Veh. Technol. Conf. (VTC-Spring)*, 2013, pp. 1–5.

[62] L. Dai, B. Wang, Y. Yuan, S. Han, I. Chih-lin, and Z. Wang, "Non-orthogonal multiple access for 5G: solutions, challenges, opportunities, and future research trends," *IEEE Commun. Mag.*, vol. 53, no. 9, pp. 74–81, 2015.

[63] C. Liu, L. Yu, X. Yu, J. Qian, Y. Wang, and Z. Wang, "Capacity Analysis of RIS-assisted Visible Light Communication Systems with Hybrid NOMA," in *IEEE Globecom Workshops (GC Wkshps)*, 2022, pp. 118–123.

[64] H. Marshoud, V. M. Kapinas, G. K. Karagiannidis, and S. Muhaidat, "Non-Orthogonal Multiple Access for Visible Light Communications," *IEEE Photon. Technol. Lett.*, vol. 28, no. 1, pp. 51–54, 2016.

[65] T. Le Anh and I. P. Hong, "Secrecy Performance of a Multi-NOMA-MIMO System in the UEH Relaying Network Using the PSO Algorithm," *IEEE Access*, vol. 9, pp. 2317–2331, 2021.

[66] L. Lei, D. Yuan, C. K. Ho, and S. Sun, "Power and Channel Allocation for Non-Orthogonal Multiple Access in 5G Systems: Tractability and Computation," *IEEE Trans. Wireless Commun.*, vol. 15, no. 12, pp. 8580–8594, 2016.

[67] Z. Xiao, L. Zhu, J. Choi, P. Xia, and X.-G. Xia, "Joint Power Allocation and Beamforming for Non-Orthogonal Multiple Access (NOMA) in 5G Millimeter Wave Communications," *IEEE Trans. Wireless Commun.*, vol. 17, no. 5, pp. 2961–2974, 2018.

[68] F. Fang, J. Cheng, and Z. Ding, "Joint Energy Efficient Subchannel and Power Optimization for a Downlink NOMA Heterogeneous Network," *IEEE Trans. Veh. Technol.*, vol. 68, no. 2, pp. 1351–1364, 2019.

[69] Y. Saito, A. Benjebbour, Y. Kishiyama, and T. Nakamura, "System-level performance evaluation of downlink non-orthogonal multiple access (NOMA)," in *Proc. IEEE 24th Annu. Int. Symp. Pers. Indoor Mobile Radio Commun. (PIMRC)*, 2013, pp. 611–615.

[70] C. C. Trinca, J.-C. Belfiore, E. D. de Carvalho, and J. Vieira Filho, "Estimation with mean square error for real-valued channel quantization," in *2014 IEEE Globecom Workshops (GC Wkshps)*, 2014, pp. 275–280.

[71] K. Ying, H. Qian, R. J. Baxley, and S. Yao, "Joint Optimization of Precoder and Equalizer in MIMO VLC Systems," *IEEE J. Sel. Areas Commun.*, vol. 33, no. 9, pp. 1949–1958, 2015.

[72] H. Ma, L. Lampe, and S. Hranilovic, "Coordinated Broadcasting for Multiuser Indoor Visible Light Communication Systems," *IEEE Trans. Commun.*, vol. 63, no. 9, pp. 3313–3324, 2015.

[73] R. Eberhart and J. Kennedy, "A new optimizer using particle swarm theory," in *MHS'95. Proceedings of the Sixth International Symposium on Micro Machine and Human Science*, 1995, pp. 39–43.

List of Publications

Journal Papers:

1. **A. Sharma**, V.B. Shukla, V. Bhatia et al., “ZA-LMS-based sparse channel estimator in multi-carrier VLC system,” ***Photon Netw Commun.***, 47, pp. 30–38, 2024.

2. **A. Sharma**, R. Mitra, O. Krejcar, K. Choi, M. Dobrovolny, and V. Bhatia, “Hyperparameter-Free RFF Based Post-Distorter for OTFS VLC System,” ***IEEE Photonics Journal***, vol. 15, no. 2, April 2023.

3. **A. Sharma**, K. Singh, V. Bhatia, C. P. Li, and Z. Ding, “CSK Modulation Scheme and DNN-Based Symbol Detection in OSTAR-RIS-aided VLC Systems,” ***IEEE Wireless Communication Letters***, vol. 14, no. 4, pp. 1094-1098, April 2025.

Conference Papers:

1. **A. Sharma** and S. Sengar, "Performance Analysis of Indoor VLC System under Different System Configuration," in ***Proc. 3rd International Conference on Electronics, Communication and Aerospace Technology (ICECA)***, Coimbatore, India, 2019, pp. 768-773.

2. **A. Sharma**, S. Jain, R. Mitra, and V. Bhatia, "Performance Analysis of OTFS Over Multipath Channels for Visible Light Communication," in ***Proc. International Conference on Communications, Signal Processing, and their Applications (ICCSPA)***, 2021, pp. 1-6.

3. **A. Sharma**, S. Jain, R. Mitra, and V. Bhatia, "Performance Analysis of OTFS Over Mobile Multipath Channels for Visible Light Communication," in ***IEEE REGION 10 CONFERENCE (TENCON)***, 2020, pp. 490-495.

4. T. Sivalingam, **A. Sharma**, V. Bhatia, N. Rajatheva, S. Sharma, and K. Deka, "Federated Learning-based Base Station Selection on 3D LiDAR Data for Beyond 5G Communications," in ***Proc. IEEE International Conference on Advanced Networks and Telecommunications Systems (ANTS)***, Jaipur, India, 2023, pp. 1-6.

5. **A. Sharma** and V. Bhatia, "VLMS based Channel Estimator for OTFS VLC System," in ***Proc. IEEE International Conference on Advanced Networks and Telecommunications Systems (ANTS)***, Gandhinagar, Gujarat, India, 2022, pp. 249-254.

6. **A. Sharma**, V. B. Shukla, and V. Bhatia, "ZA-LMS based Sparse Channel Estimator for VLC-OTFS," in ***Proc. IEEE International Conference on Advanced Networks and Telecommunications Systems (ANTS)***, Gandhinagar, Gujarat, India, 2022, pp. 1-6.

7. **A. Sharma**, P. Keshari, and V. Bhatia, "LSTM-based Channel Estimator for Optical IRS-Assisted non-Linear VLC Systems," in ***Proc. IEEE International Conference on Advanced Networks and Telecommunications Systems (ANTS)***, Jaipur, India, 2023, pp. 114-119.